Estimations of mechanical properties of intact and damaged bone from high resolution CT-images

Citation for published version (APA):
Arias Moreno, A. J. (2019). *Estimations of mechanical properties of intact and damaged bone from high resolution CT-images.* [Phd Thesis 1 (Research TU/e / Graduation TU/e), Biomedical Engineering]. Technische Universiteit Eindhoven.

Document status and date:
Published: 27/06/2019

Document Version:
Publisher's PDF, also known as Version of Record (includes final page, issue and volume numbers)

Please check the document version of this publication:

• A submitted manuscript is the version of the article upon submission and before peer-review. There can be important differences between the submitted version and the official published version of record. People interested in the research are advised to contact the author for the final version of the publication, or visit the DOI to the publisher's website.
• The final author version and the galley proof are versions of the publication after peer review.
• The final published version features the final layout of the paper including the volume, issue and page numbers.

Link to publication

General rights
Copyright and moral rights for the publications made accessible in the public portal are retained by the authors and/or other copyright owners and it is a condition of accessing publications that users recognise and abide by the legal requirements associated with these rights.

- Users may download and print one copy of any publication from the public portal for the purpose of private study or research.
- You may not further distribute the material or use it for any profit-making activity or commercial gain
- You may freely distribute the URL identifying the publication in the public portal.

If the publication is distributed under the terms of Article 25fa of the Dutch Copyright Act, indicated by the "Taverne" license above, please follow below link for the End User Agreement:

www.tue.nl/taverne

Take down policy
If you believe that this document breaches copyright please contact us at:

openaccess@tue.nl

providing details and we will investigate your claim.

Download date: 13. abr.. 2023

ESTIMATIONS OF MECHANICAL PROPERTIES OF INTACT AND DAMAGED BONE FROM HIGH RESOLUTION CT-IMAGES

Andrés Julián Arias-Moreno

Estimations of Mechanical Properties of Intact and Damaged Bone from High Resolution CT-images

Andrés Julián Arias-Moreno

Cover designed by J.R. Arias-Moreno, Graphic Designer (julian.arias.moreno@gmail.com).
Printed by ProefschriftMaken (www.Proefschriftmaken.nl)

A catalogue record is available from the Eindhoven University of Technology Library
ISBN: 978-90-386-4804-0.

This work was supported by the grants program "Programa de Formación Doctoral Francisco José de Caldas Generación del Bicentenario" awarded by the Francisco José de Caldas Institute for the Development of Science and Technology (COLCIENCIAS, Colombia) and sponsored by the Autonomous University of Manizales. LASPAU ID 20110290.

REPÚBLICA DE COLOMBIA
COLCIENCIAS

UAM
UNIVERSIDAD
AUTÓNOMA DE MANIZALES

Estimations of Mechanical Properties of Intact and Damaged Bone from High Resolution CT-images

PROEFSCHRIFT

ter verkrijging van de graad van doctor aan de Technische Universiteit Eindhoven,
op gezag van de rector magnificus prof.dr.ir. F.P.T. Baaijens, voor een commissie
aangewezen door het College voor Promoties, in het openbaar te verdedigen op
donderdag 27 juni 2019 om 16:00 uur

door

Andrés Julián Arias-Moreno

geboren te Bogotá, Colombia

Dit proefschrift is goedgekeurd door de promotoren en de samenstelling van de promotiecommissie is als volgt:

voorzitter:	Prof. Dr. P.A.J. Hilbers
1e promotor:	Prof. Dr. K. Ito
Copromotor:	Dr. Ir. B. van Rietbergen
leden:	Prof. Dr. G.H. van Lenthe (KU Leuven)
	Prof. Dr. D. A. Garzón-Alvarado (National University of Colombia)
	Prof. Dr. Ir. N.J.J. Verdonschot (Radboud Universiteit UMC)
	Prof. Dr. Ir. R.H.J. Peerlings

Het onderzoek of ontwerp dat in dit proefschrift wordt beschreven is uitgevoerd in overeenstemming met de TU/e Gedragscode Wetenschapsbeoefening.

Dedicated to don Leo,

who always liked good music; especially this one:

En la vereda Velandia del municipio de Saboyá,
Una cucharita e'hueso me regalaron por amistá.

(In the village of Velandia in the municipality of Saboyá,
A teaspoon of bone was given to me for friendship.)

La Cucharita (the Teaspoon), Jorge Velosa

Traditional Colombian music

Table of Content

Chapter 1

General Introduction

Bone

Structure and function

Bone tissue is a connective tissue composed of two phases: a mineral phase and an organic phase (Piekarski, 1973). The characteristic of having two phases makes bone acquire exceptional mechanical properties, as the inorganic phase provides stiffness and strength, while the organic component provides toughness. Bone also is a highly dynamic living tissue with a unique capability of remodeling and of self-repair (Nordin *et al.*, 2012). Its main functions are to serve as the body framework, to protect essential organs, and to distribute and transmit mechanical loads that occur due to physical activity. Bone also has a function as a reservoir for calcium, blood cells and fat.

At the organ level (> 5 mm), bone tissue is characterized by its porosity into two types of tissues: cortical bone (also named dense or compact bone) and trabecular bone (also called cancellous or porous bone). Cortical bone tissue has a porosity ranging between 5% and 10%, and a density of approximately 1.85 g/cm^3. Trabecular bone has a porosity ranging from 50% to 90%, and a density in the range of 0.9 – 0.2 g/cm^3 (Lieberman *et al.*, 2005). Within the pores of trabecular bone fat and marrow is located. Cortical bone typically forms the outer shell of long bones while cancellous bone is located near the joints in long bones, and at the center of most other bones. The delineation between the cancellous and cortical region is the endosteal boundary. In contrast to the periosteal boundary, which identifies the outer surface of the bone, the endosteal boundary is not always clearly identifiable as the transition can be smooth with dense cortical bone gradually transforming to porous cancellous bone (Piekarski, 1973; Vaz *et al.*, 2011, Burr, 2019).

At the tissue level (100 – 1000 µm), cortical bone is made up of osteons (also named haversian systems): concentric lamellar bone layers that surround a central channel where blood vessels and nerves are located. Osteons are around 250 microns in diameter and located in the thicker cortical region such as the diaphysis of long bones, but typically are absent in thin cortical layers such as in small animals. Trabecular bone at this level is forming a highly connected network consisting of plates and rods with a thickness in the range of 200 µm. The plates and rods typically have a preferred orientation that aligns with the loading directions (Meyer *et al.*, 2006; Burr, 2019).

Microscopically (5 – 50 µm), bone has two forms: woven and lamellar. Woven bone is considered immature and is normally found only in the growing bone and in the post-fracture callus. This primary bone has the appearance of a disorganized tissue. It has more cells per unit volume that the lamellar bone and can form quickly. Lamellar bone is the normal type of bone tissue that results as a product of a bone remodeling process. It forms the osteon and is also found as packets in trabecular bone tissue (Piekarski, 1973; Vaz *et al.*, 2011, Burr, 2019).

At the nano level (<100 nm), the mineral phase of bone is composed of hydroxyapatite crystals and the organic phase of type I collagen (Rho *et al.*, 1998; Burr, 2019). At this level, the composition of cortical and trabecular bone tissue is the same.

Bone Cells and Bone Remodeling

Bone is formed and remodeled by bone cells (Majeska, 2001; Burr, 2019). Three types of cells are present in bone tissue: osteoblasts, osteoclast and osteocyte cells. Osteoblast cells form the bone tissue. They are mononuclear cells that derive from pre-cursor cells and are located at the surface of the bone. Osteoclast cells are bone resorbing cells. They are multinucleated cells characterized by their large size (20 to 100 µm in diameter) that also reside at the bone surface. Osteocyte cells, finally, are cells located within the bone matrix. They derive from osteoblast cells that are embedded in the matrix they form. The osteocytes reside in lacunae within the matrix and form a highly connected network as they have many processes that connect to other osteocytes via canaliculi in the matrix. Osteocytes also cover the bone surfaces where they are typically referred to as bone lining cells.

Throughout its lifetime, old bone tissue is constantly removed by osteoclast cells (resorption) and newly formed by osteoblasts (formation) (Geddes, 1996; Rosen, 2003). Every year about 25% of trabecular bone and 3% of cortical bone is replaced (Parfitt, 1994). This process is called bone remodeling, and enables bone to repair microcracks and to change its mass and structure. During bone remodeling, osteoblasts and osteoclasts work together, in what is called a Basic Multicellular Unit (BMU) (Parfitt, 1983; Rosen, 2003; Hollinger, 2005; Crockett *et al.*, 2011). BMU remodeling follows a well-defined sequence of phases that always begins with activation, followed by resorption, lastly followed by formation (Recker, 1983; Kular *et al.*, 2012). It is generally assumed nowadays that osteocyte cells initiate and regulate this process, and that one of the main triggers for this is the mechanical loading (Aarden *et al.*, 1994; Manolagas S.C., 2000; Matsuo *et al.*, 2008; Crockett *et al.*, 2011). Osteocytes can recruit osteoclast to remove bone at locations of microcracks and can stimulate osteoblast to add new bone during the last phase of BMU remodeling (Rosen, 2003). By adding more bone than was removed first, highly loaded structures can be thickened while by adding less bone than originally removed low loaded structures can be thinned (Frost, 1986; Goodship *et al.*, 2001; Hollinger, 2005). In this way bone can form strong though lightweight structures that are adapted to mechanical loading (Buckwalter *et al.*, 1995; Goodship *et al.*, 2001; Kotiya *et al.*, 2013; Kohrt *et al.*, 2013; Silva, 2013).

Bone tissue mechanical properties

As mentioned before, one of the main functions of bone is a mechanical one. Bone fractures can be catastrophic events, and as such bone strength is an important characteristic. Bone tissue strength is highly dependent on the porosity of the bone and the microstructural organization. Cortical bone is stronger in the longitudinal (osteonal) direction than in the transverse direction, and stronger in compression than in tension (Keaveny *et al.*, 1993; Guo, 1997 and 2001; Huiskes *et al.*, 2005; Nordin *et al.*, 2012). In cancellous bone, the strength is highly dependent on the preferred orientation of the trabeculae, which can be quantified by a fabric tensor (Turner, 1992; Odgaard *et al.*, 1997; Hazrati-Marangalou *et al.*, 2015; Hosseini *et al.*, 2017). For this reason, bone strength is often specified as a function of both density and fabric (Keaveny, 2001).

During normal physiological loading, the elastic properties of bone tissue play a major role as these determine the stresses and strains that are sensed by the cells. The elastic properties of bone are usually well described as linear elastic and anisotropic. The anisotropy of cortical bone is well described as transversally isotropic, with the principal orientation aligned with the osteonal orientation. Cancellous bone is better described as orthotropic, with elastic planes of symmetry aligned with the principal trabecular orientations (Keaveny, 2003). To account for this type of anisotropy, the elastic properties of cancellous bone are often specified as a function of its porosity and a fabric tensor (van Rietbergen *et al*., 2001).

Load adaptive Bone remodeling

The strength and elastic properties of bone tissue can change due to bone remodeling. In the healthy case, this enables bone to adapt its stiffness and strength to changes in activity. For example, strenuous exercises can increase bone strength while long time disuse will reduce bone strength. This functional adaptation of bones is generally referred to as "Wolff´s law" (Wolff, 1892), which states that bone density and microarchitecture adapt to the loading it is subjected to. It was proposed already long ago that this adaptation is the results of a "quantitative self-regulating mechanism" regulated by cells (Roux, 1881). At that time, however, it was not possible to test such propositions. During the last decades, computer models based on hypothetical bone remodeling rules have been developed, and these have shown that, indeed, a relatively simple self-organizational process can result in the formation of load-adaptive bone structures and can describe bone adaptation in case of changes in loading (Huiskes, 2000).

Clinical problem: osteoporosis

With aging, the balance between bone formation and resorption becomes unbalanced in favor of resorption, leading to bone loss. Whereas part of this loss is due to lower activity levels, hence the result of load-adaptive bone remodeling, most is actually the result of a deregulation of the load adaptation process which results from hormonal changes (Parfitt *et al*., 1995). This condition of excessive bone loss, called osteoporosis, leads to deterioration of the bone microarchitecture, enhanced bone fragility and increased bone fracture risk due to a fall (Genant *et al*., 1999). Clinically, osteoporosis is defined as a condition where the Bone Mineral Density (BMD) as measured by Dual Energy X-ray Absorptiometry (DEXA) is less than 2.5 standard deviations below that in healthy women at the age of 30 (Compston *et al.*, 2019). Osteoporosis affects mainly trabecular bone, but also contributes to the thinning and increased porosity of the cortical walls (Seeman, 2007). These reductions in trabecular and cortical density are directly associated with a reduction in bone strength (Hayes *et al.*, 1991). As a result, patient suffering from osteoporosis have a higher risk of fragility fractures. Such fractures typically occur at the hip, distal radius and in vertebrae. Treatment options depend on the site of fracture. For hip fractures a total joint replacement is typically the only option. For the distal radius, the treatment depends on the severity of the fracture. For non-displaced fractures, a cast fixation for 6 weeks is the most common treatment that generally will lead to successful healing. In case of displaced fractures, or fractures consisting of multiple fragments, fixation plates possibly in combination with resorbable bone cement can be used to better stabilize the fracture. Vertebral fractures, finally, often remain untreated (or even undetected as they often do not cause pain). If needed, the collapsed vertebrae can be augmented with bone cement (vertebroplasty). It is possible as well to first restore vertebral height before applying the bone cement (kyphoplasty). Treatment is not always possible though. In particular hip fractures are a catastrophic event for elderly. Only about 25% of the elderly will fully recover, why a similar percentage will die due to fracture-related complications in the first year (Malik *et al.*, 2018; Compston *et al.*, 2019). It thus is important to avoid fractures. This, however, requires an accurate diagnosis of bone fracture risk.

Diagnosis of bone fracture risk

From bone density and morphology

As mentioned above, DEXA is presently the most widely used technique to quantify osteoporosis by measuring areal BMD at the hip, spine or other parts of the body. Advantages of this technique are its low radiation dose, short scan time wide availability and easy clinical interpretation (Messina *et al.*, 2018). Whereas DEXA measurements can well identify very osteoporotic and healthy individuals, it is not very sensitive nor specific in predicting fracture risk for other patients. It has been described that only half of the patients that suffer from a major osteoporotic fracture would have been diagnosed as being osteoporotic based on DEXA measurements (McClung, 2006). Several efforts have been made to improve the prediction of bone fracture risk by adding other risk factors to the BMD values (e.g. FRAX) (Whitlock *et al*., 2019). Although these have somewhat improved the sensitivity/specificity of the fracture risk prediction, an accurate prediction still is not possible.

As DEXA can only provide projected images, a major limitation is that it cannot distinguish between cortical and cancellous bone. Also, it cannot measure the true bone density, but only an area-weighted density (often named areal BMD or aBMD). The latter is not only dependent on bone density, but also on bone size. Later studies have therefore proposed quantitative CT (QCT) imaging as a tool for the diagnosis of bone fracture risk. With QCT imaging, it is possible to measure the bone density in a true volumetric way, individually for the cancellous and cortical region. Although this enables a better-defined measure of bone density, results of QCT based analyses for the prediction of bone fracture risk have not been much better than those of DEXA (Davis *et al*., 2013). This relates to the fact that true BMD (unlike aBMD) values are independent of bone size, whereas bone strength obviously is dependent on bone size, and to the fact that the resolution of QCT is not high enough for an adequate representation of the cortex in areas where it is thin (near the joints, and in in vertebrae).

A limitation of both DEXA and QCT is that they can only measure bone density as their resolution is not good enough to recognize the trabecular architecture. With the introduction of High Resolution peripheral Quantitative CT (HR-pQCT) imaging, it has become possible to also image trabecular morphological changes (Boutroy *et al*., 2011; Lespessailles *et al*., 2018; Ramalho *et al*., 2018; Neto *et al*., 2019). A major advantage of this technique is the high resolution (82 or 61 microns isotropic, depending on model type) that enables an accurate representation of the trabecular network and the cortical region. Also, it enables the quantification of changes in bone morphology that would not result in changes in bone density, which is of particular interest when testing new drugs or treatments. Major disadvantages of this technique are the fact that it can be used only to scan the peripheral bones (typically distal radius and distal tibia) and the limited availability (presently around 80 systems worldwide). Several studies have investigated if morphological parameters measured by HR-pQCT are better predictors of bone fracture risk than

DEXA (Pahr *et al*., 2009; Boutroy *et al*., 2011; van Rietbergen, 2015; Butscheidt *et al*., 2018; Fink *et al*., 2018; Samelson *et al*., 2019). Although such studies have found clear differences between fracture patients and controls, it was found that the fracture risk prediction is not much improved.

From finite element modeling

Finite element (FE) modeling has long been proposed to better estimate bone fracture risk. Unlike bone density and morphology parameters, it does not rely on stochastic relationships between density/morphology and bone strength but provides a direct mathematical relationship between the bone internal and external morphology and bone strength. Finite element models can be derived directly from CT scans. The geometry of the model then is manually or automatically derived from the periosteal contour of the bone and subdivided in elements. The element density is derived from the grey-level of the voxels underlying the element (Mulder *et al*., 2004). As this meshing technique can be time consuming, a more popular approach nowadays is the voxel conversion technique, where bone voxels are directly converted to brick elements in the FE model (Keyak *et al*., 1990). While most studies only accounted for bone density to represent the element material properties, later studies also included bone fabric to quantify bone anisotropic properties (Hazrati-Marangalou *et al*., 2015). Whereas FE models can much better predict bone strength than density or morphological analyses, their ability to predict bone fracture risk is less clear. Whereas good results were reported in some studies (Niebur *et al*., 2000; Keyak *et al*., 2011; Kawabata *et al*., 2017; Sternheim *et al*., 2018), other studies did not show a major improvement (Carballido-Gamio *et al*., 2013; Keyak *et al*., 2013).

With the introduction of the HR-pQCT, it became possible as well to perform micro-FE analyses that model that actual bone microstructure (Pistoia et al., 2002; van Rietbergen et al., 2015). Several studies have validated the strength prediction of micro-FE analyses based on HR-pQCT images of the distal radius and found considerable improvements over strength predictions based on DEXA aBMD or other density measures (Pistoia *et al*., 2004; Macneil *et al*., 2008; Varga *et al*., 2010 and 2016; Whittier *et al*., 2018). Micro-FE has also been used in many clinical studies to predict bone fractures. When considering retrospective cross-sectional studies that compare measurements of subjects with fractures with measurements of controls, however, the association of the micro-FE parameters with fractures was not much higher than of DEXA-based parameters (van Rietbergen *et al.*, 2015). This could be contributed to the fact that in such retrospective studies the fracture often occurred many years before the scanning, and many patients were treated with bisphosphonates after the treatment, such that the measured structure did not well reflect the structure at the time of fracture. In a recent study that included results from many prospective studies, it was found that the association between fractures and micro-FE results indeed was much stronger than that of any other parameter investigated (Samelson *et al.*, 2019).

Micro-FE analyses have also been used to measure the stiffness of fractured bone (de Jong *et al.*, 2014). In such studies the fractured region is scanned and micro-FE analyses involving compression/bending tests are simulated. It was found that the calculated stiffness first drops, and only after some 3 weeks the micro-FE calculated stiffness showed a clear increase in stiffness over time. Two years later, the fractured site actually had a higher stiffness than the contralateral site (de Jong *et al.*, 2017a).

Presently, however, it is still unclear what the accuracy of such micro-FE analyses of fractured bone are as unlike with intact bone, an experimental validation is not feasible. It seems likely that several systematic errors will occur, such as the fact that trabeculae that touch will be considered to be bonded and the fact that bone tissue itself may be damaged, but that this cannot be derived from the images. It was proposed that such artefacts could explain, for example, the initial drop in stiffness seen in the fracture healing studies (de Jong *et al.*, 2014). Similar problems may occur for bone that is treated by plates and cement after a fracture. Metal plates may lead to severe imaging artefacts, although these can be avoided by using other materials (de Jong *et al.*, 2017b). The cement can be visualized with HR-pQCT as these cements are radiopaque, but it presently is unclear to what extent the stiffness of bone treated with cement can be predicted by micro-FE or other analyses.

Thesis outline

The first goal of this thesis therefore was to investigate to what extent micro-FE analysis based on high resolution CT-images can accurately estimate material properties of intact and damaged bone tissue. To reach this goal, first the ability of micro-FE analysis to estimate the compressive stiffness of cancellous bone samples after a fracture was tested (chapter 2). Subsequently, the stiffness after cementing a fractured sample was measured and compared to the fractured and unfractured situation (chapter 3). In this study also, micro-FE was used in order to test if it can predict the stiffness of cemented bone.

As mentioned in the introduction above, however, the first goal of diagnosis should be to avoid bone fractures. The other chapters in this thesis therefore focus on the bone strength prediction. In chapter 4, this is done for small animal models. In such studies bone strength is often measured using three-point bending tests, the results of which then are analyzed by beam theory. In this chapter we investigate the accuracy of this approach for rat femur bone. In chapter 5 we then move to the mechanical analysis of human bone strength based on HR-pQCT in-vivo scans. Although this method has been validated in several studies for the first generation of this type of scanner, there was no validation yet for the second generation of HR-pQCT devices, even though it was clear that strength and stiffness parameters may need to be changed. The goal of this chapter therefore was to establish optimal parameters when performing micro-FE and also homogenized FE analyses.

REFERENCES

Aarden E.M., Burger E.H., Nijweide P.J., 1994. Function of osteocytes in bone. *Journal of Cellular Biochemistry* 5b5, 287–99.

Boutroy S., Vilayphiou N., Roux J., Delmas P.D., Blain H., Chapurlat R.D., Chavassieux P., 2011. Comparison of 2D and 3D bone microarchitecture evaluation at the femoral neck, among postmenopausal women with hip fracture or hip osteoarthritis. *Bone* 49, 1055-1061.

Buckwalter J.A., Glimcher M.J., Cooper R.R., Recker R., 1995. Bone Biology. Part I: structure, blood supply, cells, matrix, and mineralization. Part II: Formation, form, remodelling and regulation of cell function. *Journal of Bone and Joint Surgery* 77A, 1256-1289.

Butscheidt S., Rolvien T., Vettorazzi E., Frieling I., 2018. Trabecular bone microarchitecture predicts fragility fractures in postmenopausal women on denosumab treatment. *Bone* 114, 246-251.

Burr D.B., 2019. Bone Morphology and Organization. In: Burr D.B., Allen M.R. (eds.). Basic and Applied Bone Biology (Second Edition). Academic Press, Cambridge, MA, USA. pp 3-26.

Carballido-Gamio J., Harnish R., Saeed I., Streeper T., Sigurdsson s., Amin S., Atkinson E.J., Therneau T.M., Siggeirsdottir K., Cheng X., Melton L.J., Keyak J.H., Gudnason V., Khosla S., Harris T.B., Lang T.F., 2013. Structural patterns of the proximal femur in relation to age and hip fracture risk in women. *Bone* 57, 290-299.

Compston J.E., McClung M.R., Leslie W.D., 2019. Osteoporosis. *The Lancet* 393, 364-376.

Crockett J.C., Rogers M.J., Coxon F.P., Hocking L.J., Helfrich M.H., 2011. Bone remodeling at a glance. *Journal of Cell Science* 124(7), 991-998.

Davis E.T., Olsen M., Zdero R., Smith G.M., Waddell J.P., Schemitsch E.H., 2013. Predictors of Femoral Neck Fracture Following Hip Resurfacing: A Cadaveric Study. *The Journal of Arthroplasty* 28, 110-116.

de Jong J.J.A, Willems P.C., Arts J.J.C., Bours S.G.P., Brink P.R.G., van Geel T.A.C.M., Poeze M., Geusens P.P., van Rietbergen B., van den Bergh J.P.W., 2014. Assessment of the healing process in distal radius fractures by high resolution peripheral quantitative computed tomography. *Bone* 64, 65-74.

de Jong J.J.A., Arts J.J.C., Willems P.C., Bours S.P.G., Bons J.P.A., Menheere P.P.C.A., van Rietbergen B., Geusens P.P., van den Bergh J.P.W., 2017a. Contra-lateral bone loss at the distal radius in postmenopausal women after a distal radius fracture: A two-year follow-up HRpQCT study. *Bone* 101, 245-251.

de Jong J.J.A., Lataster A., van Rietbergen B., Arts J.J.C., Geusens P.P., van den Bergh JP, Willems P.C., 2017b. Distal radius plate of CFR-PEEK has minimal effect compared to titanium plates on bone parameters in high-resolution peripheral quantitative computed tomography: a pilot study. *BMC Medical Imaging* 17, 18.

Fink H.A., Langsetmo L., Vo T.N., Orwoll E.S., Schousboe J.T., Ensrud K.E., 2018. Association of High-resolution Peripheral Quantitative Computed Tomography (HR-pQCT) bone microarchitectural parameters with previous clinical fracture in older men: The Osteoporotic Fractures in Men (MrOS) study. *Bone* 113, 49-56.

Frost, H. M., 1986. Intermediary Organization of the Skeleton, Volume I. CRC Press, Boca Raton, FL, USA. pp. 1–365.

Geddes, A., 1996. Animal models of bone disease. In: Bilezikian J., Raisz L., Rodan G., (eds.). Principles of Bone Biology, Academic Press, San Diego, CA, USA. pp. 1343–1354.

Genant H.K., Cooper C., Poor G., Reid I., Ehrlich G., Kanis J., Nordin B.E., Barrett-Connor E., Black D., Bonjour J.P., Dawson-Hughes B., Delmas P.D., Dequeker J., Ragi E.S., Gennari C., Johnell O., Johnston C.C. Jr., Lau E.M., Liberman U.A., Lindsay R., Martin T.J., Masri B., Mautalen C.A., Meunier P.J., Khaltaev N., et al., 1999. Interim report and recommendations of the World Health Organization Task-Force for Osteoporosis. *Osteoporosis International* 10, 259-264.

Goodship A.E., Cunningham J.L., 2001. Pathophysiology of Functional Adaptation of bone in remodeling and repair in vivo. In: Cowin S. Bone Mechanics Handbook. 2nd edition, CRC Press, Boca Raton, FL, USA.

Guo X.E., Goldstein S.A., 1997. Is trabecular bone tissue different from cortical bone tissue?. *Forma* 12, 185-196.

Guo X.E., 2001. Mechanical properties of cortical bone and cancellous bone tissue. In: Cowin S. Bone Mechanics Handbook. 2nd edition, CRC Press, Boca Raton, FL, USA.

Hayes W.C., Piazza S.J., Zysset P.K., 1991. Biomechanics of fracture risk prediction of the hip and spine by quantitative computed tomography. *Radiologic Clinics of North America* 29, 1-18.

Hazrati-Marangalou J., Ito K., van Rietbergen B., 2015. A novel approach to estimate trabecular bone anisotropy from stress tensors. *Biomechanics and Modeling in Mechanobiology* 14, 39–48.

Hollinger J.O., 2005. Bone Dynamics. Morphogenesis, Growth, Modeling and Remodeling. In: Lieberman J., Friedlaender G., Bone regeneration and repair, Biology and clinical applications. Humana Press Springer, New York, USA. pp 8-14.

Hosseini H.S., Dünki A., Fabech J., Stauber M., Vilayphiou N., Pahr D., Pretterklieber M., Wandel J., van Rietbergen B., Zysset P.K., 2017. Fast estimation of Colles' fracture load of the distal section of the radius by homogenized finite element analysis based on HR-pQCT. *Bone* 97, 65–75.

Huiskes R., 2000. If bone is the answer, then what is the question? *Journal of Anatomy* 197, 145-156.

Huiskes R., van Rietbergen B., 2005. Biomechanics of Bone. In: Mow C., Huiskes R. (editors), Basic Orthopaedic Biomechanics and Mechano-Biology, 3rd Edition. Lippincott Williams & Wilkins, Philadelphia, USA.

Kawabata Y., Matsuo K., Nezu Y., Kamiishi T., Inaba Y., Saito T., 2017. The risk assessment of pathological fracture in the proximal femur using a CT-based finite element method. *Journal of Orthopaedic Science* 22, 931-937.

Keaveny T.M., Hayes W.C., 1993. Mechanical properties of cortical and trabecular bone. *Bone* 7, 285-344.

Keaveny T.M., 2001. Strength of trabecular bone. In: Cowin S. Bone Mechanics Handbook. 2nd edition, CRC Press, Boca Raton, FL, USA.

Keaveny T.M., Morgan E.F., Yeh O.C., 2003. Bone Biomechanics. In: Kutz M. (editor), Biomedical Engineering and Design Handbook, Volume 1, McGraw-Hill Professional, New York, USA.

Keyak J.H., Meagher J.M., Skinner H.B., Mote C.D., 1990. Automated three-dimensional finite element modelling of bone: a new method. *Journal of Biomedical Engineering* 12, 389-397.

Keyak J.H., Sigurdsson S., Karlsdottir G., Oskarsdottir D., Sigmarsdottir A., Zhao S., Kornak J., Harris T.B., Sigurdsson G., Jonsson B.Y., Siggeirsdottir K., Eiriksdottir G., Gudnason V., Lang T.F., 2011. Male–female differences in the association between incident hip fracture and proximal femoral strength: A finite element analysis study. *Bone* 48, 1239-1245.

Keyak J.H., Sigurdsson S., Karlsdottir G.S., Oskarsdottir D., Sigmarsdottir A., Kornak J., Harris T.B., Sigurdsson G., Jonsson B.Y., Siggeirsdottir K., Eiriksdottir G., Gudnason V., Lang T.F., 2013. Effect of finite element model loading condition on fracture risk assessment in men and women: The AGES-Reykjavik study. *Bone* 57, 18-29.

Kohrt W.M., Villalon K.L., Barry D.W., 2013. Effects of exercise and physical interventions on bone: clinical studies. In: Silva M.J. (Ed.). Skeletal aging and osteoporosis, biomechanics and mechanobiology. 1st ed., Springer-Verlag Berlin Heidelberg, Berlin, Germany.

Kotiya A.A., Silva M.J., 2013. The effect of aging on skeletal mechanoresponsiveness: animal studies. In: Silva M.J. (Ed.). Skeletal aging and osteoporosis, biomechanics and mechanobiology. 1st ed., Springer-Verlag Berlin Heidelberg, Berlin, Germany.

Kular J., Tickner J., Chim S.M., Xu J., 2012. An overview of the regulation of bone remodelling at the cellular level. *Clinical Biochemistry* 45, 863-873.

Lespessailles E., Ibrahim-Nasser N., Toumi H., Chapurlat R., 2018. Contribution of high resolution peripheral quantitative CT to the management of bone and joint diseases. *Joint Bone Spine* 85, 301-306.

Lieberman J., Friedlaender G., 2005. Bone regeneration and repair, Biology and clinical applications. Humana Press Springer, New York, USA.

MacNeil J.A., Boyd S.K., 2008. Bone strength at the distal radius can be estimated from high-resolution peripheral quantitative computed tomography and the finite element method. *Bone* 42, 1203-1213.
Majeska R.J., 2001. Cell biology of Bone. In: Cowin S. Bone Mechanics Handbook. 2nd edition, CRC Press, Boca Raton, FL, USA.

Malik A.T., Panni U.Y., Masri B.A., Noordin S., 2018. The impact of surgeon volume and hospital volume on postoperative mortality and morbidity after hip fractures: A systematic review. *International Journal of Surgery* 54, 316-327.

Manolagas S.C., 2000. Birth and death of bone cells basic regulatory mechanisms and implications for the pathogenesis and treatment of osteoporosis. *Endocrine Reviews* 21, 115–37.

Matsuo K., Irie N., 2008. Osteoclast–osteoblast communication. *Archives of Biochemistry and Biophysics* 473, 201-209.

McClung M.R., 2006. Do current management strategies and guidelines adequately address fracture risk? *Bone* 38, 13-17.

Messina C., Lastella G., Sorce S., Piodi L.P., Rodari G., Giavoli C., Marchelli D., Guglielmi G., Ulivieri F.M., 2018. Pediatric dual-energy x-ray absorptiometry in clinical practice: what the clinicians need to know. *European Journal of Radiology* 105, 153-161.

Meyer U., Wiesmann H.P., 2006. Bone and Cartilage Engineering. Springer-Verlag, Berlin, Germany.

Mulder L., Koolstra J.H., van Eijden T.M.G.J., 2004. Accuracy of microCT in the quantitative determination of the degree and distribution of mineralization in developing bone. *Acta Radiologica* 45, 769-777.

Neto N.S.R., Bento J.C.B., Takayama L., Caparbo V.F.,Pereira R.M.R., 2019. Bone microarchitecture as measured using HR-pQCT of male Fabry disease patients and GLA gene GVUS subjects. *Molecular Genetics and Metabolism* 126, S126.

Niebur G.L., Feldstein M.J., Yuen J.C., Chen T.J., Keaveny T.M., 2000. High-resolution finite element models with tissue strength asymmetry accurately predict failure of trabecular bone. *Journal of Biomechanics* 33, 1575-1583.

Nordin M., Frankel V.H., 2012. Basic Biomechanics of the Musculoskeletal System. 4rd edition. Lippincott Williams & Wilkins, Philadelphia, USA.

Odgaard A., Kabel J., van Rietbergen B., Dalstra M., Huiskes R., 1997. Fabric and elastic principal directions of cancellous bone are closely related. *Journal of Biomechanics* 30, 487-495.

Pahr D.H., Zysset P.K., 2009. From high-resolution CT data to finite element models: development of an integrated modular framework. *Computer Methods in Biomechanics and Biomedical Engineering* 12, 45-57.

Parfitt M. A., 1983. The physiologic and clinical significance of bone histomorphometric data. In: Recker R.R. (ed.). Bone Histomorphometry: Techniques and Interpretation. CRC Press, Boca Raton, FL, USA. pp 143–224.

Parfitt A.M., 1994. Osteonal and hemi-osteonal remodeling: the spatial and temporal framework for signal traffic in adult human bone. *Journal of Cellular Biochemistry* 55, 273–286.

Parfitt A.M., Villanueva A.R., Foldes J., Rao D.S., 1995. Relations between histologic indices of bone formation: implications for the pathogenesis of spinal osteoporosis. *Journal of Bone and Mineral Research* 10(2), 466–473.

Piekarski K., 1973. Analysis of bone as a composite material. *International Journal of Engineering Science* 11, 557-565.

Pistoia W., van Rietbergen B., Lochmüller E.M., Lill C.A., Eckstein F., Rüegsegger p., 2002. Estimation of distal radius failure load with micro-finite element analysis models based on three-dimensional peripheral quantitative computed tomography images. *Bone* 30, 842-848.

Pistoia W., van Rietbergen B., Lochmüller E.M., Lill C.A., Eckstein F., Rüegsegger P., 2004. Image-Based Micro-Finite-Element Modeling for Improved Distal Radius Strength Diagnosis: Moving From “Bench” to “Bedside”. *Journal of Clinical Densitometry* 7, 153-160.

Ramalho J., Marques I.D.B., Hans D., Dempster D., Zhou H., Patel P., Pereira R.M.R., Jorgetti V., Moyses R.M.A., Nickolas T.L, 2018. The trabecular bone score: Relationships with trabecular and cortical microarchitecture measured by HR-pQCT and histomorphometry in patients with chronic kidney disease. *Bone* 116, 215-220.

Recker R.R. (ed.), 1983. Bone Histomorphometry: Techniques and Interpretation. CRC Press, Boca Raton, FL, USA. pp 1–306.

Rho J.Y., Kuhn-Spearing L., Zioupos P., 1998. Mechanical properties and the hierarchical structure of bone. *Medical Engineering & Physics* 20, 92-102.

Rossen C.J., 2003. Anatomy, Physiology and Disease. In: Langton C.M., Njeh C.F. (eds.). The Physical Measurement of Bone. First ed. CRC Press, Boca Raton, FL, USA.

Roux W., 1881. Der Kampf der Teile im organismus. Leipzig: Engelmann.

Samelson E.J., Broe K.E., Xu H., Yang L., Boyd S., Biver E., Szulc P., Adachi J., Amin S., Atkinson E., Berger C., Burt L., Chapurlat R., Chevalley T., Ferrari S., Goltzman D., Hanley D.A., Hannan M.T., Khosla S., Liu C.T., Lorentzon M., Mellstrom D., Merle B., Nethander M., Rizzoli R., Sornay-Rendu E., Van Rietbergen B., Sundh D., Wong A.K.O., Ohlsson C., Demissie S., Kiel D.P., Bouxsein M.L., 2019. Cortical and trabecular bone microarchitecture as an independent predictor of incident fracture risk in older women and men in the Bone Microarchitecture International Consortium (BoMIC): a prospective study. *The Lancet Diabetes and Endocrinology* 7, 34-43.

Seeman E., 2007. Bone's material and structural strength. *Journal of Bone and Mineral Metabolism* 26, 1-8.

Silva M.J. (Ed.), 2013. Skeletal aging and osteoporosis, biomechanics and mechanobiology. 1st ed., Springer-Verlag Berlin Heidelberg, Berlin, Germany.

Sternheim A., Giladi O., Gortzak Y., Drexler M., Salai M., Trabelsi N., Milgrom C., Yosibash Z., 2018. Pathological fracture risk assessment in patients with femoral metastases using CT-based finite element methods. A retrospective clinical study. *Bone* 110, 215-220.

Turner C.H., 1992. On Wolff's law of trabecular architecture. *Journal of Biomechanics* 25, 1-9.

van Rietbergen B., Huiskes R., 2001. Elastic constants of cancellous bone. In: Cowin S. Bone Mechanics Handbook. 2nd edition, CRC Press, Boca Raton, FL, USA.

van Rietbergen B., Ito K., 2015. A survey of micro-finite element analysis for clinical assessment of bone strength: the first decade. *Journal of Biomechanics* 48, 832–841.

Varga P., Pahr D.H., Baumbach S., Zysset P.K., 2010. HR-pQCT based FE analysis of the most distal radius section provides an improved prediction of Colles' fracture load in vitro. *Bone* 47, 982-988.

Varga P., Schwiedrzik J., Zysset P.K., Fliri-Hofmann L., Widmer D., Gueorguiev B., Blauth M., Windolf M., 2016. Nonlinear quasi-static finite element simulations predict in vitro strength of human proximal femora assessed in a dynamic sideways fall setup. *Journal of the Mechanical Behavior of Biomedical Materials* 57, 116-127.

Vaz M.F., Canhão H., Fonseca J.E., 2011. Bone: A Composite Natural Material. In: Těšinova P. (Ed.). Advances in Composite Materials. IntechOpen, London, UK.

Whitlock R.H., Leslie W.D., Shaw J., Rigatto C., Thorlacius L., Komenda P., Collister D., Kanis J.A., Tangri N., 2019. The Fracture Risk Assessment Tool (FRAX®) predicts fracture risk in patients with chronic kidney disease. *Kidney International* 95, 447-454.

Whittier D.E., Manske S.L., Kiel D.P., Bouxsein M., Boyd S.K., 2018. Harmonizing finite element modelling for non-invasive strength estimation by high-resolution peripheral quantitative computed tomography. *Journal of Biomechanics* 80, 63–71.

Wolff J., 1892. Das Gesetz der Transformation der Knochen. Springer-Verlag Berlin Heidelberg, Berlin, Germany.

Chapter 2

Micro-Finite Element analysis will overestimate the compressive stiffness of fractured cancellous bone

The content of this chapter is based on:
Arias-Moreno A.J., Ito K., van Rietbergen B., 2016. Micro-Finite Element analysis will overestimate the compressive stiffness of fractured cancellous bone. *Journal of Biomechanics* 49, 2613-2618.

ABSTRACT

Recently, micro-Finite Element (micro-FE) analysis based on High Resolution peripheral Quantitative CT (HRpQCT) images was introduced to quantify the state of fracture healing (de Jong et al., 2014). That study suggested that the direct post-fracture stiffness may be overestimated by micro-FE. The aim of this study was to investigate this further by measuring the loss in stiffness of cancellous bone samples under compressive loading and to compare this with predictions based on micro-FE analyses and bone microstructural and fracture morphology. Sixty porcine trabecular cores were micro-CT scanned and tested in compression before and after inducing a fracture in 4 different manners. The loss in stiffness as measured in the experiment was compared to that calculated from micro-FE analysis. Additionally, bone morphology parameters and fracture thickness were calculated. The experimentally measured loss in stiffness ranged from 37% to 80%. The losses calculated from the micro-FE analyses were lower and ranged from 36% to 61%, while in one case an increase in stiffness was calculated. For 2 of the 4 experiments, the results of the experiment and micro-FE analyses were significantly different. Only for very smooth fractures good agreement was obtained between FE and experimental results. The loss in stiffness did not correlate with any investigated bone morphology parameter or the thickness of the fracture region. It was concluded that micro-FE analysis can severely overestimate the stiffness of fractured bone depending on the type of fracture, but in the case of smooth fractures good estimates are possible.

INTRODUCTION

In recent studies, micro-Finite Element (micro-FE) analysis based on High Resolution peripheral Quantitative CT (HRpQCT) images has been introduced as a new tool to quantify the state of fracture healing for distal radius fractures (de Jong *et al.*, 2014; Meyer *et al.*, 2014). With this approach, the in-vivo microstructural geometry of the fractured bone region is represented by a 3D finite element model and the stiffness of that region is calculated by simulating a compression or bending test. The consolidation of the fracture is then quantified by the increase in stiffness over time. It was demonstrated that such an approach can detect significant increases in bone mechanical properties as expected during healing. Interestingly, however, the micro-FE approach predicts that the stiffness of the fractured region will first drop, and only increases after 3 weeks of healing (de Jong *et al.*, 2014).

A possible explanation for this effect, that is eluded as well in the earlier study, could be that the micro-FE approach overpredicts the stiffness of the fractured region just after the fracture occurred. There are two major reasons why this could be the case. First, in the fractured region, trabeculae from both fracture sides might touch or interlock to each other. In the HR-pQCT images, such touching and interlocking trabeculae appear to be connected. As a consequence, in the micro-FE models these trabeculae will be modelled as connected rather than fractured, thus leading to an overestimation of the stiffness. Second, due to the fracture, large deformations occur in trabecula, which leads to damage accumulation and consequent degradation of their material properties. Since the accumulated damage is not visible in the HR-pQCT images, it will not be accounted for in the micro-FE models. Both these factors could result in an overestimation of the calculated stiffness, and it is only after remodelling has taken place and a new connected bone structure has been formed, that the micro-FE analysis is expected to provide good estimates of the stiffness of the healing region.

Whereas it thus is likely that micro-FE analysis will not accurately predict the bone stiffness just after the fracture is formed, presently no information is available about the severity of this error, and if this error relates to the type of fracture (e.g. it may be more severe for irregular than for smooth fractures), the trabecular architecture (e.g. it may be more severe in low density bone than in high density bone) or the fracture morphology (e.g. it may be more severe for fractures with a large damage region than for fractures with a narrow damage region). In the present study we therefore aim at comparing the loss in stiffness predicted by micro-FE analyses with those measured in an experimental test for bone samples for which high-resolution images and stiffness measurements were obtained before and after different types of fractures were artificially created. Specific goals were first, to measure the loss in stiffness under compressive loading for different types of induced fractures and to compare these measurements with predictions based on micro-FE analyses. A second goal was to investigate whether the loss in stiffness is related to the bone microstructural morphology or the fracture morphology. Bone microstructural and fracture morphology were assessed from the same micro-CT scans using 3D morphology measures and image registration techniques.

MATERIALS AND METHODS

Material

Sixty cylindrical trabecular bone samples (7.5 mm diameter) were obtained from porcine proximal tibiae using a hollow drill irrigated with PBS. The longitudinal axis of the samples was normal to the tibia plateau. After drilling, the samples were cut at both ends to a length of 10 mm using a diamond blade saw to ensure plan-parallel ends. Bone marrow was left inside during the whole procedure and care was taken that the samples did not contain any part of the physis.

MicroCT scanning and mechanical testing

Each sample was scanned in a micro-CT (µCT 80, Scanco Medical AG, Switzerland) at a resolution of 20 µm (Voltage 70 kVp; Intensity 114 µA; Integration time 300 ms) in air in a closed holder. After scanning, all samples were subjected to a non-destructive compression test to determine their stiffness (Fig. 1). For testing, metal endcaps were glued to the ends of the specimen to reduce the end-artefact effects (Linde, 1994; Keaveny *et al.*, 1994). A pre-load of 20 N was applied to the specimen four times after which the load was increased till 200 N, corresponding to a stress of around 4.5 MPa, at a speed of 0.1 mm/min (Universal testing machine BT1-FB010TND30, Zwick/Roell, Germany). At this level, the elastic behaviour was still in the linear elastic range for all samples tested. An optical measurement system (VideoXtens multicamera extensometer, Zwick/Roell, Germany) was used as extensometer to measure strain directly at the sample's surface. By fitting a line to the region of 100 – 200 N of the force-displacement curve, the experimental stiffness was determined.

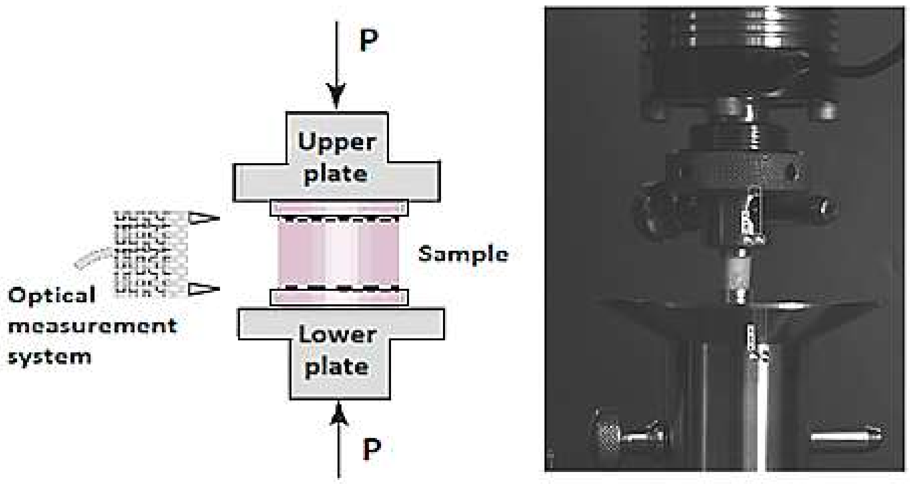

Figure 1. Scheme of the compression test measured by the optical measurement system (left) and a measurement image obtained from this optical measurement system (right).

Inducing fractures

The 60 samples were divided into three groups of 20 samples each. Samples in the first group were transversely cut at their mid-section using a diamond-blade saw (DS group) (Fig. 2a), representing an osteotomy. Samples in the second group were "fractured" by pulling a 0.4 mm diameter steel cable through their centre while supporting their ends (SC group) (Fig. 2b), creating a shearing stress fracture. Samples in the third group were fractured by a drop weight: 0.5 kg, 20 cm fall-height (Fig. 2c). In half of the samples (n=10), compressive impact was applied (CI group), in the other half (n=10) a 3-point bending impact (BI group). These last mechanisms created an impacted fracture (where bone fragments are driven into each other) and a comminuted fracture, respectively.

Diamond-blade Saw
(DS group)

Steel Cable
(SC group)

Impact Force
(CI and BI groups)

Figure 2. Different methods to induce a fracture inside the bone samples: (A) by a diamond-blade saw (DS group), (B) by a steel cable (SC group) and, (C) by impact load (CI and BI groups) (C). In this last, compression direction is shown.

After the fracture was created, the two parts of the sample were put together in their original position and micro-CT scanning and mechanical test measurements were repeated. No efforts were taken to precisely align the two parts of the samples and in particular for the samples that were cut with the diamond blade saw, it was possible that both ends were slightly rotated relative to each other compared to the intact case. When the fractures were complete, the main two halves were put together in their original position together with any other smaller fragments. Fragments were not held together during the second test.

Image analysis

Micro-CT image processing included gauss filtering (sigma=2, support=0.8 voxels) and segmentation of the bone phase using a global threshold of 220 per mile of the maximum grey value, corresponding to 483 mg HA/ccm. From the segmented images, the following morphology indices were determined for the cylindrical region encompassing the specimen: Bone volume fraction (BV/TV), Trabecular number (Tb.N), Trabecular Thickness (Tb.Th), Trabecular Space (Tb.Sp), and Structural Model Index (SMI). To better quantify the morphology of the fracture itself, an image registration technique similar to one that was described earlier was applied (Tassani *et al.*, 2014). With this technique, the image of one fractured part of a sample was registered to its intact image using rigid image registration (Ellouz *et al.*, 2014). After registration, only the bone voxels that are present in both images are segmented. After removing unconnected parts, a dilation operation with a distance of 30 voxels was performed, effectively filling the inter-trabecular space in the registered region. Following, an erosion operation with the same distance was applied, bringing back the volume to its original size. Finally, a strong gauss filter (sigma=20, support=30 voxels) was applied and the resulting image was thresholded (threshold= 500 per mile). In this way a solid volume was obtained that represents the intact part of the sample. By performing this operation for both fragments of each sample, the non-damaged part of each sample could be indicated, and the part of the sample that was not within these two regions was considered the fracture region (Fig. 3). The average thickness of this fracture region (Fx.Th) was quantified using a distance transformation function that measured the shortest distance between the two fracture sites. This value then was used as a measure of fracture morphology.

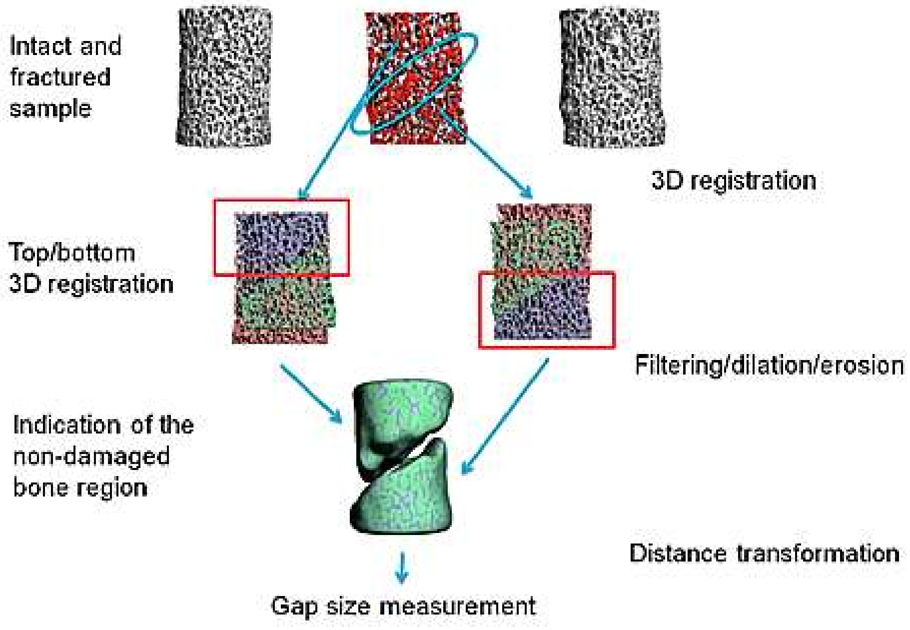

Figure 3. Scheme of the implemented image registration procedure to quantify the morphology of the fracture.

Micro-FE

The segmented images were converted to micro-FE models using a voxel conversion procedure (van Rietbergen *et al*., 1995). In addition, models with a resolution of 40, 60 and 80 micron voxel size were generated by downscaling the original images and these were converted to micro-FE models as well. The latter was done to enable a clinical translation of the results since 60 and 80 micron resolutions can be obtained in-vivo. A compression test was first simulated (E = 1 GPa) to determine an initial stiffness of each intact specimen. The tissue Young's modulus was then calculated such that the experimental and the micro-FE calculated stiffness matched. This modulus was used for all later micro-FE simulations for that specimen. The Poisson's ratio was set to 0.3. All image processing and micro-FE analyses were performed using IPL v5.16 (Scanco Medical AG, Switzerland).

Analysis of results

The change in compressive stiffness due to the fracture then was quantified as:

$$\Delta K[\%] = \frac{K^{cut} - K^{intact}}{K^{intact}} * 100 \tag{1}$$

where K^{intact} is the stiffness for the intact specimen and K^{cut} is the stiffness after the fracture was made. This change in stiffness was calculated both for the micro-FE calculated and for the experimentally measured stiffness to investigate to what extent the micro-FE models can reproduce the experimental results.

Statistical analysis

To investigate differences in the loss in stiffness for different fracture types and differences between measured and FE-predicted values, a mixed two-way ANOVA was performed with one factor representing the fracture-type (the 4 types of fracture) and the other factor the analysis-approach (experiment or FE-analysis at different resolutions). A repeated measure was used in the analysis-approach factor and a Bonferroni post-hoc test was used to test for significance of differences between groups and between experimental and FE-results. The Shapiro-Wilk’s test was used to test the normality of the distribution, which was found to be acceptable (p>0.05) for all the types of fracture at all types of analysis.

Furthermore, a one-way ANOVA with the fracture-generation approach as the independent factor and the measured fracture thickness as the dependent variable was conducted to determine if the fracture thickness was different for groups with different type of induced fracture. A check for the assumptions of normality of the distribution was made using the Shapiro-Wilk's test and that of homogeneity of variances was assessed by the Levene's test of homogeneity of variances. Both assumptions were found to be acceptable ($p>0.05$).

Finally, to investigate to what extent this experimentally measured change in stiffness correlates with the initial bone microstructure morphology and the fracture morphology, correlation coefficients between the change in stiffness as measured in the experiment and the different morphology parameters were calculated, both for the different groups and for the pooled data. A multiple regression analysis then was performed on the pooled data to investigate if any combination of morphology parameters could lead to improved predictions of the change in stiffness due to a fracture.

RESULTS

The micro-CT images of the fractured samples revealed the different morphologies of the different induced fractures (figure 4 top). The cut made by the diamond-blade saw produced a smooth cut, difficult to recognize on the micro-CT scan for the DS group, but the other approaches to induce a fracture create substantial damage to the structure locally. For the SC group, damage is concentrated in a confined cross section where the cable was pulled. The CI group generally showed an oblique densification area whereas the BI group generally showed a more varied fracture shape and location. All these fracture morphologies were in good agreement with the expected morphologies depending on the respective applied mechanism to induce the fracture.

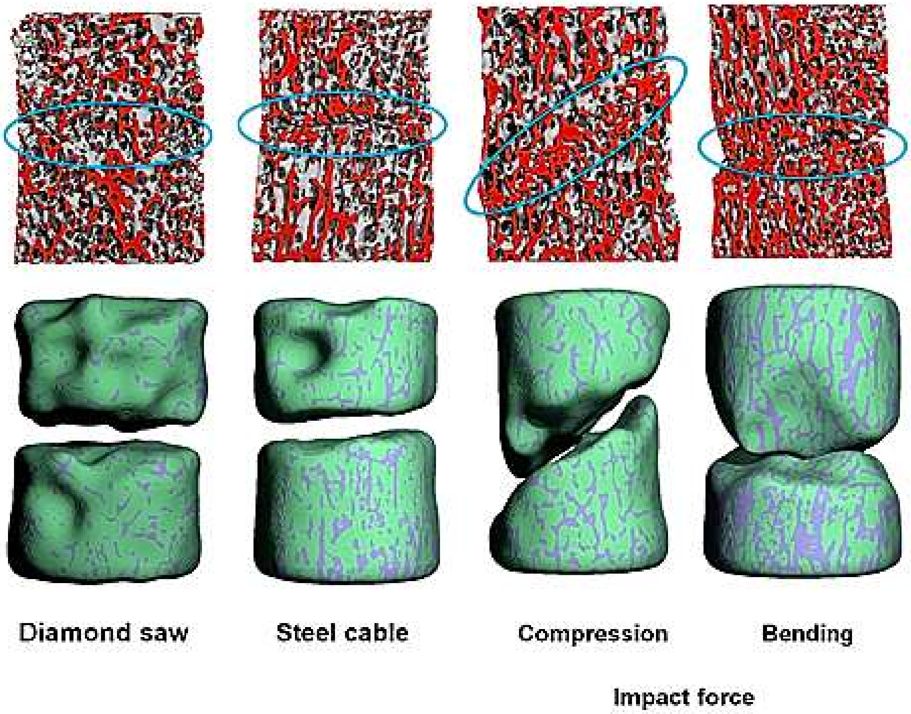

Figure 4. Micro-CT image-based models of the fractured samples (top) and the non-damaged bone models (bottom).

Whereas it was thus difficult to identify the fracture region by visual inspection, the image registration procedure resulted in a clear identification of non-damaged and damaged regions (Fig. 4 bottom). The calculated fracture thickness (mean±SD) was 0.51±.81 [mm] for the DS group, 1.38±.30 [mm] for the SC group, 2.61±1.35 [mm] for the CI group and 0.91±.21 [mm] for the BI group. The one-way Anova analysis, however, revealed that these differences were not significant (p=0.078). It should be noted that for the DS group, the calculated Fx.Th was found to be 1.51 mm, but this was largely determined by the thickness of the saw blade, therefore the Fx.Th for this case was corrected to 0.51 [mm] (Fig. 5).

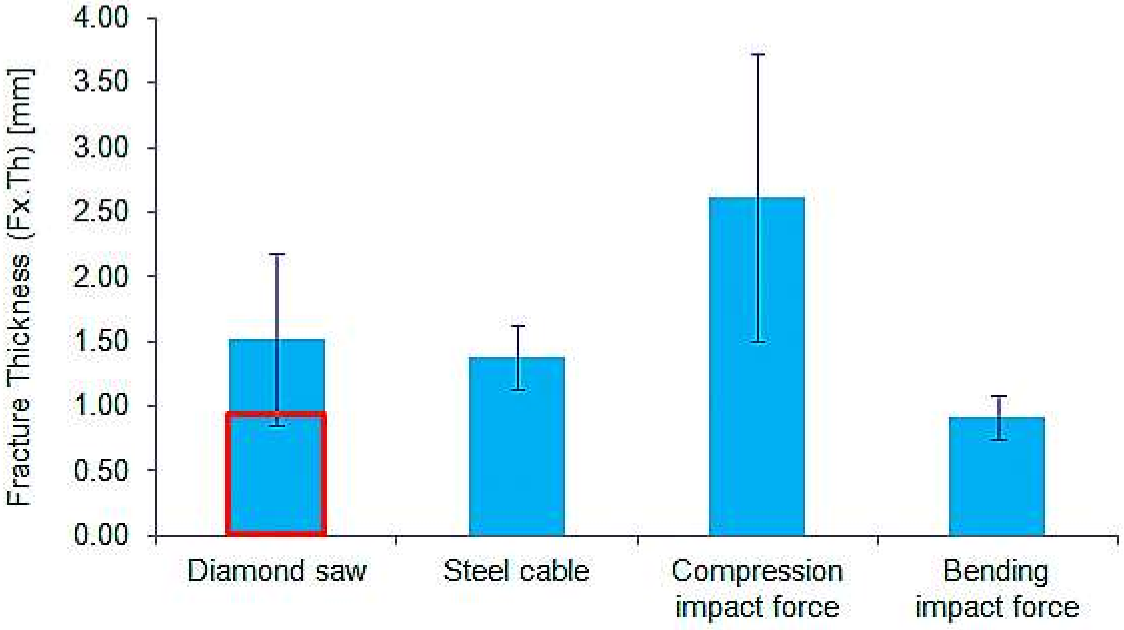

Figure 5. Fracture thickness (Fx.Th) for all cases of fracture. The red region represents the material grinded by the applied mechanism to induce the fracture.

A dramatic loss in experimentally measured stiffness due to the fracture was found for all specimens (Fig. 6). On average, the loss in stiffness was 37% for the DS group, 86% for the SC group, 76% for the CI group and 76% for the BI group. The Anova analysis revealed significant differences between the loss in stiffness measured for the DS group and any of the other groups (Table 1). Results for the other groups, however, did not differ significantly from each other.

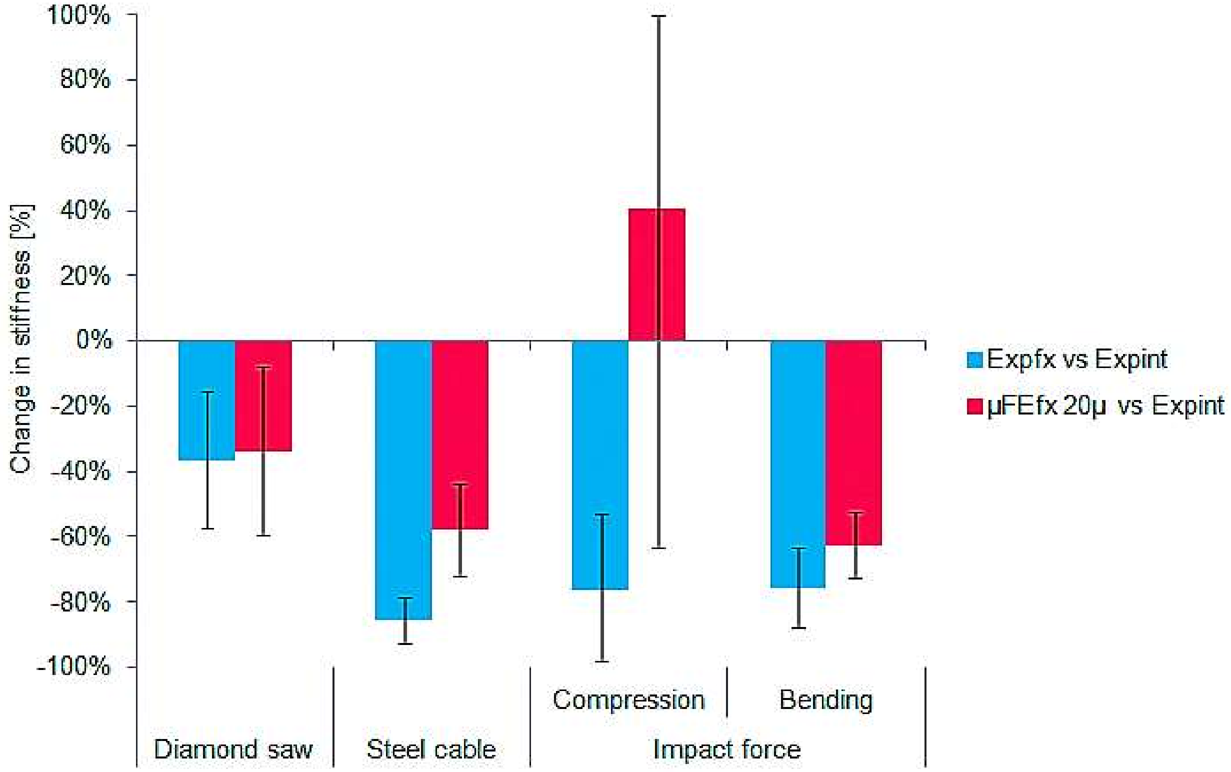

Figure 6. Change in stiffness measured after the fractures were induced on the specimens for the fractures created by the diamond blade saw, the steel cable, the compression impact force, and the three-point bending impact force. The blue bars represent the experimental loss in stiffness while the red bars represent the micro-FE predicted loss in stiffness at 20 microns voxel size.

For the DS group, the average loss in stiffness predicted by the FE-analyses agreed well with the experimental results (predicted loss in stiffness: 33-39 %, depending on resolution), for the other cases, however, the loss in stiffness predicted by the FE-analyses was less than measured in the experiment. For the CI group, on average the micro-FE analyses even predicted an increase in stiffness after fracture. Also for this case, very large standard deviations were found for the predictions.

The Anova analysis revealed no significant differences between experimental and FE-predicted loss in stiffness for the DS group (Table 2). Also for the BI group, the experimental and FE-predicted results were not significantly different for most resolutions used. For the SC and CI groups, however, differences were significant ($p<0.0001$).

Correlations between the morphology parameters and the loss in stiffness revealed no significant correlations (Table 3) except for trabecular thickness in the BI group. Further analysis, however, revealed that this high value was mainly due to the presence of an influential point and it thus was considered an unreliable correlation (Rosner, 2011). When excluding this point, no significant correlation was found (R=0.468, p=0.204). Also a non-parametric analysis revealed no significant correlation (rho=0.527, p=.117). For these reasons, this correlation was not further considered. The multiple linear regression analysis performed for the pooled data set to investigate if any combination of morphology parameters would better correlate with the change in stiffness due to a fracture revealed that no combination of morphological parameters would reach a coefficient of determination exceeding 0.2, and none of these were significant.

Table 1: Comparison of differences in measured loss in stiffness for the different fracture types. The different fracture groups are indicated by their acronyms: DS=Diamond-blade Saw, SC=Steel Cable, CI=Compressive Impact and BI=Bending Impact.

p-values	**Type of induced Fracture**					
Type of Analysis	DS - SC	DS - CI	DS - BI	SC - CI	SC - BI	CI - BI
Experimental	0.000	0.000	0.000	0.698	0.104	0.479

Table 2: Comparison of differences in the measured loss in stiffness and the FE-calculated loss in stiffness. The different fracture groups are indicated by their acronyms: DS=Diamond-blade Saw, SC=Steel Cable, CI=Compressive Impact and BI=Bending Impact.

p-values	**FE-resolution (micron)**			
Fracture Groups	80	60	40	20
DS	1.000	0.197	0.678	1.000
SC	0.000	0.000	0.000	0.000
CI	0.000	0.000	0.000	0.000
BI	0.030	0.053	0.170	0.353

Table 3: Correlation coefficients R between the morphology parameters and the experimental measured loss in stiffness for all resolutions. The different fracture groups are indicated by their acronyms: DS=Diamond-blade Saw, SC=Steel Cable, CI=Compressive Impact and BI=Bending Impact.

R	n	BV/TV	Tb.N	Tb.Th	Tb.Sp	SMI	Fx.Th
DS	20	0.218	0.350	0.051	-0.276	-0.160	-0.834
SC	20	-0.050	-0.006	-0.212	-0.007	-0.004	0.402
CI	10	0.107	0.482	-0.296	-0.431	0.311	0.223
BI	10	0.130	-0.426	0.730*	0.335	-0.266	0.362
Pooled Data set	60	0.138	0.183	-0.004	-0.176	-0.147	0.146

* Correlation is significant at the 0.05 level (2-tailed).

DISCUSSION

The goals of this study were: first, to measure the loss in stiffness under compressive loading for different types of induced fractures and to compare these measurements with predictions based on micro-FE analyses, and second, to investigate whether the loss in stiffness is related to the bone microstructural morphology or the fracture morphology. The results of this study demonstrated that micro-FE analyses indeed would overestimate the stiffness of fractured bone in cases where the fractured bone ends were irregular (fractures made by the cable and through the impact forces), although significant differences were found only for the SC and the CI groups. Only in the case of a smooth cut (samples cut by the diamond blade saw) the estimation of stiffness was good. This indicates that micro-FE analysis likely does not provide reasonable results in case of bone fractures due to trauma or osteoporosis, but it could provide reasonable assessment of bone stiffness after orthopaedic interventions such as osteotomies. It should be noted, however, that the cut generated by orthopaedic oscillating saws is expected to be less smooth than the one generated by the diamond blade saw used here.

It should be noted that the stiffness values calculated for the damaged specimens were not corrected for the change in length of the specimen after the fracture was created. On average, the length of the specimens in the DS and CI group after fracture was reduced by 0.5 mm and 1.0 mm respectively, while that of the specimens in the SC and BI group was slightly increased by 0.1

mm and 0.3 mm respectively, due to the rough fracture surface. Correcting for such changes in length would change the calculated stiffness values by 1% (SC group) to 10% (CI group). However, since such corrections would be the same for the experimental and micro-FE results, it would not affect the results for the calculated change in stiffness.

We assumed there would be two major reasons why micro-FE analysis would overpredict the stiffness of fractured bone. First, in the fractured region trabeculae from both fracture sides might touch or interlock whereas in the HR-pQCT images, such touching and interlocking trabeculae appear to be connected to each other. And second, during the fracture, large deformations occur in trabeculae leading to damage accumulation and consequent reduction of their material properties. The design of our experiments enabled us to differentiate between these effects. When using the diamond-blade saw, no damage to the tissue itself was expected, which was visually confirmed from the micro-CT scans and the image registration analysis. Thus, the reduction of stiffness was assumed to be due to the loss of connectivity at the interface (related to the mismatch of trabecular ends at the fracture interface), in that cut trabeculae cannot transfer any tensile loads or bending moments, and that cut trabeculae no longer are supported at both ends, such that they will bend and buckle much easier. This combined effect is similar to what has been reported as the ‘end artifact’ in experimental studies that use bone samples for compression tests (Keaveny *et al.*, 1994 and 2009; Linde, 1994). Based on the experiment, we conclude that these effects will reduce the stiffness by approximately 40%. This is somewhat less than what has been reported for the ‘end artifact’ in compression tests earlier, but in these earlier tests the cut surfaces were in contact with the steel plates of the test machine whereas in our setup they are in contact with each other, which likely still provides some support against sliding. The fact that the micro-FE results were in good agreement with the experiments in the diamond saw case, indicates that the major reason for the loss in stiffness is probably the reduced connectivity at the interface, since this was the only known effect that could have lead to reduced stiffness after fracture that both the experiment and the micro-FE analyses could have accounted for.

For the other groups the loss of stiffness was around 80%, indicating that the loss of stiffness due to damage of bone material is of a similar magnitude as that due to the loss of connectivity. The somewhat lower loss in stiffness for the bending impacted specimens when compared to the cable-cut specimens could relate to the fact the impact loading creates a more brittle fracture, due to its high speed. The rather low value for the Fx.Th also points in this direction.

The low correlations between morphological parameters and the loss of stiffness indicate that it is not possible to improve the prediction of the loss of stiffness by measuring bone morphology. A possible explanation for this finding could be that the morphological parameters, which are averaged over the whole specimen, do not provide information about the very local processes that lead to the initiation and progression of the fracture that in the end determine the morphology of the fracture region. It is possible that other parameters or parameters that are measured in the fracture region only would provide a better estimate for the loss in stiffness. The experiments as performed in our study, however, are not suitable for exploring this further since in 3 of the 4 groups the location of the fracture is prescribed by the experiment.

A few limitations of this study should be mentioned. First, we only included trabecular bone. It seems reasonable to expect that the overestimation of stiffness is higher for trabecular than for cortical bone specimens, such that the results presented here may be considered a worst case scenario. In distal radius fractures, the cortical bone will be carrying load as well. However, in particular in elderly, the cortical bone at the most distal regions is usually rather thin and it is expected that most of the load is carried by the trabecular core.

Second, the technique used here to determine the fracture thickness cannot be used in the same way for bone in-vivo since in that case no pre-fracture image is available to register the scan to. In the present study, however, it was included merely to investigate its potential predictive value, and the present results do not warrant further investigation of this measure for the prediction of the stiffness loss.

Third, when translating our results to patient studies, our results are only valid directly after the fracture occurred. During fracture healing, new bone tissue will form and gradually the fracture will be closed. It is possible to model this process using micro-FE modelling with element moduli that are dependent on the local mineralisation (Shefelbine *et al*., 2005; de Jong *et al*., 2014). Once a connection is established, it will also be possible to investigate other loading modes than compression as used here, such as bending and torsion (de Jong *et al*. 2014). Validating results for different stages of healing, however, will require animal experiments, and is beyond the scope of the present study.

In conclusion, the results of this study demonstrated that micro-FE analysis severely overestimated the stiffness of fractured cancellous bone and that this much depended on the type of the fracture. Only in the case of very smooth fractures or osteotomies, the micro-FE results provided reasonable estimations of the stiffness.

Conflict of interest

Bert van Rietbergen is a consultant for Scanco Medical AG.

Acknowledgments

This study was supported by the grants program “Programa de Formación Doctoral Francisco José de Caldas Generación del Bicentenario” awarded by the Francisco José de Caldas Institute for the Development of Science and Technology (COLCIENCIAS, Colombia). LASPAU ID 20110290.

REFERENCES

Cyganik L., Binkowski M., Kokot G., Rusin T., Popik P., Bolechala F., Nowak R., Wróbel Z., John A., 2014. Prediction of Young's modulus of trabeculae in microscale using macro-scale's relationships between bone density and mechanical properties. *Journal of the mechanical behavior of biomedical materials* 36, 120-134.

de Jong J.J.A., Willems P.C., Arts J.J., Bours S.G.P., Brink P.R.G., van Geel T.A.C.M., Poeze M., Geusens P.P., van Rietbergen B., van der Bergh J.P.W., 2014. Assessment of the healing process in distal radius fractures by high resolution peripheral quantitative computed tomography. *Bone* 64, 65-74.

Ellouz R., Chapurlat R., van Rietbergen B., Christen P., Pialat J., Boutroy S., 2014. Challenges in longitudinal measurements with HR-pQCT: Evaluation of a 3D registration method to improve bone microarchitecture and strength measurement reproducibility. *Bone* 63, 147-157.

Hambli R., 2013. Micro-CT finite element model and experimental validation of trabecular bone damage and fracture. *Bone* 56, 363-374.

Hollister S., Brennan J., Kikuchi N., 1994. A homogenization sampling procedure for calculating trabecular bone effective stiffness and tissue level stress. *Journal of biomechanics* 27, 433-444.

Hsu J., Wang S., Huang H., Chen Y., Wu J., Tsai M., 2013. The assessment of trabecular bone parameters and cortical bone strength: a comparison of micro-CT and dental cone-beam CT. *Journal of Biomechanics* 46, 2611-2618.

Jayakar R.Y., Cabal A., Szumiloski J., Sardesai S., Phillips E.A., Laib A., Scott B.B., Pickarski M., Duong L.T., Winkelmann C.T., McCracken P.J., Hargreaves R., Hangartner T.N., Williams D.S., 2012. Evaluation of High-resolution peripheral quantitative computed tomography, finite element analysis and biomechanical testing in a pre-clinical model of osteoporosis: A study with odanacatib treatment in the ovariectomized adult rhesus monkey. *Bone* 50, 1379-1388.

Keaveny T.M., Guo X.E. et al., Wachtel E.F., 1994. Trabecular bone exhibits fully linear elastic behavior and yields at low strains. *Journal of Biomechanics* 27, 1127-1136.

Keaveny T.M., Bevill G., 2009. Trabecular bone strength predictions using finite element analysis of micro-scale images at limited spatial resolution. *Bone* 44, 579-584.

Kumasaka S., Asa K., Kawamata R., Okada T., Miyake M., Kashima I., 2005. Relationship between bone mineral density and bone stiffness in bone fracture. *Oral Radiology* 21, 38-40.

Linde F., 1994. Elastic and viscoelastic properties of trabecular bone by a compression testing approach. *Danish Medical Bulletin* 41, 119-138.

MacNeil J.A., Boyd S.K., 2008. Bone strength at the distal radius can be estimated from high-resolution peripheral quantitative computed tomography and the finite element method. *Bone* 42, 1203-1213.

Meyer U., de Jong J., Bours S., Keszei A., Arts J., Brink P., Menheere P., van Geel T., van Rietbergen B., van den Bergh J., Geusens P., Willems P., 2014. Early changes in bone density, microarchitecture, bone resorption, and inflammation predict the clinical outcome 12 weeks after conservatively treated distal radius fractures: an exploratory study. *Journal of Bone and Mineral Research* 29, 2065-2073.

Mueller T.L., Christen D., Sandercott S., Boyd S.K., van Rietbergen B., Eckstein F., Lochmuller E., Muller R., van Lenthe G.H., 2011. Computational finite element bone mechanics accurately predicts mechanical competence in the human radius of an elderly population. *Bone* 48, 1232-1238.

Muller R., van Lenthe G.H., 2006. Trabecular bone failure at the microstructural level. *Current Osteoporosis Reports* 4, 80-86.

Piscitelli P., Brandi M.L., Tarantino U., 2010. The incidence of fragility fractures in Italy. *Bone* 48:S199.

Rosner B., 2011. Fundamentals of Biostatistics. Seventh edition, Brooks/Cole, Canada, pp. 450.

Shelfebine S., Ulrich S., Claes L., Gold A., Gabet Y., Bab I., Muller R., Augat P., 2005. Prediction of fracture callus mechanical properties using micro-CT images and voxel-based finite element analysis. *Bone* 36, 480-488.

Stauber M., Rapillard L., van Lenthe G.H., 2006. Importance of individual rods and plates in the assessment of bone quality and their contribution to bone stiffness. *Journal of Bone and Mineral Research* 21, 586-595.

Tarantino U., Capone A., Planta M., D'Arienzo M, Leticia Mauro G., Impagliazzo A., 2010. The incidence of hip, forearm humeral, ankle, and vertebral fragility fractures in Italy: results from a 3-year multicenter study. *Arthritis Research & Therapy* 12, R226.

Tassani S., Matsopoulos G., 2014. The micro-structure of bone trabecular fracture: an inter-site study. *Bone* 60, 78-86.

Ural A., Bruno P., Zhou B., Shi X T., Guo X.E., 2013. A new fracture assessment approach coupling HR-pQCT imaging and fracture mechanics-based finite element modeling. *Journal of Biomechanics* 46, 1305-1311.

van Rietbergen B., Weinans H., Huiskes R., Odgaard A., 1995. A new method to determine trabecular bone elastic properties and loading using micromechanical finite-element-models. *Journal of Biomechanics* 28, 69-81.

Varga P., Baumbach S., Pahr D., Zysset P.K., 2009. Validation of an anatomy specific finite element model of Colles' fracture. *Journal of Biomechanics* 42, 1726-1731.

Varga P., Zysset P.K., 2009. Assessment of volume fraction and fabric in the distal radius using HR-pQCT. *Bone* 45, 909-917.

Varga P., Baumbach S., Pahr D., Zysset P.K., 2010. HR-pQCT based FE analysis of the most distal radius section provides an improved prediction of Colles' fracture load in vitro. *Bone* 47, 982-988.

Verhulp E., van Rietbergen B., Muller R., Huiskes R., 2008. Indirect determination of trabecular bone effective tissue failure properties using micro-finite element simulations. *Journal of Biomechanics* 41, 1479-1485.

Vilayphiou N., Boutroy S., Sornay-rendu E., van Rietbergen B., Munoz F., Delmas P.D., Chapurlat R., 2010. Finite element analysis performed on radius and tibia HR-pQCT images and fragility fractures at all sites in postmenopausal women. *Bone* 46, 1030-1037.

Zhou B., Liu X., Wang J. Lu X., Fields A., Guo X., 2014. Dependence of mechanical properties of trabecular bone on plate-rod microstructure determined by individual trabecula segmentation (ITS). *Journal of Biomechanics* 47, 702-708.

Chapter 3

The compressive stiffness of cemented cancellous bone

The content of this chapter is based on:

Arias-Moreno A.J., Ito K., van Rietbergen B., 2019. The compressive stiffness of cemented cancellous bone. In preparation.

ABSTRACT

In case of severe fragility fractures, bone cements are often used to stabilize the fracture. In this study we investigated to what extent calcium-phosphate cements (CPC) can restore the original compressive stiffness of fractured cancellous bone samples, and if this restoration can be evaluated from micro-FE analyses or the cement morphology. A total of 56 porcine trabecular cores were micro-CT scanned and tested in compression before and after fracture (induced in 3 different manners) and after cement stabilization. Based on the micro-CT images, micro-FE models were created to simulate the experimental tests and the cement morphology was quantified. The stiffness measured after cement fixation was 12% to 53% less than the original intact stiffness. The micro-FE analyses underpredicted the stiffness of smooth cemented fractures while it overpredicted that of non-smooth cemented fractures. Only poor correlations were found between the cemented stiffness and cement morphology. It was concluded that CPC´s can only partly restore the compressive stiffness of cancellous bone samples and that neither micro-FE nor the cement morphology can provide an accurate estimate of compressive stiffness directly after cement fixation.

INTRODUCTION

Nowadays, Calcium Phosphate Cements (CPC) are widely recognized as versatile bone graft substitutes for fixation of prostheses and screws (Stadelmann *et al*., 2010; Larsson *et al*., 2012; Kohlhof *et al*., 2013), filling bone defects (Scheer *et al*., 2009; Winge *et al*., 2018), correcting skeletal deformities (van de Watering *et al*., 2012; Hoekstra *et al*., 2013), and restoring the structural integrity of fractures of lower limbs (Beckmann *et al*., 2007; Yao *et al*., 2009; Goff *et al*., 2013), vertebrae (Tarsuslugil *et al*., 2013; Nakano *et al*., 2014; Maestretti *et al*., 2014) and distal radius (Kopylov *et al*., 2002; Sripada *et al*., 2006; Lozano-Calderon *et al*., 2007). Compared to other bone graft substitutes that can only provide mechanical support after new bone has grown into the graft, the advantage of CPC's is that they provide immediate support. In particular when used for the stabilization of fractured bone, this is an advantage as it enables some load bearing before the bone healing process has progressed. For successful healing, however, the micromotions and strains in the damaged region should be reduced to normal physiological values. This implies that the stiffness of the cemented bone should be similar to the pre-fractured state, even directly after the CPC treatment. Over time, the cement then is supposed to gradually resorb while new bone is formed, which in the ideal situation would imply a rather constant stiffness over time until full healing. Presently, however, it is unclear to what extent cement can recover this original stiffness of fractured bone at different time-points of the healing process. In the present study, we focus on the mechanical properties of fractured bone directly after CPC treatment. The goals of this study were to investigate: first, to what extent CPC can restore the original bone stiffness of cancellous specimens subjected to different types of fractures; second, whether the stiffness of cemented bone can be evaluated by micro-FE analyses; and third, if the final stiffness after cementation is related to the cement morphology or the extent of the bone-cement interface. To investigate this, we use small cancellous bone samples for which high-resolution images were obtained before and after a fracture was induced (in 3 different manners) and after cement fixation of the fractured samples. The stiffness of the samples obtained experimentally is then correlated to morphological parameters and to the stiffness calculated from micro-FE.

MATERIALS AND METHODS

The methods used in this study were largely the same as those implemented previously (Chapter 2). In addition to a summarized overview of these methods, the cement analysis that was not part of the previous publication is provided in detail.

Sample preparation, scanning and testing

Fifty-six cylindrical trabecular bone samples (7.5 mm diameter, 10 mm length) were obtained from porcine proximal tibiae using a hollow drill irrigated with PBS. Samples were extracted normal to the tibia plateau, and then cut using a diamond-blade saw to ensure plan-parallel ends, where endcaps were glued. Care was taken that the samples did not contain any part of the physis. Each sample was scanned in a micro-CT system (µCT 80, Scanco Medical AG, Switzerland) at a resolution of 20 µm (Voltage 70 kVp; Intensity 114 µA; Integration time 300 ms) in air in a closed holder. After scanning, the compressive stiffness of each sample was determined in a quasi-static non-destructive compression test (0.1 mm/min) up to 200 N with preconditioning phase using four cyclical loads of 20 N (Universal testing machine BT1-FB010TND30, Zwick/Roell, Germany) (Fig. 1). A multicamera extensometer (VideoXtens, Zwick/Roell, Germany) was used to measure strain directly at the sample's surface. Stiffness was obtained as the slope of the load-displacement curve in the range of 100 – 200 N.

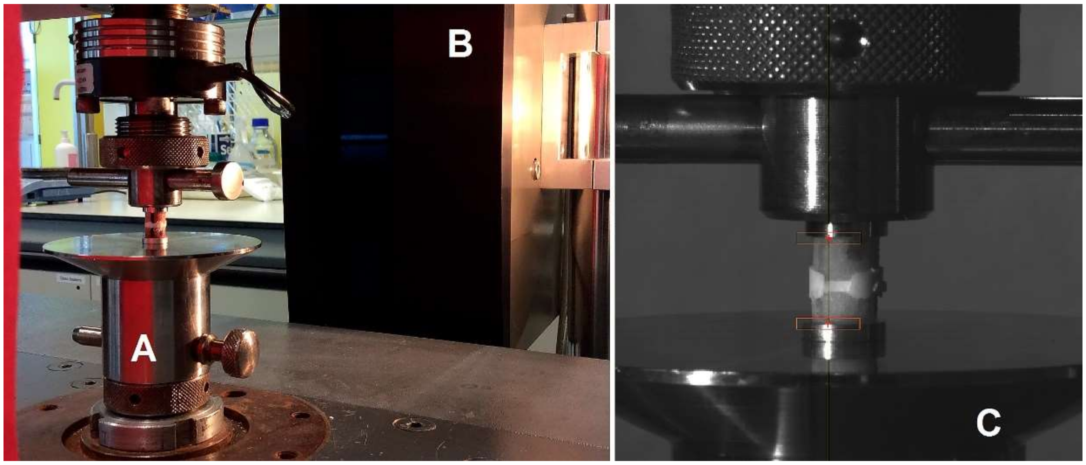

Figure 1. Compression test setup (A) measured by a multicamera extensometer (B). A measurement image obtained from this optical measurement system (C).

Inducing fractures

Using waterproof felt markers, first three lines of different colours were drawn along the length of the sample. Then, three different methods to create the fractures were applied on the 56 samples. With the first method (n=20), samples were cut at their mid-section using a diamond-blade saw (DS group) (Fig. 2a), representing an osteotomy. With the second method (n=18), samples were clamped near their ends and a 0.4 mm diameter steel cable was pulled through the centre of the sample (SC group) (Fig. 2b), creating a shearing stress fracture. With the third method (n=18), a drop-weight impact (0.5 kg weight, 20 cm fall-height) bending setup initiated a comminute fracture (BI group) (Fig. 2c).

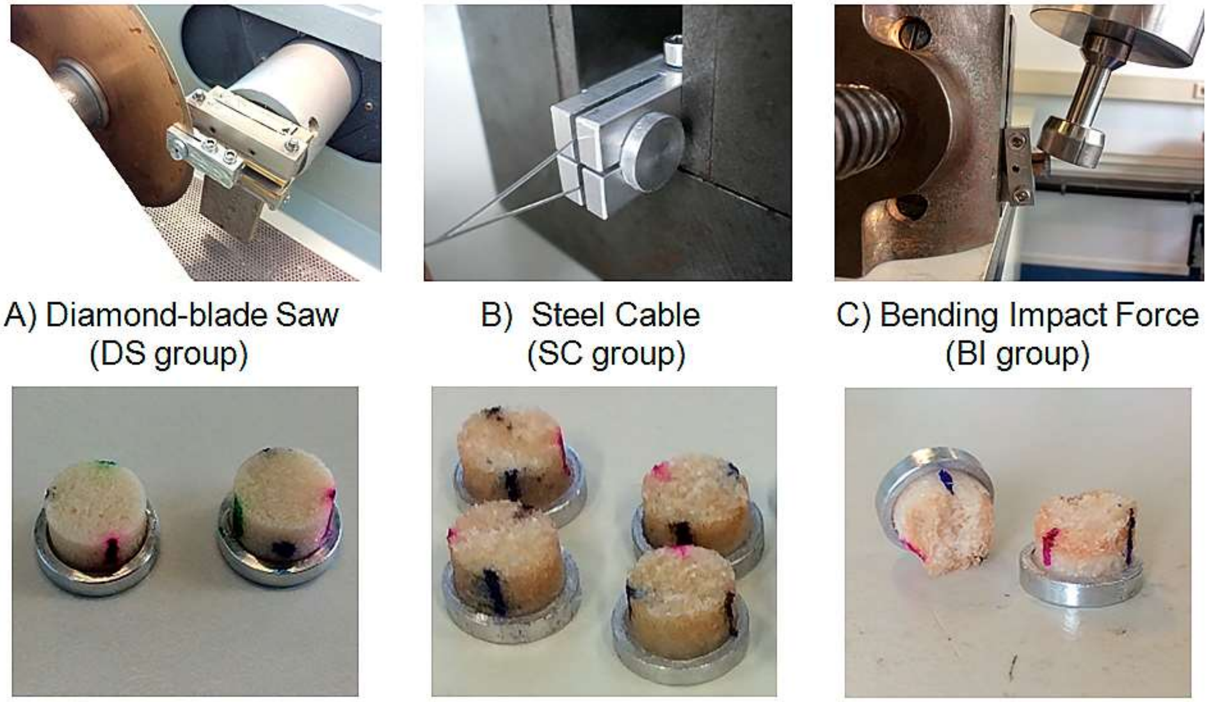
A) Diamond-blade Saw (DS group)

B) Steel Cable (SC group)

C) Bending Impact Force (BI group)

Figure 2. Implemented mechanisms to induce fractures inside the bone samples: a smooth fracture (osteotomy) by diamond-blade saw (A), a shearing fracture by steel cable (B), and a comminute fracture by bending impact force (C).

After fractures were created, the end fragments of the sample were put together in their original position, based on the lines marked before fracturing, and micro-CT scanning and mechanical test measurements were repeated. In particular for the samples that were cut with the saw, it was possible that both ends were slightly rotated relative to each other compared to the intact case. In case the fractures were complete, the main two halves were placed in their original position together with any other smaller fragments.

Cement application

After the second measurements, the fractured ends of each sample were carefully brushed and lavaged with water and then the bottom part of the fractured sample was placed in a customized holder with cylindrical holes that tightly fitted around the sample. As the holder had 10 holes, a total of 10 samples could be placed, all with their fractured end facing upwards. Then, 0.15 ml (150 mm^3) of cement was placed on top of each of the bottom fragments after which the top part of each sample was placed with the fractured end facing down while making sure that the marked lines of each part matched. Then, the top fragments were compressed downwards using a tensile test machine (Universal testing machine BT1-FB010TND30, Zwick/Roell, Germany) at a speed of 5 mm/min until a gap distance of 1 mm remained. During compression, the cement was pressurized into the trabecular bone while some of the cement also leaked to the surface of the samples where it could escape through an outlet to the outside of the holder. The final position was kept for 8 min (indicated by the manufacturer as the cement setting time) after which the samples were carefully taken out of the holder (Fig. 3). After 24h of further cement setting time (Cama, 2014), micro-CT scanning and mechanical test measurements were repeated.

Simultaneously with each cemented sample series, cement was also injected into a cylindrical metallic mold to create 3 cement samples that were later mechanically tested to measure their Young’s moduli. These values were later averaged and used as the cement Young’s modulus in micro-FE analyses.

Figure 3. Cemented samples after removal from the customized cement application holder.

Image processing and bone morphology analysis

Image processing was similar to that performed in an earlier study (Chapter 2). In summary: micro-CT images were filtered using a gauss filtering (sigma = 2, support = 0.8 voxels) and segmented using a global threshold of 220 per mile of the maximum grey value, corresponding to 483 mg HA/ccm.

To check the homogeneity of the samples between groups, the following bone morphology indices were determined: bone volume fraction (*BV/TV*), Trabecular number (*Tb.N*), Trabecular Thickness (*Tb.Th*), Trabecular Separation (*Tb.Sp*).

Cement segmentation and morphology measures

To segment the cement from the images, an image registration technique similar to one that was described earlier was applied (Tassani *et al*., 2014; Chapter 2). With this technique, the 3D image of each fractured end of a sample was registered to the 3D image of the cemented-sample using 3D rigid image registration (Ellouz *et al*., 2014). After registration, only the bone voxels that were present in both images were considered bone while the other non-zero voxels were considered the cement. From the resulting segmented model of this cement interdigitated-structure, the following morphology indices were measured: Cement volume (*CV*), Penetration depth (*PD*) (only measured for DS and SC groups as the total height of the volume occupied by the cement minus the mean distance between the fractured opposite ends of the bone after cement application divided by 2), and Cement surface (*CS*). Additionally, with the measured bone surfaces (*BS*), the Bone-Cement interface surface (*BCIS*) was quantified as:

$$BCIS = BS_{top} + BS_{bot} + CS - BS_{cemented} \tag{1}$$

where the subscripts *top/bottom* refers to both ends of the fractured samples, and $BS_{cemented}$ is the total surface measured in the entire cemented sample (Fig. 4).

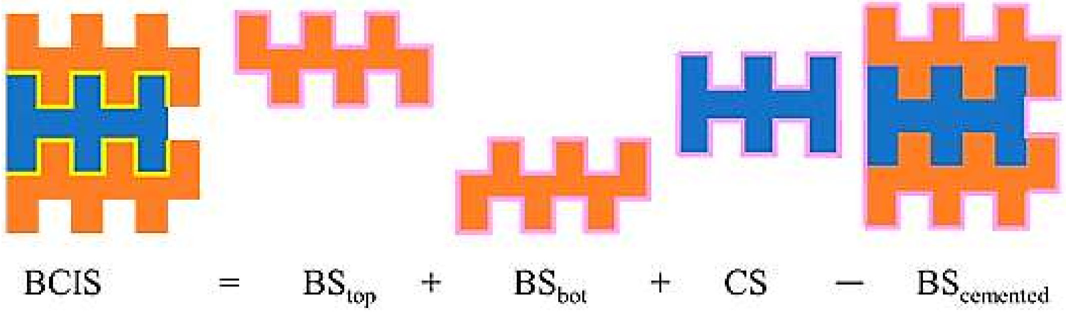

Figure 4. Schematic representation of the calculation of the bone-cement interface surface (*BCIS*). Brown blocks indicates bone tissue, blue cement, yellow lines the *BCIS* and pink lines the bone surface (*BS*) or cement surface (*CS*).

Finally, the change in specimen length compared to intact Δl of the samples after cement application was measured for each fracture group.

Micro-FE

Micro-FE models of the intact specimen and of the specimen after cement application were generated using a voxel conversion procedure (van Rietbergen *et al.*, 1995). For the intact samples, a compression test was first simulated using a tissue Young's modulus of E = 1 GPa to calculate the stiffness of each intact specimen. The tissue Young's modulus of each specimen then was scaled such that the micro-FE calculated stiffness would match the experimentally measured stiffness.

For the models with cement, the same specimen-specific Young's modulus was used for the voxels labelled as bone tissue, while for the voxels that were labelled as cement a Young's modulus based on the compression test performed for the cement samples was assigned. The Poisson's ratio was set to 0.3 for both cement and bone tissue. All image processing and micro-FE analyses were performed using IPLFE v5.16/v1.19 (Scanco Medical AG, Switzerland).

Analysis of results

The change in compressive stiffness measured in the experiment after the fracture and cement application as compared to the intact case was quantified as:

$$\Delta K[\%] = \frac{K^{cut/cem} - K^{intact}}{K^{intact}} * 100 \tag{2}$$

where K^{intact} is the stiffness for the intact specimen and $K^{cut/cem}$ is the stiffness either after fracture or cement application. For the micro-FE analyses, changes are reported only for the cemented case as the prediction of the fractured stiffness was already reported in the previous publication (Chapter 2).

Statistical analysis

To investigate differences in the mean values of bone and cement morphology parameters for the three different groups (DS, SC and BI) of intact specimens, a one-way ANOVA with Tukey post-hoc tests was conducted. Normal distribution and homogeneity of variances were assessed by Shapiro-Wilk's and Levene's tests, respectively.

To investigate differences in the mean values of the experimentally measured stiffness of the three groups (DS, SC and BI) at each of the three different conditions (intact, fractured and cemented), a two-way mixed ANOVA test was conducted with the group as the between subject variable and the condition as the within subject variable. Both Normal distribution and homogeneity of variances were assessed by Shapiro-Wilk's and Levene's tests, respectively.

Finally, to investigate to what extent the experimentally measured stiffness values after cement application correlated with the microstructure morphologies measured at bone and cement, correlation coefficients between these two datasets were calculated for the different groups.

RESULTS

Samples

The micro-CT morphology analysis of the intact samples revealed no significant differences in bone morphology parameters between the three groups, except for Tb.N which was slightly lower in the BI group than in the DS group (Table 1).

Table 1: Mean values of bone morphology parameters measured at the intact bone specimen. The different fracture groups are indicated by their acronyms: DS=Diamond-blade Saw, SC=Steel Cable and BI=Bending Impact.

Morphology parameter	**Type of induced Fracture**		
	DS	SC	BI
BV/TV [1]	.227	.254	.239
Tb.N [1/mm]	2.96	2.76	2.60*
Tb.Th [mm]	.104	.111	.113
Tb.Sp [mm]	.316	.331	.348

BV/TV: Bone volume density; *Tb.N*: Trabecular number; *Tb.Th*: Trabecular thickness; *Tb.Sp*: Trabecular separation.

* Significantly different from DS group ($p<0.05$).

Fracture and cement morphology

The micro-CT images of the cemented samples revealed differences in fracture and cement morphology between the fracture groups (Figs. 5 and 6). As expected, the Diamond-blade saw produced a smooth fracture, while the cement penetrated well into the neighbouring bone (Figs. 5 and 6, left). For the steel cable fracture, a more irregular fracture region was found, with similar penetration of cement to the neighbouring bone (Figs. 5 and 6, center). For the bending impact fracture a very irregular fracture region was found, with also more cement penetration in the neighbouring bone due to the additional porosity created by the fracture (Figs. 5 and 6, right) (Table 2).

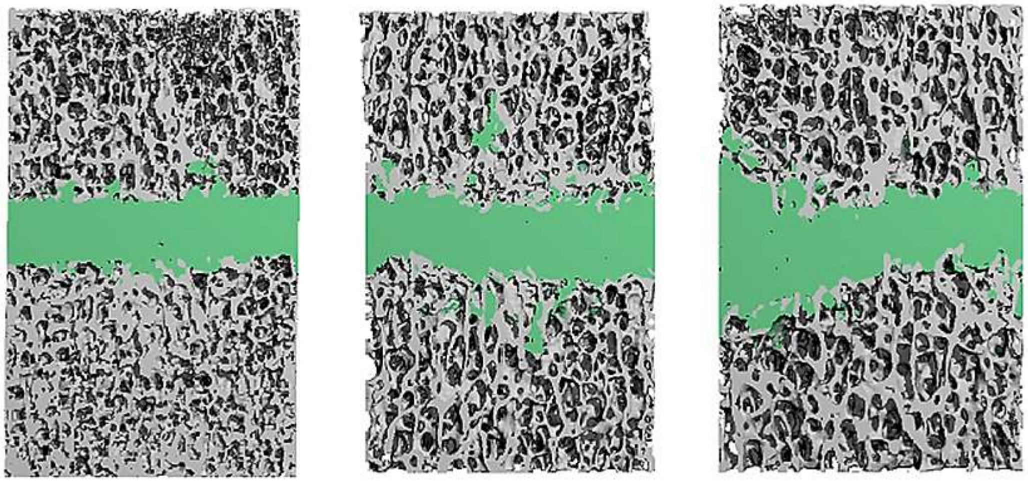

Diamond Saw (DS)
(Osteotomy)

Steel Cable (SC)
(Shearing fracture)

Bending Impact (BI)
(Comminuted)

Figure 5. Micro-CT image-based models of the cemented samples.

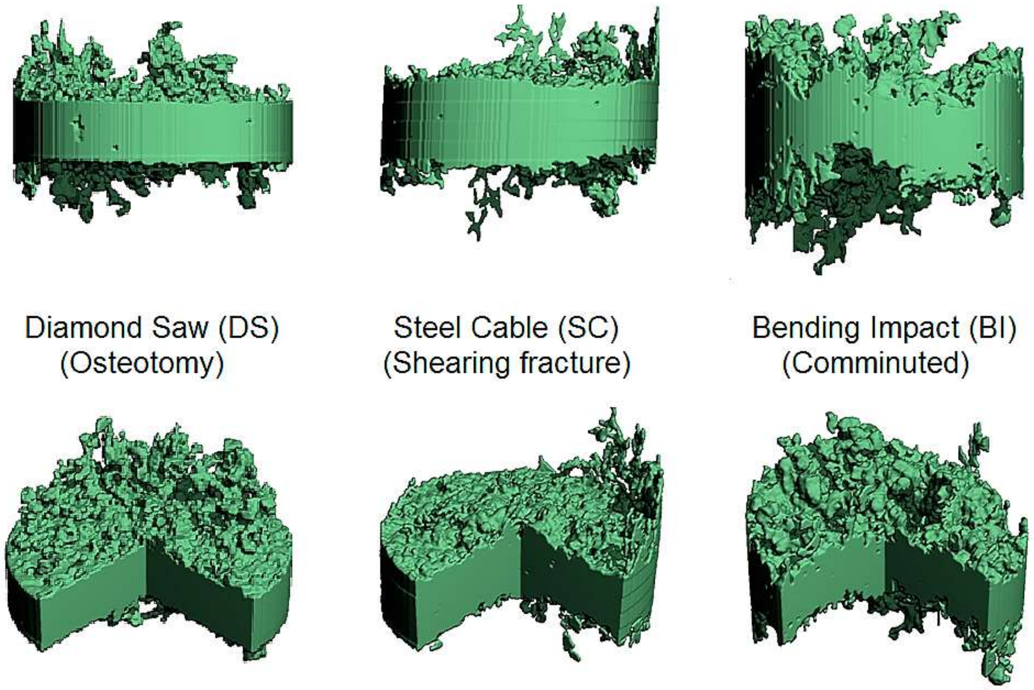

Figure 6. Examples of segmented models of cement structures. Front (top) and sectioned in perspective (bottom) views.

For the cement morphology parameters, significant differences between the fracture groups were found for CV and BCIS (Table 2). The smooth fracture (DS group) was the fracture with highest cement volume. The cement penetration depth was similar for the DS and SC fracture groups. The cement of the most irregular fracture (BI group) had the highest cement surface (CS) and bone-cement interface surface (BCIS) reflecting the complexity of the fracture.

Table 2 Mean values of cement morphology parameters for the different fracture types. The different fracture groups are indicated by their acronyms: DS=Diamond-blade Saw, SC=Steel Cable and BI=Bending Impact.

Morphology parameter	**Type of induced Fracture**		
	DS	SC	BI
CV [mm^3]	81	61*	71*
PD [mm]	1.78	1.70	—
CS [mm^2]	209	207	285
BCIS [mm^2]	220	291*	374*
Δl [mm]	0.76	0.17	0.11

CV: Cement volume; *PD*: Cement penetration depth; *CS*: Cement surface; *BCIS*: Bone-Cement interface surface, Δl: average change in specimen length compared to intact.

(–): *PD* was not measured in the BI fracture group.

* Significantly different from DS group ($p<0.05$).

Stiffness after fracture and cement application

The stiffness measured for the DS group in the intact case was significantly different from the other fracture groups (Table 3). The change in stiffness due to the fracture compared to the intact case was -48±22% for the DS group, -74±18% for the SC group and -75±17% for the BI group (data presented as mean±SD) (Fig. 7), and these results are in good agreement with those obtained in our earlier study (Chapter 2). As expected, the application of the cement increased the stiffness of the fractured samples, but the stiffness was still lower than in the intact case. Compared to the intact case, a change of -12±48% was found for the DS group, of -38±39% for the SC group and of -53±33% for the BI group. In these cemented cases, very large standard deviations were found for the measurements.

For the stiffness values measured after fracture and after cement application, the two-way Anova analyses revealed significant differences between the DS group and any of the other groups, but the results of the SC and BI group were not significantly different (Table 3).

Table 3: Mean stiffness values and mean differences measured in the experiments and from the micro-FE. The different fracture groups are indicated by their acronyms: DS=Diamond-blade Saw, SC=Steel Cable and BI=Bending Impact.

Condition Fracture group		Intact	Fractured	Cemented	Micro-FE Cemented	Difference / Significance (p-value)			
						Fra vs Int	Cem vs Int	Cem vs Fra	mFE Cem vs Int
DS		5281	2532	4058	3306	**-48%** **<.0005***	-12% .310	**73%** **.001***	**-35%** **<.0005***
SC		3348	733	1692	2846	**-74%** **<.0005***	**-38%** **.003***	**205%** **<.0005***	**-13%** **.002***
BI		3189	707	1258	2327	**-75%** **<.0005***	**-53%** **.001***	**162%** **.019***	**-23%** **.017***
Difference / Significance (p-value)	DS vs SC	**58%** **.008***	**245%** **<.0005***	**140%** **<.0005***	16% .475				
	DS vs BI	**66%** **.004***	**258%** **<.0005***	**223%** **<.0005***	**42%** **.041***				
	SC vs BI	5% .966	4% .986	34% .101	22% .406				

* Significantly different from DS group (p<0.05).

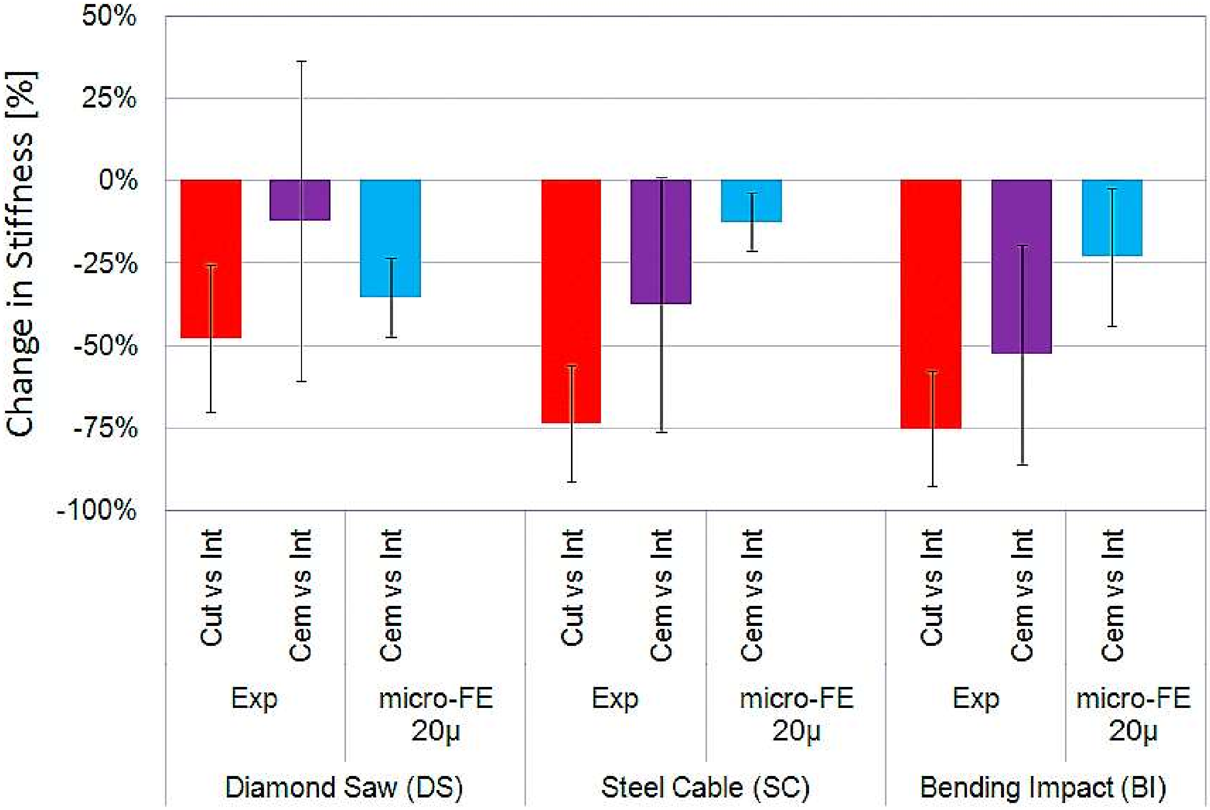

Figure 7. Measured and predicted changes in compressive stiffness after fracture and cement application for the diamond-blade saw (DS), the steel cable (SC), and the bending impact (BI) group. The red and purple bars represent the experimental results (change relative to intact) while the blue bars represent the micro-FE results. Error bars indicate the standard deviation.

Micro-FE analysis

Based on the measured and micro-FE calculated stiffness for the intact specimens, a specimen-specific Young's modulus was determined for each sample. On average, this value was higher for the DS group than for the other groups (Table 4). The Young's modulus of the cement as measured from the additional cement-only samples also varied somewhat between the different batches (Table 4). For the micro-FE models, the Young's modulus measured for the batch from which the cement was obtained was used.

Table 4: Young's modulus of the bone tissue and cement for the different batches

Batch	Young's modulus cement [GPa]	Young's modulus bone tissue [GPa]
DS (n=20)	1.04	12.8±5.4
SC1 (n=10)	1.31	8.0±3.7
SC2 (n=8)	1.12	
BI1 (n=10)	1.21	8.6±3.4
BI2 (n=8)	1.12	

The micro-FE analyses underestimated the stiffness after cement application for the DS group while they overestimated that for the SC and BI groups (Table 3). Compared to intact, the change in stiffness was -35±12% for the DS group, -13±9% for the SC group and -23±21% for the BI group (Fig. 7).

Relationship between cement morphology and final stiffness

Significant correlations between the cement volume (CV) and surface (CS) with stiffness after cement application were found only for the BI group (Table 5).

Table 5: Correlation coefficients R between the morphology parameters measured at the cement and the measured stiffness after cement application. The different fracture groups are indicated by their acronyms: DS=Diamond-blade Saw, SC=Steel Cable and BI=Bending Impact.

R	**CV**	**PD**	**CS**	**BCIS**
group	**[mm^3]**	**[mm]**	**[mm^2]**	**[mm^2]**
DS	-.414	.219	.035	.204
SC	.052	-.313	-.062	.013
BI	.509*	—	.519*	.377

CV: Cement volume; *PD*: Cement penetration depth; *CS*: Cement surface; *BCIS*: Bone-Cement interface surface.

(–): *PD* was not measured in the BI fracture group.

* Correlation is significant at the 0.05 level (2-tailed).

DISCUSSION

The first goal of this study was to investigate to what extent CPC can restore the original compressive stiffness of cancellous specimens subjected to different types of fractures. This study revealed that the cement indeed resulted in an increased compressive stiffness compared to the fractured case, but that the final stiffness was still considerably less than that of intact bone (DS: -12%, SC: -38%, BI: -53%). The results indicate that the cement is less effective in the case of more irregular fractures, such as generated for the SC and BI group. A possible explanation for this could be the larger extent of the damage in these cases compared to the DS group. As a result of this, first, it will be more difficult to stabilize the connection between the two parts by cement, and second, damage might exist as well outside of the cement-penetrated regions that thus are not stabilized by the cement.

A second goal was to investigate if micro-FE analyses can predict the stiffness of the cemented bone. For the smooth fractures (DS group) the cemented stiffness was underpredicted by the micro-FE analyses while for the other groups the stiffness was overpredicted. The overprediction of the cemented stiffness likely relates to two facts. First, the micro-FE-models assume bonding between bone and cement whenever these are in contact whereas in reality the cement does not bind to the bone. Second, the micro-FE-models assume intact bone tissue properties whereas the bone tissue may have been damaged due to the generation of the fracture. Both effects are more severe for the BI group, as this has more bone-cement interface surface and likely will have generated more bone tissue damage also outside the cemented regions. The reason why for the DS group the stiffness is underpredicted is less clear. Obviously, the two effects mentioned above play a lesser role in this group as it has the lowest bone-cement interface surface and as no damage to the neighbouring bone tissue is created by the saw. Possibly, the underprediction is caused by the fact that this group had slightly different characteristics than the other groups. Most notably, the DS group samples were roughly 60% stiffer than the other samples (Table 3), even though their morphology was similar (Table 1). This also resulted in a roughly 50% higher tissue Young's modulus in the micro-FE models compared to the other specimens (Table 4), reflecting a higher state of mineralization of the bone in this batch. Also worth noting is that the cement properties of this group were the lowest of all batches (Table 4), such that the difference between bone tissue and cement properties is larger than in the other groups Furthermore, the change in length of this group after cement application (0.76 mm) was higher than that of the other two groups (<0.17 mm) (Table 2) and the cement volume in this group was higher than that of the other groups. However, presently it is not clear which of these factors would cause the unexpected outcome for this group.

The third goal was to investigate if specific cement morphology parameters or the bone-cement interface were associated with the cemented stiffness. The cemented stiffness of the smooth (DS) and the shearing fractures (SC) group, were not associated with any morphology parameter (Table 5). Only for the roughest fracture (BI group) associations between the cement morphology and the final stiffness were found. However, correlations were only modest (R<0.52), indicating that the final stiffness is not much dependent on cement morphology. Hence, it seems not feasible to predict the stiffness of fractured bone after cement stabilization from high-resolution images by analysing the cement morphology.

A number of limitations of this study should be mention as well. First, as already mentioned before, the bone-cement interface was modelled as bonded by the micro-FE. Earlier studies have modelled the bone-cement interface by including frictional contact (e.g. Janssen *et al.*, 2009). Potentially including such phenomena could improve the predictions for the SC and BI group in our study. Such analyses, however, are much more cpu-time consuming and are not possible with the voxel-conversion meshing approach used here. Second, we only considered a cement thickness of around 1 mm while in clinical practice a thickness of up to 3 mm may be needed to fill bone-defects and for prosthesis fixation (Vaishya *et al.*, 2013). Third, there was some variation in the measured cement moduli between the different batches (coefficient of variation was around 9%). Likely this related to small differences in cement handling, hardening time, etc. To investigate if this could potentially affect our results the micro-FE analyses were repeated for 3 models using either the lowest or highest measured Young's modulus. Differences in the final calculated stiffness were found to be less than 4.8%, suggesting that the any uncertainty in the cement preparation will not much affect the experimental or micro-FE results. Finally, this study focused only on the stiffness of the cemented fractures. It was assumed here that the strength of the bone-cement was sufficient to avoid new fractures. As re-fracturing of a treated site is rare, this seems a reasonable assumption.

The present study focused only on small bone samples in which artificial fractures were made. As shown in earlier studies, however, it is possible to do similar analyses for fractured bone in-vivo (de Jong et al., 2014 and 2016). In such studies High Resolution peripheral Quantitative CT (HR-pQCT) was used to scan the fracture site of patients with a distal radius fracture and micro-FE approaches were used to estimate the stiffness directly after the fracture and during the healing. It was shown that such analyses provide a steady increase in bone stiffness over time due to the healing, where the final stiffness reached after 2 years would actually exceed the stiffness of the contralateral side. Only directly after fracturing, when bone was still disconnected, results were unreliable due to the fact that bone that is actually disconnected may appear connected in the scans. In an earlier study, we investigated this effect further, and found that only for smooth fractures the micro-FE approach may provide reasonable results (Chapter 2). In all of these clinical studies, however, only non-displaced fractures were studied that were stabilized by an external cast. To the best of our knowledge, only one case study exists in which a patient treated with bone substitute was scanned and analysed (Mueller et al., 2011). We expected that micro-FE analyses of bone with cement would suffer less from the artefacts that exists in the non-cemented case directly after fracturing. The results of this study, however, indicate that, also for cemented bone, the mechanical properties are hard to predict and cannot be well predicted from micro-FE analyses. As for the non-cemented case, it is well possible that the analyses will become more accurate once the healing process has started.

In conclusion, we found that CPC´s can only partly restore the compressive stiffness of cancellous bone samples. For non-smooth fractures, the stiffness after cement application is overpredicted by micro-FE analyses and is not or poorly related to the applied cement volume or the cement-bone interface

Conflict of interest

Bert van Rietbergen is a consultant for Scanco Medical AG.

Acknowledgements

This study was supported by the grants program "Programa de Formación Doctoral Francisco José de Caldas Generación del Bicentenario" awarded by the Francisco José de Caldas Institute for the Development of Science and Technology (COLCIENCIAS, Colombia). LASPAU ID 20110290. The authors thank Professor J.J.C. Arts for providing us with the cement used in this study.

REFERENCES

Arias-Moreno A.J., Ito K., van Rietbergen B., 2016. Micro-Finite Element analysis will overestimate the compressive stiffness of fractured cancellous bone. *Journal of Biomechanics* 49, 2613-2618.

Cama G., 2014. Calcium phosphate cements for bone regeneration. In: Dubruel P., van Vlierberghe S. (Eds.), Biomaterials for Bone Regeneration. Woodhead Publishing, Elsevier, Cambridge, UK, pp. 3-25.

Ellouz R., Chapurlat R., van Rietbergen B., Christen P., Pialat J., Boutroy S., 2014. Challenges in longitudinal measurements with HR-pQCT: Evaluation of a 3D registration method to improve bone microarchitecture and strength measurement reproducibility. *Bone* 63, 147-157.

Goff T., Kanakaris N.K., Giannoudis P.V., 2013. Use of bone graft substitutes in the management of tibial plateau fractures. *Injury* 44 S1, S86-S94.

Hoekstra J.W., Klijn R.J., Meijer G.J., van den Beucken J.J., Jansen J.A., 2013a. Maxillary sinus floor augmentation with injectable calcium phosphate cements: a pre-clinical study in sheep. *Clinical Oral Implants Research* 24, 210–216.

Janssen D., Mann K.A., Verdonschot N., 2009. Finite Element Simulation of Cement-Bone Interface Micromechanics: A Comparison to Experimental Results. *Journal of Orthopaedic Research* 27, 1312-1318.

Kohlhof H., Seidel U., Hoppe S., Keel M.J., Benneker L.M., 2013. Cement-augmented anterior screw fixation of Type II odontoid fractures in elderly patients with osteoporosis. *The Spine Journal* 13, 1858-1863.

Kopylov P., Adalberth K., Jonsson K., Aspenberg P., 2002. Norian SRS versus functional treatment in redisplaced distal radial fractures: a randomized study in 20 patients. *Journal of Hand Surgery: British and European Volume* 27(6), 538-541.

Larsson S., Stadelmann V.A., Arnoldi J., Behrens M., Hess B., Procter P., Murphy M., Pioletti D.P., 2012. Injectable calcium phosphate cement for augmentation around cancellous bone screws. In vivo biomechanical studies. *Journal of Biomechanics* 45, 1156–1160.

Lozano-Calderon S., Moore M., Liebman M., Jupiter J.B., 2007. Distal radius osteotomy in the elderly patient using angular stable implants and Norian bone cement. *Journal of Hand Surgery* 32, 976-983.

Maestretti G., Sutter P., Monnard E., Ciarpaglini R., Wahl P., Hoogewoud H., Gautier E., 2014. A prospective study of percutaneous balloon kyphoplasty with calcium phosphate cement in traumatic vertebral fractures: 10-year results. *European Spine Journal* 23, 1354-1360.

Nakano M., Kawaguchi Y., Kimura T., Hirano N., 2014. Transpedicular vertebroplasty after intervertebral cavity formation versus conservative treatment for osteoporotic burst fractures. *Spine* 14, 39-48.

van Rietbergen B., Weinans H., Huiskes R., Odgaard A., 1995. A new method to determine trabecular bone elastic properties and loading using micromechanical finite-element-models. *Journal of Biomechanics* 28, 69-81.

Scheer J.H., Adolfsson L.E., 2009. Tricalcium phosphate bone substitute in corrective osteotomy of the distal radius. *Injury* 40, 262-267.

Sripada S., Rowley D.I., Saito M., Shimada K., Nakashima T., Wigderowitz C.A., 2006. Biomechanical Testing of the Fractured Distal Radius Treated with A New Bone Cement–Is it Strong Enough? *Journal of Hand Surgery* 31, 385-389.

Stadelmann V.A., Bretton E., Terrier A., Procter P., Pioletti D.P., 2010. Calcium phosphate cement augmentation of cancellous bone screws can compensate for the absence of cortical fixation. *Journal of Biomechanics* 43, 2869–2874.

Tarsuslugil S.M., O'Hara R.M., Dunne N.J., Buchanan F.J., Orr J.F., Barton D.C., Wilcox R.K., 2013. Development of calcium phosphate cement for the augmentation of traumatically fractured porcine specimens using vertebroplasty. *Journal of Biomechanics* 46, 711-715.

Tassani S., Matsopoulos G., 2014. The micro-structure of bone trabecular fracture: an inter-site study. *Bone* 60, 78-86.

Vaishya R., Chauhan M., Vaish A., 2013. Bone Cement. *Journal of Clinical Orthopaedics and Trauma* 4, 157-163.

van de Watering F.C., van den Beucken J.J., Walboomers X.F., Jansen J.A., 2012. Calcium phosphate/poly(D,L-lactic-co-glycolic acid) composite bone substitute materials: evaluation of temporal degradation and bone ingrowth in a rat critical-sized cranial defect. *Clinical Oral Implant Research* 23, 151–159.

Winge M.I., Røkkum M., 2018. CaP cement is equivalent to iliac bone graft in filling of large metaphyseal defects: 2 year prospective randomised study on distal radius osteotomies. *Injury* 49, 636-643.

Chapter 4

Accuracy of Beam Theory for Estimating Bone Tissue Modulus and Yield Stress From 3-point Bending Tests on Rat Femora

The content of this chapter is based on:

Arias-Moreno A.J., Ito K., van Rietbergen B., 2019. Accuracy of Beam Theory for Estimating Bone Tissue Modulus and Yield Stress From 3-point Bending Tests on Rat Femora. Submitted.

ABSTRACT

Mechanical analysis of animal long bones often makes use of beam theory to estimate the bone tissue properties from bending tests. In an earlier study, however, van Lenthe et al. (2008) found that using beam theory for the analysis of the tissue Young's modulus of mice femora will lead to a considerable underestimation of the tissue Young's modulus because the measured central cross-section is not representative for the full bone geometry and because roller indentation is not accounted for by beam theory. We hypothesized that beam theory might still be an accurate tool for the determination of bone tissue strength from experimental data, because the highest stresses are found at the central region where the cross-section is measured. The first goal of this study was to test this hypothesis. A second goal of this study was to investigate if the underestimation of the tissue modulus found for mouse femurs is also valid for rat femurs. The final goal was to investigate if micro-FE and beam theory would yield similar increases in Young's moduli and yield stress during aging. Six femurs of 12 weeks old and six femurs of 16 weeks old rats were scanned using micro-CT and subjected to a three-point bending test from which the bending stiffness and the yield force were obtained. The tissue Young's modulus and yield stress then were calculated by regressing the experimental results with results obtained from beam theory as well as results obtained from micro-FE analysis based on the micro-CT scans. It was found that the bone tissue yield strength calculated using beam theory overestimated that calculated from micro-FE by 8.0%. The tissue Young's modulus did not significantly differ. When comparing results for the 12 weeks and 16 weeks groups a similar increase in tissue modulus and yield strength was found for beam theory and micro-FE, but significant differences were found only for the micro-FE tissue yield stress. It is concluded that the use of beam theory to calculate bone tissue yield strength from 3-point bending test results of rat femurs leads to its overprediction.

INTRODUCTION

Mechanical analysis of animal long bones often makes use of beam theory to estimate the stresses within the tissue due to applied bending on these long bones. Such estimates require the calculation of the second moment of area from a CT scan (Ferretti *et al*., 1996; Jamsa *et al*., 1998; Martin *et al*., 2004; Schriefer *et al*., 2005; Rennick *et al*., 2013), which is even possible in the in-vivo case. However, the use of beam theory involves a number of assumptions: the beam is considered long and slender, prismatic, and having constant material properties. Even in the case of testing long bones these premises are only partly met. In an earlier study, van Lenthe *et al*. (2008) investigated the accuracy of calculations based on beam theory when analysing mouse femora. In that study, the results of beam theory (BT) and Finite Element (FE) analyses were regressed to experimental results in order to calculate the bone tissue Young's modulus. They concluded that using beam theory, based on a central cross-section image, will lead to a considerable underestimation of the tissue modulus, with the error depending on both the bending set-up and the bone's size and shape. We expect that this error is mainly due to two reasons. The first is the fact that bones are not prismatic. Beam theory analysis is based on a single central cross-section whereas the total deformation is also affected by the cross-sectional geometry at other locations. The second is the fact that beam theory assumes that the measured deformation is purely due to bending, which it is not. The actual measured displacement is also due to the indentation of the rollers and the deformation of the cross-section. This will lead to an overestimation of the amount of bending when taking the roller displacement as the measure of bending deformation.

Three-point bending tests are also used to calculate the bone tissue strength (Ferreti *et al*., 1996; Jamsa *et al.*, 1998; Stenstrom *et al*., 2000; Schriefer *et al*., 2005; Alippi *et al*., 2011; Hsu *et al*., 2013). In these tests, the highest bending moments will occur at the central section, which is the section typically used to calculate the second moment of area. Moreover, the stress calculation according to beam theory is dependent only on the applied moment *M*, the second moment of area *I*, and the distance from the neutral axis *r* (Beer and Johnston, 2002):

$$\sigma = \frac{M}{I} r \tag{1}$$

The stress thus is independent of inaccuracies in the measurement of the applied displacement and the measured second moment of area should be an accurate representation for that of the highest-loaded cross-section where the fracture will start. We therefore hypothesize that beam theory based on the analysis of a single central cross-section image, although not an accurate predictor of bone tissue elastic properties, will be a good predictor of bone tissue strength. A first goal of this study was to test this hypothesis.

As the present study focuses on rats rather than mice as used by van Lenthe *et al*. (2008), a second aim of this study was to investigate if the predicted underestimation of Youngs's moduli based on results of van Lenthe *et al*. (2008) would also be valid for rat femora. Finally, as the present study included animals of different age for which increases in stiffness and strength are expected due to maturation of the bone, a third aim was to investigate if micro-FE and beam theory would yield similar increases over time in Young's moduli and yield stress.

To reach these goals, we performed 3-point bending tests on rat femora obtained from animals of different age groups and used beam theory to calculate the bone tissue Young's modulus and yield stress. These results then were compared to micro-FE calculations of the bone tissue stresses that were taken as the gold standard.

MATERIALS AND METHODS

Preparation of the femurs

A total of 12 femurs (2 per animal) from male Copenhagen rats, six aged 12 weeks and six aged 16 weeks, were obtained from an earlier study, where half of each age group was treated with an ablation by high intensity focused ultrasound and the other half was kept as control (Yeo *et al*., 2015). All attached soft tissue was removed. Specimens were first CT-scanned and then were kept frozen. Bones were thawed 3 hours before the bending test.

CT scanning

All femurs were CT-scanned using a vivaCT 40 scanner (Scanco Medical AG, Switzerland) with a voxel size of 25 µm (45 kVp, 175 µA, 300 ms integration time). The CT-images then were rotated in such a way that their orientation corresponded to that during the experiments. Thereafter, the images were thresholded based on the density histograms using a single threshold of 675 mgHA/cm^3 value to segment solely the normally mineralized bone tissue (Fig. 1).

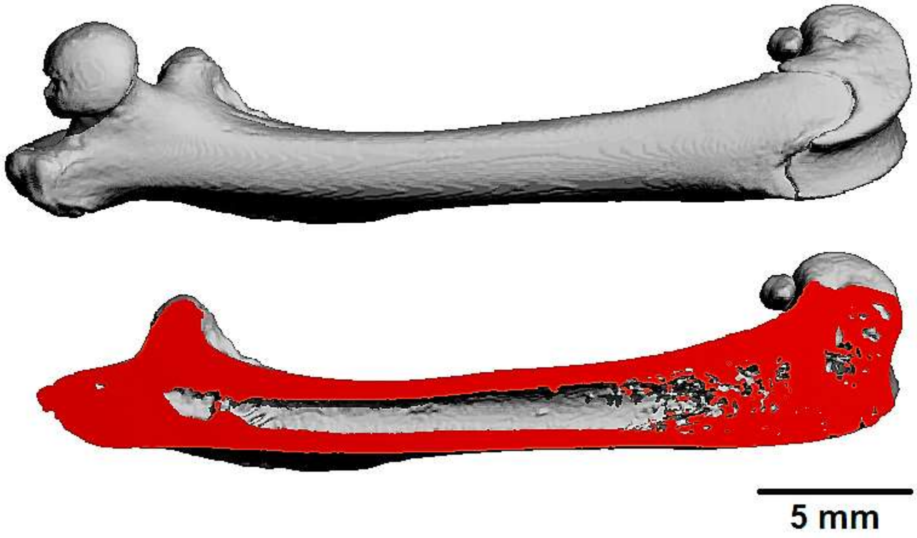

Figure 1. Rat femur segmented model (top) and its longitudinal section (bottom)

Three-point bending tests

Each rat femur was subjected to a three-point bending test to determine both bending stiffness and yield force (Universal testing machine Z010/TN2S, Zwick, Ulm, Germany). The femurs were supported at their metaphysis with a distance L = 23.5 mm between supporting rollers (Fig. 2A). A load was applied on the mid-femoral shaft in the posteroanterior direction at a speed of 0.1 mm/min until tensile failure at the anterior surface of the bone. The experimental bending stiffness S_{exp} was calculated as the slope of the linear elastic range of the obtained force-displacement curve. The yield force $F_{\exp}^{yield}$ was estimated at the point where an 0.2% offset line of the linear range intersected this same curve (Fig. 3).

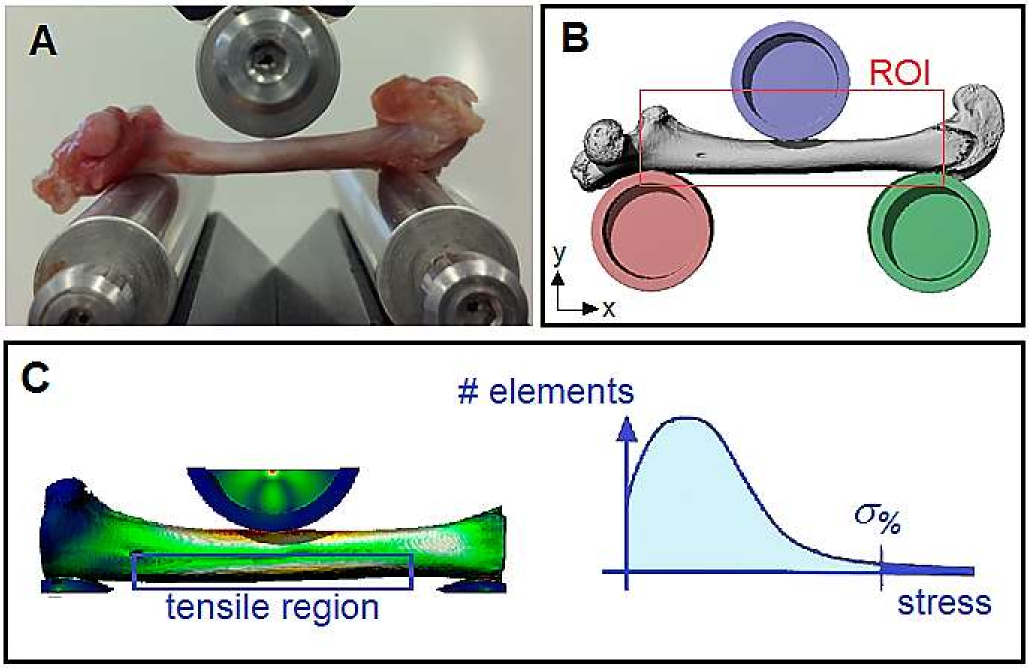

Figure 2. A: 3-point bending test setup. B: segmented micro-FE model representing the same setup. The analyzed region is marked with the red box as the region of interest (ROI). C: Criterion to estimate yield strength. Tissue stresses are evaluated for elements in a 15mm section (blue box) at the tensile region of the shaft.

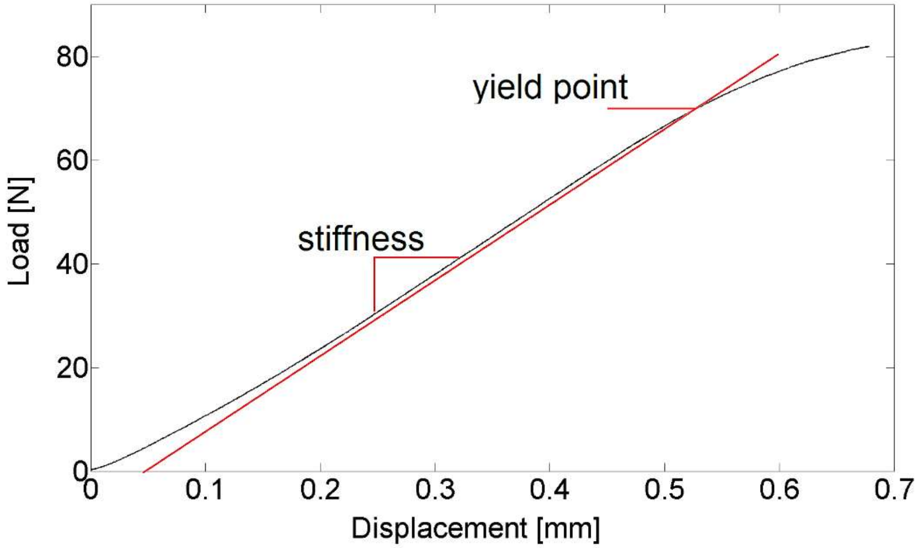

Figure 3. A typical load-displacement curve obtained from a 3-point bending test of a rat femur. The stiffness was calculated as the slope of the linear part of the curve and the yield point was located at the point where an 0.2% offset line of the linear part intersected the curve.

Modelling

For generating the micro-FE models, the image resolution was reduced to 50 µm. Thereafter, bone voxels were converted to micro-FE models using a voxel conversion technique (van Rietbergen *et al.*, 1995). A set of supporting rollers was artificially created and included in the model at the bottom, while on top, a roller was put in contact at the middle-femoral shaft such as in the experimental setup (Fig. 2B). To ensure proper contact, the rollers were penetrating into the bone over a distance of two voxel layers (100 microns). Images then were cropped to include only the region between the bottom rollers plus 0.5 mm on the proximal and distal ends. Also the rollers were cropped, leaving only the part relevant for applying the boundary conditions. Isotropic linear elastic material properties were assigned to all materials with a Young's modulus of 210 GPa for the rollers. For the bone elements, an initial Young's modulus of E_{init} = 10 GPa and a Poisson's ratio of 0.3 were assigned for all elements. The left support roller was constrained in all directions at its central axis, while the right support roller was constrained at its central axis only in the vertical direction. For the top roller a prescribed 1 mm displacement in the vertical direction was applied. The micro-FE calculated bending stiffness S_{FE} then was calculated as the reaction force divided by the applied displacement.

For the beam modelling approach, both the second moment of area *I* of the cross-section and the distance *r* from the neutral axis to the tensile-loaded outer surface of each femur were calculated from the segmented images for 1 slice at the central section where the femur was loaded. All image processing and FE simulations were done using IPLFE v1.16 (Scanco Medical AG, Switzerland).

Tissue Young's modulus calculation

The procedure for calculating the tissue Young's modulus was the same as used in van Lenthe *et al*. (2008) For the micro-FE models: starting with a tissue Young's modulus of E_{init} = 10 GPa the stiffness of the models was calculated. The actual Young's modulus E_{FE} then was determined from the equation:

$$E_{FE} = \frac{S_{\exp}}{S_{FE}} E_{init} \tag{2}$$

with S_{exp} the stiffness measured in the experiment, S_{FE} the stiffness measured from the micro-FE model.

For the beam theory (BT) approach, the Young's modulus was calculated as (Beer and Johnston, 2002):

$$E_{BT} = \frac{S_{exp} L^3}{48I} \tag{3}$$

with *L* the distance between the bottom rollers and *I* the second moment of area.

Yield strength calculation

Using the micro-FE models, the bone tissue stresses were evaluated for elements in a 15 mm section at the central tensile region of the shaft while the bone was loaded with the experimentally measured yield force $F_{\exp}^{yield}$ (Fig. 2C). The maximum principal stress in this region was taken as the bone tissue yield stress $\sigma_{FE}^{yield\_\max}$. As it is known that the micro-FE solution can be inaccurate when evaluating the stresses at single elements (van Rietbergen *et al.*, 1995), also a histogram-based approach was used similar to the strength criterion proposed by Pistoia *et al.*, (2002). With this approach, the principal yield stress $\sigma_{FE}^{yield\_2\%}$ was determined as the corresponding stress value that is exceeded by 2% of all elements in the selected region.

For the beam theory approach, the yield stress was estimated from:

$$\sigma_{BT}^{yield} = \frac{M}{I} r = \frac{F_{exp}^{yield} L}{4I} r \tag{4}$$

with *r* the maximum distance from the neutral axis.

Statistics

For each age group, a paired-samples t-test was conducted to determine whether there were statistically significant differences between the mean tissue Young's modulus calculated from beam theory (E_{BT}) and from micro-FE analyses (E_{FE}). As the tissue yield strength calculation involved comparisons between 3 parameters (σ_{BT}^{yield}, $\sigma_{FE}^{yield\_\max}$ and $\sigma_{FE}^{yield\_2\%}$), for each age group a one-way repeated measures ANOVA with Post hoc analysis with a Bonferroni adjustment were conducted to determine whether there were statistically significant differences between these parameters. Five independent-samples t-tests including Levene's test for equality of variances were run to determine if there were differences in both tissue modulus and yield stress between the age groups for the models. All analyses included both outliers and normality assessments by boxplot and Shapiro-Wilk's test, respectively. All analyses were performed using SPSS Statistics (v23, IBM, USA).

RESULTS

The dimensions and second moment of area measured from the CT scans are listed in Table 1.

Table 1. Structural values as measured at the central CT-slice of each rat femur.

Age [weeks]	n	AP [mm]	WT [mm]	*r* [mm]	Izz [mm^4]
12	6	2.956 ± 0.096	0.513 ± 0.036	1.480 ± 0.131	3.855 ± 0.208
16	6	3.210 ± 0.157	0.645 ± 0.070	1.571 ± 0.092	5.486 ± 0.702

AP: anteroposterior thickness. WT: cortical wall thickness. *r*: distance from the neutral axis to the tensile-loaded outer surface. Izz: second moment of area. Values are presented as mean ± SD.

Three-point bending tests

The average bending stiffness values were 165 and 250 N/mm while the yield forces were 69 and 102 N for the 12w and 16w old specimens, respectively.

Tissue Young's moduli

The Young's moduli calculated from beam theory were not significantly different from those calculated from micro-FE, neither for the 12w group nor for the 16w group (Table 2). Also, no significant differences were found between the 12w group and the 16w group when using beam theory nor when using micro-FE (table 2).

Table 2. Mean Young´s moduli as estimated by beam theory and micro-FE for both age groups (12 and 16 weeks).

Model Age	E_{BT} [GPa]	E_{FE} [GPa]	Difference/ significance E_{BT} vs E_{FE}
12w	11.60	12.25	5.6% p=.400
16w	12.39	13.06	5.4% p=.115
Difference/ Significance 12w vs 16w	6.8% p=.290	6.6% p=.238	

When comparing the measured stiffness with those calculated from the micro-FE analyses and the beam theory, both with the fitted average tissue modulus as in Table 2, the coefficients of determination for the pooled age groups were $R^2 = .848$ and $R^2 = .879$ for the beam theory and micro-FE models respectively (Fig. 4).

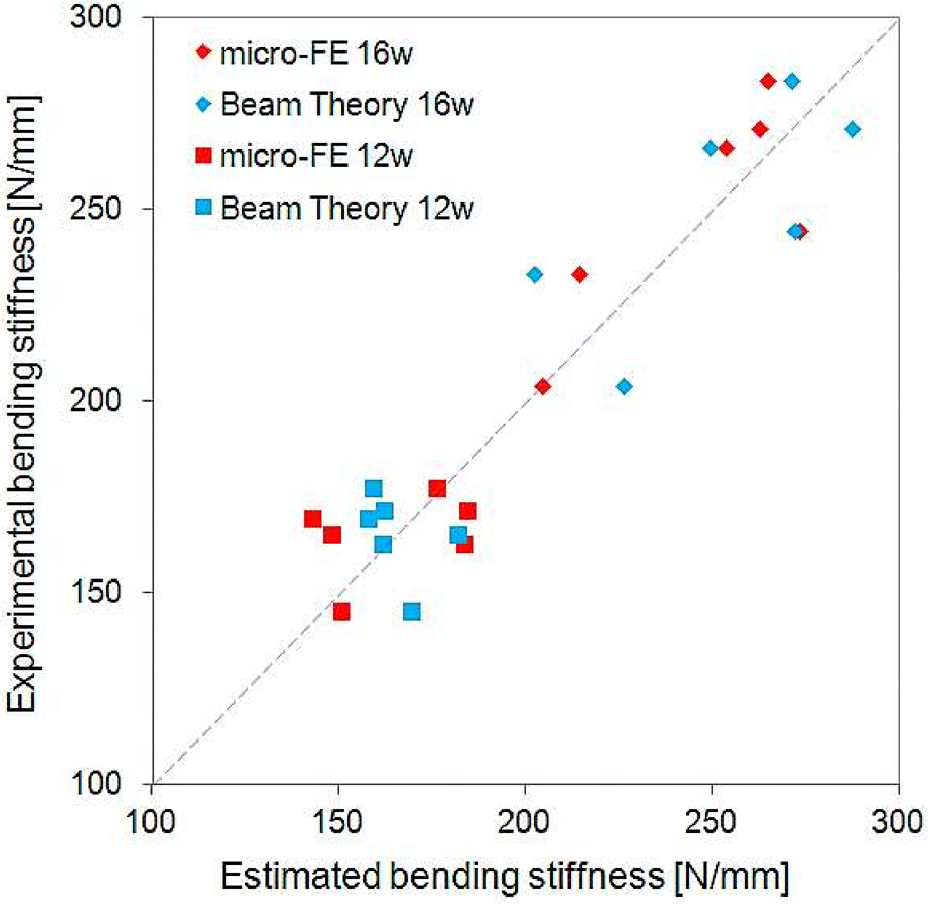

Figure 4. Micro-FE and beam theory bending stiffness estimations by using the fitted E per age groups (12 and 16 weeks).

Tissue yield stress

In general, the yield stresses found from micro-FE analyses and beam theory were significantly different for both age groups, with only one exception in the younger group (σ_{BT}^{yield} vs $\sigma_{FE}^{yield\_\max}$) (Table 3). On average, the yield strength calculated from beam theory was 8% higher than the yield strength calculated from the micro-FE analyses, and even 32% higher than the yield stress calculated from the micro-FE analyses that accounted for a 2% overloaded volume. When comparing the two age groups, only significant changes in tissue yield stress were calculated when using micro-FE.

Table 3. Mean yield stresses as estimated by beam theory and micro-FE for both age groups (12 and 16 weeks).

Model Age	σ_{BT}^{yield} [MPa]	$\sigma_{FE}^{yield\_max}$ [MPa]	$\sigma_{FE}^{yield\_2\%}$ [MPa]	Difference/ significance	
				σ_{BT}^{yield} vs $\sigma_{FE}^{yield\_max}$	σ_{BT}^{yield} vs $\sigma_{FE}^{yield\_2\%}$
12w	154	141	103	**8.4%** **p<.0005**	**33.1%** **p<.0005**
16w	172	159	119	7.6% p=.354	**30.8%** **p<.0005**
Difference/ Significance 12w vs 16w	11.7% p=.074	**12.8%** **p=.036**	**15.5%** **p=.005**		

When regressing the yield forces predicted by beam theory and micro-FE using the mean yield stress as in Table 3 with the experimental values, a coefficient of determination of $R^2 = .822$ was found for the beam theory results and values of $R^2 = .897$ and $R^2 = .922$ were found for the micro-FE results when the yield criterion is based on the maximum principal stress or allows a 2% overloaded volume respectively (Fig.5).

When comparing the measured yield forces with the yield stresses calculated from the micro-FE analyses and the beam theory, the coefficients of determination for the pooled age groups were $R^2 = .515$ for the beam theory, and $R^2 = .715$ and $R^2 = .860$ for the micro-FE models, maximum principal stress and 2% overloaded volume, respectively.

DISCUSSION

Our first goal was to test the hypothesis that beam theory based on the analysis of a single central cross-section will be a good predictor of bone tissue strength. Unlike what we hypothesized, beam theory resulted in a significant overestimation of the tissue yield stress by 8.0% on average over the micro-FE results. This is likely due to the fact that the force applied in the 3-point bending test does not result in bending only (as assumed in beam theory) but also in shear and compressive deformations. As with the stiffness, the severity of this will depend on to what

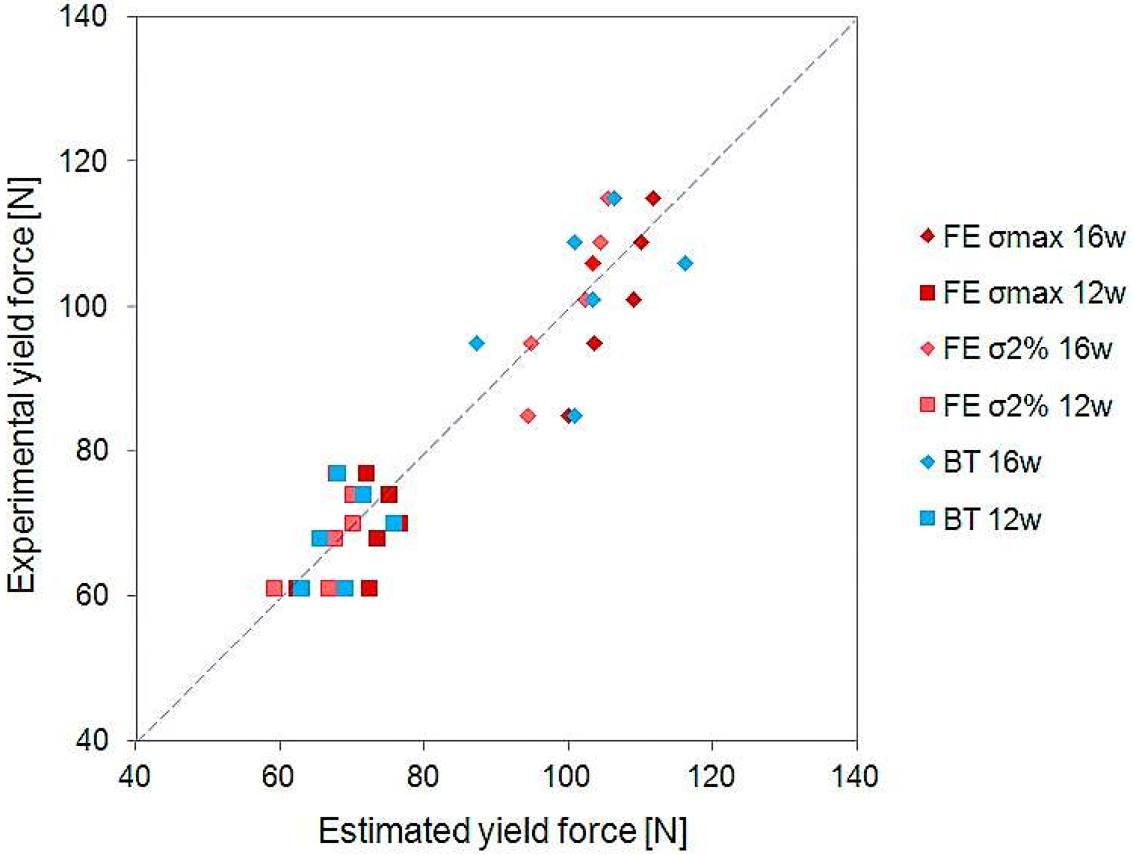

Figure 5. Yield forces estimations per age groups.

extent the beam theory assumptions are met. Although significant differences thus exist between micro-FE and beam theory, this may not pose a major problem as long as the same animals are used in experimental studies. The beam theory estimated yield stresses of this study are higher than values reported in literature, which are roughly in the range of 109 – 151 MPa (Ferreti *et al.*, 1996; Jamsa *et al.*, 1998; Silva *et al.*, 2004; Cory *et al.*, 2010; Hsu *et al.*, 2013), while the micro-FE results using a yield strength equal to the maximum principal stress or the stress overloaded by 2% of the volume are in good agreement to those studies. The micro-FE results using a 2% overloading obviously predict lower values for the tissue strength. Although this model thus had a lower precision, it has a higher correlation with the experimental results than the other micro-FE model, likely due to the fact that the other micro-FE results are more dependent on numerical errors in the FE solution (van Rietbergen *et al.*, 1995).

A second goal was to investigate if the underestimation of tissue Youngs's moduli when using beam theory as reported by van Lenthe *et al*. (2008) for mouse femurs would also be valid for rat femurs. The present study demonstrated that beam theory also tends to underpredict the tissue moduli for rat femora, but no significant differences were found. For the specific setup of our study, with average aspect ratios of 8.0 and 7.5 (calculated as support width divided by anteroposterior thickness) for the 12w and 16w old bones respectively, and a cortical thickness ratio of 0.4 (calculated as cortical wall thickness divided by radius *r*) for all the bones, the expected underestimation would be 16% for the 12w group and 18% for the 16w group based on van Lenthe *et al*. (2008). The reason why no significant differences were found here may be related to differences in size as well as differences in shape and morphology between mouse and rat bones. It is also possible that differences in boundary condition played a role: in this study boundary conditions were applied to the rollers that were penetrated slightly into the bone rather than to the bone directly. Also the large size of the rollers could involve a reduced local indentation at loading points. When regressing the stiffness values predicted by micro-FE and beam theory with the experimental results, higher correlations were found for the micro-FE results, indicating that these better reflect the experimental situation. This is likely due to the fact that the micro-FE analyses include the full bones and can account for the cross-sectional deformation, whereas beam theory results are based only in the central cross-sectional geometry.

A third goal was to investigate if micro-FE and beam theory would yield similar increases in Young's moduli and yield stress due to aging. For the tissue Youngs modulus no significant changes were found. As there were large (significant) differences in the stiffness, this indicates that the increase in stiffness is due to the change in geometry rather than a change in tissue modulus. For the tissue yield stress, the beam theory just did not detect significant differences ($p = .074$) while the micro-FE results using the yield stress just did detect significant differences ($p < .05$). Both models predicted a similar change in tissue Youngs modulus (6.8% for beam theory and 6.6% for micro-FE) and tissue strength due to aging though (11.7% for beam theory, and both 12.8% and 15.5% for micro-FE), suggesting that beam theory will provide reasonable values for changes in strength over time but is less sensitive than micro-FE. The changes found here are also in agreement with literature values that reported increases in tissue strength from 6 to 24.42% per month during growth (Ferguson *et al*., 2003; Silva *et al*. 2013; Zhang *et al*., 2015).

Although the results of this study demonstrate that micro-FE will provide more accurate results than beam theory, some limitations of the micro-FE approach should be discussed as well. The most obvious one is that micro-FE requires scanning the full bone (at least the part that would be relevant for the 3-point bending test). In particular when scanning animals in-vivo, this will increase the scanning time and the radiation dose of the animals. Although earlier studies have indicated no effects of the radiation dose when scanning the metaphysial region in rats (Brouwers *et al*., 2007), the scanning region required here would be larger, and thus involve more radiation than required when scanning only the metaphysial region. In addition, performing micro-FE analyses with simulated rollers as performed in the present study requires additional effort to generate and correctly place the rollers. Finally, the required cpu-time for micro-FE analyses (typically 1 hour) far exceeds that required for calculating only the second moment of area (less than a minute). Because of these limitations, the micro-FE approach might not be suitable when scanning large numbers of animals in-vivo. When analyzing bones after the animals are sacrificed, however, the increased scanning/radiation dose no longer are an issue, and the micro-FE approach is recommended for getting the most accurate results.

Some limitations of the present study should be discussed as well. First, since the rat femurs tested in this study were part of another study carried out to investigate the effect of High-Intensity focused ultrasound (HIFU) on bone tissue properties (Yeo *et al*., 2015), the sample size was limited. As a result, it is possible that some differences would remain undetected. Nevertheless, we did find significant differences between many parameters. Second, half of these femurs received this HIFU treatment that could potentially affect bone tissue stiffness and yield strength, but the study by Yeo *et al*. (2015) confirmed that this was not the case as no significant differences were found between treated and control bones. Third, only linear-elastic micro-FE analyses were performed, and the contact conditions between the bone and rollers were set to a prescribed indentation. As the deformation until reaching the yield point are limited this is considered acceptable.

In conclusion, we found that the use of beam theory to calculate bone tissue strength properties from 3-point bending test results of rat femurs leads to an overprediction of the bone tissue strength values while no significant differences were found for the prediction of the tissue Young's modulus.

Conflict of interest

Bert van Rietbergen is a consultant for Scanco Medical AG

Acknowledgements

This study was supported by the grants program “Programa de Formación Doctoral Francisco José de Caldas Generación del Bicentenario” awarded by the Francisco José de Caldas Institute for the Development of Science and Technology (COLCIENCIAS, Colombia), LASPAU ID 20110290.

REFERENCES

Alippi R., Picasso E., Huygens P., Bozzini C., Bozzini C., 2011. Growth-dependent effects of dietary protein concentration and quality on the biomechanical properties of the diaphyseal rat femur. *Endocrinología y Nutrición* 59, 35-43.

Beer F.P., Johnston E.R., DeWolf J.T., 2002. Mechanics of materials. 3rd ed., McGraw-Hill, New York.

Brouwers J., van Rietbergen B., Huiskes R., 2007. No Effects of In Vivo Micro-CT Radiation on Structural Parameters and Bone Marrow Cells in Proximal Tibia of Wistar Rats Detected after Eight Weekly Scans. *Journal of Orthopaedic Research* 25, 1325-1332.

Cory E., Nazarian A., Entezari V., Vartanians V., Muller R., Snyder B., 2010. Compressive axial mechanical properties of rat bone as functions of bone volume fraction, apparent density and micro-ct based mineral density. *Journal of Biomechanics* 43, 953-960.

Ferguson V.L., Ayers R.A., Bateman T.A., Simske S.J., 2003. Bone development and age-related bone loss in male C57BL/6J mice. *Bone* 33, 387-398.

Ferretti J.L., Capozza R.F., Zanchetta J.R., 1996. Mechanical validation of a tomographic (pQCT) index for noninvasive estimation of rat femur bending strength. *Bone* 18, 97-102.

Hsu J., Wang S., Huang H., Chen Y., Wu J., Tsai M., 2013. The assessment of trabecular bone parameters and cortical bone strength: a comparison of micro-CT and dental cone-beam CT. *Journal of Biomechanics* 46, 2611-2618.

Jämsä T., Jalovaara P., Peng Z., Väänänen H.K., Tuukkanen J., 1998. Comparison of three-point bending test and peripheral quantitative computed tomography analysis in the evaluation of the strength of mouse femur and tibia. *Bone* 23, 155-161.

Martin D.E., Severns A.E., Kabo J.M., 2004. Determination of mechanical stiffness of bone by pQCT measurements: correlation with non-destructive mechanical four-point bending test data. *Journal of Biomechanics* 37, 1289-1293.

Pistoia W., van Rietbergen B., Lochmüller E.-M., Lill C.A., Eckstein F., Rüegsegger P., 2002. Estimation of distal radius failure load with micro-finite element analysis models based on three-dimensional peripheral quantitative computed tomography Images. *Bone* 30, 842-848.

Rennick J., Nazarian A., Entezari V., Kimbaris J., Tseng A., Masoudi A., Nayeb-Hashemi H., Vaziri A., Snyder B., 2013. Finite element analysis and computed tomography based structural rigidity analysis of rat tibia with simulated lytic defects. *Journal of Biomechanics* 46, 2701-2709.

Schriefer J.L., Robling A.G., Warden S.J., Fournier A.J., Mason J.J., Turner C.H., 2005. A comparison of mechanical properties derived from multiple skeletal sites in mice. *Journal of Biomechanics* 38, 467-475.

Silva M.J., Brodt M.D., Fan Z., Rho J., 2004. Nanoindentation and whole-bone bending estimates of material properties in bones from the senescence acceletated mouse SAMP6 . *Journal of Biomechanics* 37, 1639-1646.

Silva M.J. (Ed.), 2013. Skeletal aging and osteoporosis, biomechanics and mechanobiology. 1st ed., Springer-Verlag Berlin Heidelberg, Berlin, Germany.

Stenstrom M., Olander B., Lehto-Axtelius D., Madsen J.E., Nordsletten L., Carlsson G.A., 2000. Bone mineral density and bone structure parameters as predictors of bone strength: an analysis using computerized microtomography and gastrectomy-induced osteopenia in the rat. *Journal of Biomechanics* 33, 289-297.

van Lenthe G.H., Voide R., Boyd S.K., Muller R., 2008. Tissue modulus calculated from beam theory is biased by bone size and geometry: implications for the use of three-point bending tests to determine bone tissue modulus. *Bone* 43, 717-723.

van Rietbergen B., Weinans H., Huiskes R., Odgaard A., 1995. A new method to determine trabecular bone elastic properties and loading using micromechanical finite-element models. *Journal of Biomechanics* 28, 69-81.

Yeo S.Y., Arias Moreno A.J., van Rietbergen B., ter Hoeve N.D., van Diest P.J., Grüll H., 2015. Effects of magnetic resonance-guided high-intensity focused ultrasound ablation on bone mechanical properties and modeling. *Journal of Therapeutic Ultrasound* 3:13.

Zhang R., Gong H., Zhu D., Ma R., Fang J., Yobo F., 2015. Multi-level femoral morphology and mechanical properties of rats of different ages. *Bone* 76, 76-87.

Chapter 5

Validation of distal radius failure load predictions by homogenized- and micro-Finite Element analyses based on second generation high resolution peripheral quantitative CT images

The content of this chapter is based on:

Arias-Moreno A.J., Hosseini H.S., Bevers M., Ito K., Zysset P.K., van Rietbergen B., 2019. Validation of distal radius failure load predictions by homogenized- and micro- Finite Element analyses based on second generation high resolution peripheral quantitative CT images. Osteoporosis International. DOI:10.1007/s00198-019-04935-6.

ABSTRACT

Micro- Finite Element (FE) analyses based on High Resolution peripheral Quantitative CT (HR-pQCT) images are frequently used to predict distal radius failure load. With the introduction of a second generation HR-pQCT device, however, the default modelling approach no longer provides accurate results. The aim of this study was to develop a well standardized and reproducible approach for micro-FE (mFE) and homogenized-FE (hFE) analyses that can provide precise and accurate results for distal radius failure load predictions based on second generation HR-pQCT images. Second-generation HR-pQCT was used to scan the distal 20 mm section of 22 cadaver radii. The sections were excised and mechanically tested afterwards. For these sections mFE and hFE models were made that were used to identify required material parameters by comparing predicted and measured results. Using these parameters, the models were cropped to represent the 10 mm region recommended for clinical studies to test their performance for failure load prediction. After identification of materials parameters, the measured failure load of the 20 mm segments was in good agreement with results of mFE models (R^2=0.969, slope=1.035) and hFE models (R^2=0.966, slope=0.890). When the models were restricted to the clinical region, mFE still accurately predicted the measured failure load (R^2=0.955, slope=1.021), while hFE predictions were precise but tended to overpredict the failure load (R^2=0.952, slope=0.780). It was concluded that it is possible to accurately predict the distal radius failure load using either mFE or hFE models when using the approaches and parameters developed in this study.

INTRODUCTION

Micro- Finite Element (FE) analyses based on High Resolution peripheral Quantitative CT (HR-pQCT) images are nowadays commonly performed in clinical studies to measure bone mechanical properties *in-vivo* (for an overview see (van Rietbergen *et al*., 2015; Samelson *at al*., 2019)). With this approach, an approximately 1 cm region of the distal radius or distal tibia is imaged at 82 microns voxel size and a Laplace-Hamming filtering followed by a thresholding procedure is used to generate a 3D reconstruction of the bone tissue (Laib *et al*., 1999). This reconstruction is then converted to a micro-FE model from which stiffness, failure load and load transfer parameters are calculated for compressive loading conditions (Boutroy *et al*., 2008). In most studies, linear elastic analyses are performed, which cannot simulate the actual failure process during the compression. Instead, an empirical failure criterion is used that assumes that failure will occur if the strain exceeds a critical value (typically set at 0.7%) for a prescribed amount of bone tissue (typically set at 2% of the tissue volume) (Pistoia *et al*., 2002). Several validation studies have been performed to investigate the accuracy and precision of these predictions. In these validation studies, micro-FE based on HR-pQCT images of cadaver bones were used and the predicted results were compared to measured stiffness and failure load values (Pistoia *et al*., 2002; Macneil *et al*., 2008; Varga *et al*., 2010; Mueller *et al*., 2011). These studies have shown excellent correlations between predicted and measured failure load values (with R^2 up to 0.92) and high accuracy (Varga *et al*., 2010).

With the introduction of a second generation HR-pQCT scanner, the image processing has changed. Due to the higher resolution of this scanner reconstructions are made at smaller voxel size (60.7 microns) and a Gauss filtering followed by thresholding is used to generate the segmented image. Thresholds are set at different values for the cortical and trabecular compartment (Manske *et al*., 2017). These changes affect the results of the micro-FE analyses. In an *in-vivo* study comparing micro-FE results based on the first generation HR-pQCT (XCT1) and the second generation HR-pQCT (XCT2) images, good correlations were found (R^2>0.9), but a significant bias existed in the results, with XCT2 underestimating the failure load at the radius when using the common failure criterion (Agarwal *et al*., 2016). This underestimation was due to the fact that the threshold used for the XCT1 images was deliberately set too low, as the segmented image originally was used only for the trabecular number calculation, resulting in an overestimation of the amount of bone when using this same image as the basis for micro-FE analysis. Therefore, in order to get good agreement with experimental results, elastic and strength parameters were tuned to compensate for the overestimation of the amount of bone tissue. As the thresholds used for the XCT2 images are higher, resulting in a better representation of the actual mineralized phase, these values require new tuning in order to predict accurate values. In an earlier study (Hosseini *et al*., 2017), we directly compared the results of micro-FE analyses based on XCT2 images with experimental results and found similar results as reported in other earlier studies with regard to the underestimation of the predicted failure load when using XCT2 versus XCT1 images (Agarwal *et al*., 2016). In our earlier study, however, the tested region was 20 mm, which is not the same as the standard clinically measured region (10.2 mm) and comprises bone more distal and more proximal of the standard scan region. Because the empirical failure criterion is also dependent on the resolution and the size of model (Mueller *et al*., 2011), no tweaking could be performed in a way that would be relevant for the clinical scan region in that earlier study.

Another issue with the introduction of the XCT2 has been the increase in solution times due to the increased size of the micro-FE models. Whereas the XCT1 based models typically take between 4 and 8 hours to solve, the XCT2 based models typically are in the range of 12 to 24 hours. In the earlier validation study mentioned above (Hosseini *et al*., 2017), we also introduced an alternative homogenized FE (hFE) approach that can speed up the calculations and in addition enables non-linear analyses. With this approach the bone is modelled as a continuum characterized by its density and fabric (a measure of the orientation of trabeculae). In that study we found that the precision and accuracy of the failure load prediction from such hFE models are as good as those of micro-FE (mFE) models. Two issues, however, prohibit the clinical use of this approach. First, as mentioned before, the tested region in that study was not the same as the standard clinically measured region. Although this should be less of an issue with this mechanistic rather than empirical failure load prediction, a proper analysis of accuracy and cpu-time would require models based on the clinical region. Second, unlike mFE analyses, which are highly standardized, hFE analyses involve a large number of parameters related to the meshing (element size, density, type), the homogenization (parameters used, distance used), fabric (fabric tensor used, normalization used), material model parameters (moduli, strength, plasticity and damage parameters, local/non-local formulations), and analysis (load-steps, convergence criteria). Hence, results are reproducible only when a highly standardized implementation is available. In the earlier study, we used in-house developed software for most of these calculations. As this software is not available to other users, this would require other users to redevelop these procedures and steps. The accuracy of the calculations then would need to be re-tested, and some of the parameters may need tuning in order to get accurate results.

The overall aim of this study, therefore, was to develop a well standardized approach for mFE and hFE analyses that can provide accurate results for bone failure load predictions based on XCT2 images of the distal radius that can be used by other HR-pQCT users. Although the approach developed here is similar to the approach used in our earlier study (Hosseini *et al.*, 2017), the use of software already available to HR-pQCT users (e.g. for calculating fabric tensors) required to make some modifications. Furthermore, a more elaborate homogenization scheme was adopted and some modifications were made to material constants in order to ease their physical interpretation. The specific goals of this study therefore were first, to identify the elastic and failure parameters for mFE and hFE analyses for models based on XCT2 images when using this new standardized approach; second, to investigate the accuracy of the failure load prediction by mFE and hFE models that represent the clinical (10 mm) region using these parameters; and third, to compare the mFE and hFE performance in relation to the computational costs for a standardized implementation.

MATERIAL AND METHODS

Material

HR-pQCT images (XtremeCT II, Scanco Medical AG, Brüttisellen, Switzerland) at 60.7 microns resolution for 22 distal radius segments of 20.4 mm in size (2 stacks of 168 slices) were available from an earlier study and a detailed description can be found there (Hosseini *et al*., 2017). Briefly, the segments were obtained from 12 pairs of fresh frozen anatomic specimens of human forearms that were cut at 5 mm and at 25 mm proximal of the distal subchondral plate and included the standard 10 mm clinical region. The study was approved by the ethics committee of the Medical University of Vienna. The donors (5 female, mean age 82.4 years and 7 males, mean age of 75.1 years) had no bone related diseases and had voluntarily donated their bodies to the Center of Anatomy and Cell Biology of the Medical University of Vienna. Images were obtained using the standard clinical setting (68 kVp voltage, 1460 µA, 43 ms integration time).

Image processing

The images were processed using the standard clinical workflow. In a first step, periosteal contours were generated using an automatic contouring algorithm. In the following step the cortical and trabecular compartments were automatically defined and a Gauss filtering (sigma=0.8, support=1 voxel) and thresholding operation (320 mgHa/cm^3 for trabecular bone and 450 mgHa/cm^3 for cortical bone) were applied to generate a segmented image.

In addition, the standard clinical region was selected based on the original scout views as the region located 9 mm proximal of the reference line placed at the distal subchondral plate. To analyze the clinically relevant region, the 20.4 mm segments were cropped to one stack of 168 slices (10.2 mm).

Mechanical test data

The mechanical test data was also obtained from the earlier study (Hosseini *et al*., 2017). In summary, the 20.4 mm segments were tested in compression at a rate of 5 mm/min in a servo-hydraulic test machine in which the upper platen was fixed by a ball-bearing to optimize load transfer. Platens were sand-blasted to minimize in-plane deformation during compression. Forces were measured using a load cell and the displacement and rotations of the upper platen were captured using an optical system. From the force-displacement curves, the stiffness and failure load were calculated.

Micro-FE analysis

Micro-FE models were generated directly from the segmented images using a voxel conversion technique (van Rietbergen *et al.*, 1995) for both the 20.4 and 10.2 mm segments. All elements were assigned linear elastic material properties with a Young's modulus of E=10GPa and a Poisson's ratio of v=0.3. Boundary conditions simulated a compression test at a compressive strain of 1% in which the transversal displacement at the loaded surfaces was suppressed (as in the experiment). The stiffness of the segment was calculated as the reaction force over the applied displacement.

Three parameters were determined such that the root-mean-square error (RMSE) between predicted and measured parameters for the 20 mm segments was minimized. For the stiffness this was done by first calculating the slope β_0 of the least square regression line using a standard regression equation:

$$\beta_0 = \frac{\sum_{i=1}^{n} x_i y_i}{\sum_{i=1}^{n} x_i^2} \tag{1}$$

with x_i the stiffness values calculated from the micro-FE models, y_i the experimentally measured stiffness values and n = 22 the number of samples. The Young's modulus then was calculated as $10/\beta_0$ GPa.

The second was the 'critical volume' v_{crit} and the third parameter the 'critical strain' ε_{crit} as defined in the original criterion described in Pistoia *et al*. (2002). With the original criterion the critical volume was set to v_{crit} = 2% and the critical strain to ε_{crit} = 0.7%. To find the optimal values for these constants for models based on XCT2 images, the critical volume parameter was increased from 0.7% to 1.2% in steps of 0.1% and the critical volume parameter from 2% to 7% in steps of 1%. For each possible combination the RMSE values were calculated and the combination of parameters that provided the lowest RMSE was selected.

Homogenized-FE analyses

The homogenization approach was based on earlier studies (Hosseini *et al*., 2017; Hazrati-Marangalou *et al*., 2015), but differed in several details. A detailed overview of the steps used in this study is provided here.

In a first step, periosteal and endosteal contours were generated automatically using a standard procedure implemented in the scanner software (Burghardt *et al*., 2010). A mask image, further referred to as the full mask, then was created from the periosteal contour that represents the complete volume of the bone within the periosteal contour. Similarly, a mask was created from the endosteal contour that delineates the trabecular compartment (trabecular mask). By subtracting both masks, a mask of the cortical compartment (cortical mask) is obtained.

In a second step, the full mask was downscaled in all directions by a factor 28 to a voxel size of 1.7 mm and for each larger voxel a volume fraction was calculated based on the original number of mask voxels it contains over the total number of voxels in the larger voxel. Each larger voxel with a volume fraction that exceeds 1% was converted to an 8-node brick element (Fig. 1). The downscale factor of 28 was selected based on a mesh convergence study (Appendix A) and on the fact that 28 is a divisor of 168, which is the number of slices per stack generated by the scanner, such that the full sample can be meshed with elements of isotropic size.

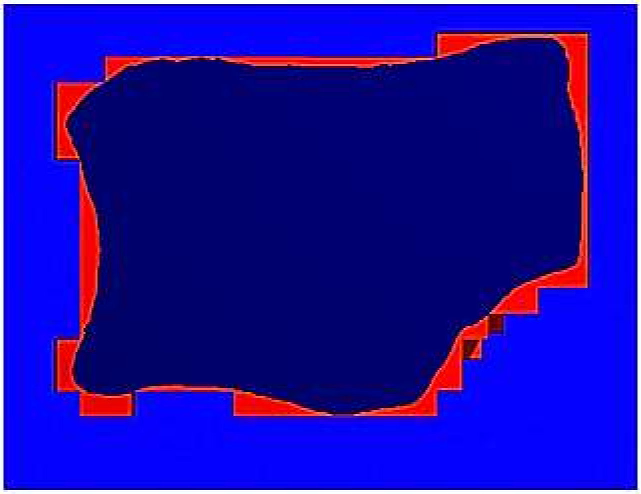

Figure 1. The downscaled full mask (red) overlaid with the original full mask (dark blue). Note that the downscaled mask includes the full mask completely.

In the third step, homogenized properties were assigned to the elements. The homogenization was done separately for the trabecular and cortical compartments. For the trabecular compartment, a spherical region with a fixed radius of 2 mm was defined around the centroid of each element. For each element the density *D* then was evaluated from the original high-resolution grey-level images by averaging the density of all voxels within the sphere region. Based on this density, a bone volume fraction ρ_{trab} was calculated as: $\rho_{trab} = D/1200$, where 1200 mgHa/cm^3 is considered the density of cortical bone (Fig. 2a). In case the sphere would have extended outside the trabecular compartment, the volume fraction was calculated only for its part within the compartment and this value was assigned to the element (Fig. 2b). In case the element was only partly within the compartment (Fig. 2c), the bone volume fraction again was calculated for the part of the sphere within the trabecular compartment and assigned only to that part of the element. To do so, also the fraction of the element that is within the trabecular compartment f_{trab} was calculated and stored. The same homogenization was also used to calculate an element fabric tensor. The fabric was calculated from the segmented image using the standard mean intercept length (MIL) instead of the Mean Surface Length (MSL) tensor as in the earlier study (Hosseini *et al.*, 2017), because the MIL tensor is also used for the standard morphological analyses. The MIL fabric tensor was normalized such that its eigenvalues m_i sum to 3.

Subsequently, the homogenization was repeated for the cortical compartment. For this compartment, however, the density and fabric were averaged over the element volume rather than a larger spherical volume (Fig. 2d). In case the element volume was covered only partly by the cortical compartment, a cortical element fraction f_{cort} was calculated and stored (Fig. 2e,f). No fabric tensor was calculated for the cortical compartment. Instead, the fabric tensor was set to the identity tensor.

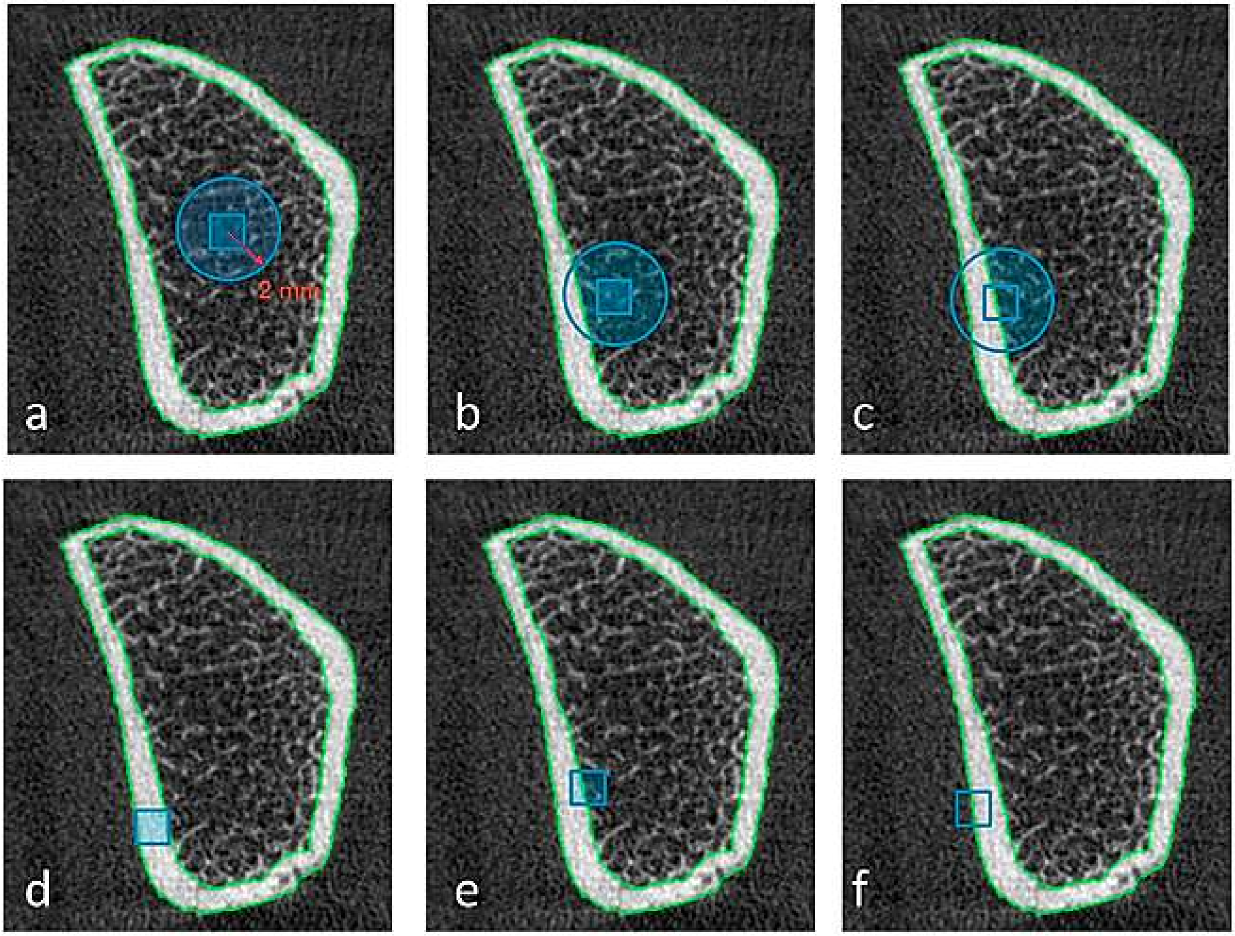

Figure 2 Top row: Density homogenization of the cancellous region for a radius cross-section with green lines delineating the periosteal and endosteal contours. The blue square represents a brick element and the blue circle the spherical region around the element centroid that is used for homogenization. Depending on the element

location, different approaches are used: a) If the spherical region was completely within the cancellous compartment, the element trabecular density (ρ_{trab}) was evaluated for the full sphere and assigned to the full element ($f_{trab} = 1$). B) If the sphere was only partly inside the cancellous compartment, the element trabecular density (ρ_{trab}) was evaluated only for the part of the sphere within the cancellous region which was assigned to the full element ($f_{trab} = 1$). C) if the sphere and the element were only partly within the cancellous compartment, the element trabecular density (ρ_{trab}) was evaluated only for the part of the sphere within the cancellous region which was assigned to the part of the element ($f_{trab} < 1$) that was within the cancellous compartment.

Bottom row: Density homogenization of the cortical region. The blue square represents a brick element, which for the cortical bone also represents the region used for homogenization. Depending on the element location, different approaches were used: d) If the element was completely within the cortical compartment, the element cortical density (ρ_{cort}) was evaluated for the full element region and assigned to the full element ($f_{cort} = 1$). e/f) If the element was only partly within the cortical compartment, the element cortical density (ρ_{cort}) was evaluated only for the part of the element that was within the cortical compartment which was assigned to the part of the element ($f_{cort} < 1$) that was within the cortical compartment.

The final density of each element then was calculated as:

$$\rho = \frac{\left(f_{trab}\rho_{trab} + f_{cort}\rho_{cort}\right)}{f_{trab} + f_{cort}} \tag{2}$$

Note that if an element is partly outside the periosteal contour the element volume fractions f_{trab} and f_{cort} do not sum to 1, indicating the element is a ‘partial volume’. As such, the density ρ represents the total density for that part of the element that is within the periosteal contour. A schematic representation of the procedure is shown in Fig. 3.

To find the averaged fabric tensor a weighted arithmetic average was calculated of the fabric tensors calculated for the cortical and trabecular compartment (Moahker, 2006). With this procedure, the individual tensor components are averaged in the same way as described in Eq. 2. The averaged fabric tensor then was again normalized.

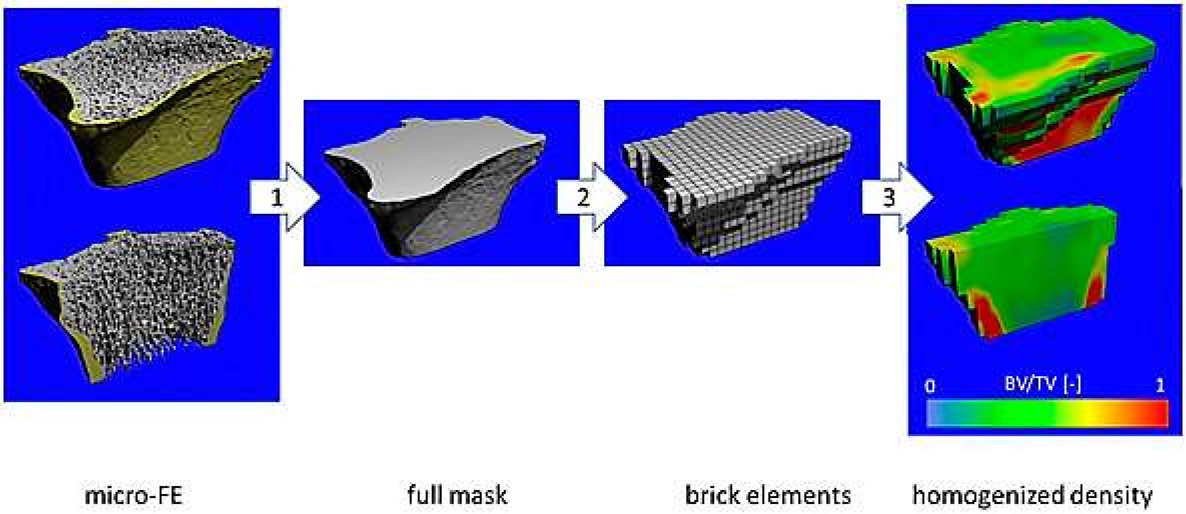

Figure 3. Schematic representation of the homogenization procedure. In a first step a 'full mask' was generated representing the volume within the periosteal contour. In a second step this mask was downscaled and segmented to obtain a 1.7 mm brick element representation. In a third step the homogenized density and fabric were calculated for each brick element and assigned to the element.

The material model used is the same as described in the previous paper. However, some of the parameters used in the earlier paper were changed to simplify their implementation and physical interpretation. Most notably, rather than a piecewise power function that relates the elastic parameters with volume fraction as well as the strength parameters with volume fraction, a single power function was used that also accounted for the element partial volume $f = f_{trab} + f_{cort}$. Accordingly, the three elastic moduli ε_i and three shear moduli μ_{ij} were calculated according to the relationship:

$$\begin{aligned} \varepsilon_i &= \varepsilon_0 f \rho^k m_i^{2l} \\ \mu_{ij} &= \mu_0 f \rho^k m_i^l m_j^l \end{aligned} \tag{3}$$

with ε_0 the elastic modulus of cortical bone, m_i the eigenvalues of the fabric tensor, the powers *k* and *l* material constants that were taken from the earlier study and μ_0 the shear modulus of bone tissue. The tensile σ_i^+, compressive σ_i^- and shear τ_{ij} strength calculations were adapted in a similar manner:

$$\begin{aligned} \sigma_i^{\pm} &= \sigma_0^{\pm} f \rho^p m_i^{2q} \\ \tau_{ij} &= \tau_0 f \rho^p m_i^q m_j^q \end{aligned} \tag{4}$$

with $\sigma_0^{\pm}$ the tensile/compressive strength and τ_0 the shear strength of bone tissue. Note that this formulation implies that moduli and strength values depend on the density and fabric according to a power function and on the partial volume according to a linear function.

As the material model differs in detail from the one used in the earlier publication, a validation study was performed first using the full 20 mm models for which mechanical test data was available. Using these models, two scaling factors were calculated to adjust elastic and strength parameters such that the root-mean-square error (RMSE) between predicted and measured parameters for the 20 mm segments was minimized. The first scaling factor was for the two elastic constants (ε_0 and μ_0). The values used in the earlier study (but corrected for the absence of the piecewise power function) were used as a starting point and a single analysis then was performed for all models. The RMSE then was minimized by scaling the elastic constants with 1/*β*, with *β* according to Eq. (1).

The second scaling factor was for the three strength constants (σ_0^-, σ_0^+ and τ_0). The values used in the earlier study were used as the starting point and a similar procedure was followed to calculate the scaling factor that would best match the calculated and measured failure load. Other parameters in the material model (*i.e.* the powers in the density relationships and the hardening constants) were taken from the previous study without tuning.

After fitting of the constants, the homogenized-FE analyses were repeated for the 10.2 mm sections and the predicted failure loads were compared to the experimentally measured ones. Since the stiffness largely depends on the height of the model, it was not considered useful to compare the stiffness values of the 10.2 mm sections to the measured stiffness values.

All image processing and finite element analyses steps were implemented in IPLFE v2.01 (Scanco Medical AG, Brüttisellen, Switzerland).

Statistics

Linear regression analyses were performed to compare the measured and calculated stiffness and failure load values:

$$y=\alpha+\beta x \tag{5}$$

with y the experimentally measured variable and x the FE-calculated variable, α the intercept and β the slope of the regression line. A linear regression t-test was used to test if the intercept was significantly different from zero and if the slope was significantly different from 1. Analyses were done using R version 3.4.2

As 20 of the 22 samples were obtained from 10 donors (each providing a left and right sample), the samples cannot be considered fully independent. To check whether systematic differences exist between the left and right samples, a paired samples t-test was performed.

RESULTS

Parameters identification

For none of the parameters investigated a significant difference between the experimentally measured or FE-calculated means left and right arm samples was detected, so the samples were further treated as independent.

Elastic parameters

For the mFE analyses, the RMSE for the predicted stiffness was minimized for a tissue Young's modulus of 10.83 GPa. Since the latter value was very close to the original value used in most earlier studies (10 GPa) and since the slope of the least-square regression line when using this original value ($\beta_0 = 0.924$) was not significantly different from 1, it was decided to leave the tissue Young's modulus value to 10 GPa (Appendix B). The linear regression model then predicted the measured stiffness with a coefficient of determination $R^2 = 0.853$, a slope of 1.057 and an intercept that was not significantly different from zero (Fig. 4).

For the hFE analyses, the RMSE for the predicted stiffness was minimized when scaling the elastic constants by a factor 1.534 (relative to the values reported in the earlier study that used a piecewise power function). The resulting moduli were 19.01 GPa and 7.851 GPa for the Young's modulus and shear modulus respectively (Appendix B). The linear regression model then predicted the measured stiffness with a coefficient of determination $R^2 = 0.856$, a slope that was not significantly different from 1 and an intercept that was not significantly different from zero (Fig. 4).

Strength parameters

For the mFE analyses, the smallest RMSE was found when the critical strain was set to 1.0% and the critical volume to 5%. The final RMSE then was 620 N, which was similar to the best values found in an earlier study for XCT1 based analysis (Mueller *et al.*, 2011). Using these parameters, the linear regression model predicted the measured failure load with a coefficient of determination $R^2 = 0.969$, a slope of 1.035 and an intercept that was not significantly different from zero (Fig. 4).

For the hFE analyses, using the moduli as described in the previous section, the RMSE for the predicted failure load was minimized when applying a scaling value of 0.753 for the strength parameters, resulting in a compressive strength σ_0^- = 166 MPa, a maximum tensile strength σ_0^+ = 131 MPa and a maximum shear strength τ_0 = 67.3 MPa (Appendix B).

Using these parameters, the linear regression model predicted the measured failure load with a coefficient of determination R^2 = 0.966, an intercept of 925 N and a slope that was not significantly different from 1 (Fig. 4).

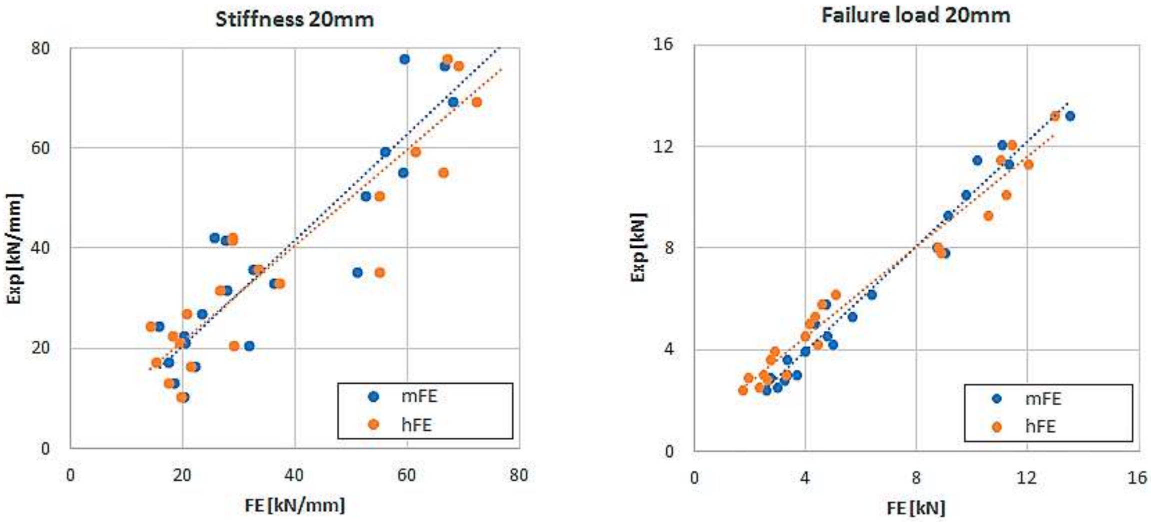

	Parameter	α	*β*	R^2
mFE	Stiffness	-588.8#	1.057	0.853
hFE	Stiffness	2299#	0.955*	0.856
mFE	Fult	-232.4#	1.035	0.969
hFE	Fult	925.0	0.890*	0.966

Not significantly different from 0, $p<0.05$

* Not significantly different from 1, $p<0.05$

Figure 4. Regression of the FE-predicted stiffness (left) and failure load (right) with the experimentally measured values for the 20 mm segments.

Failure load calculation for the clinical region

Using the set of identified constants (Appendix B), the failure load was calculated for the clinical region. For the mFE analyses, the linear regression model predicted the measured failure load with a coefficient of determination $R^2 = 0.955$, a slope that was not significantly different from 1, and an intercept that was not significantly different from zero (Fig. 5).

For the hFE analyses, the linear regression model predicted the measured failure load with a coefficient of determination $R^2 = 0.952$, a slope of 0.780 and an intercept that was not significantly different from zero (Fig. 5).

A Bland-Altman plot was created to investigate differences between the failure loads predicted from the 20 mm segment models with those predicted from the clinical region models (Fig. 6, top). For all hFE models an overprediction of the failure load was found (0.6 – 3.6 kN) that was higher for the stiffer segments. For the mFE models a much smaller overprediction was found (0.06 – 0.75 kN) that remained constant over the range of failure loads measured. Two additional Bland-Altman plots were created to investigate differences between the failure loads predicted from both 20 and 10 mm segment models with those experimentally measured. For the 20 mm models, both mFE and hFE presented small differences (Fig. 6, bottom left), while for the 10 mm models, only the hFE models showed large differences (Fig. 6, bottom right).

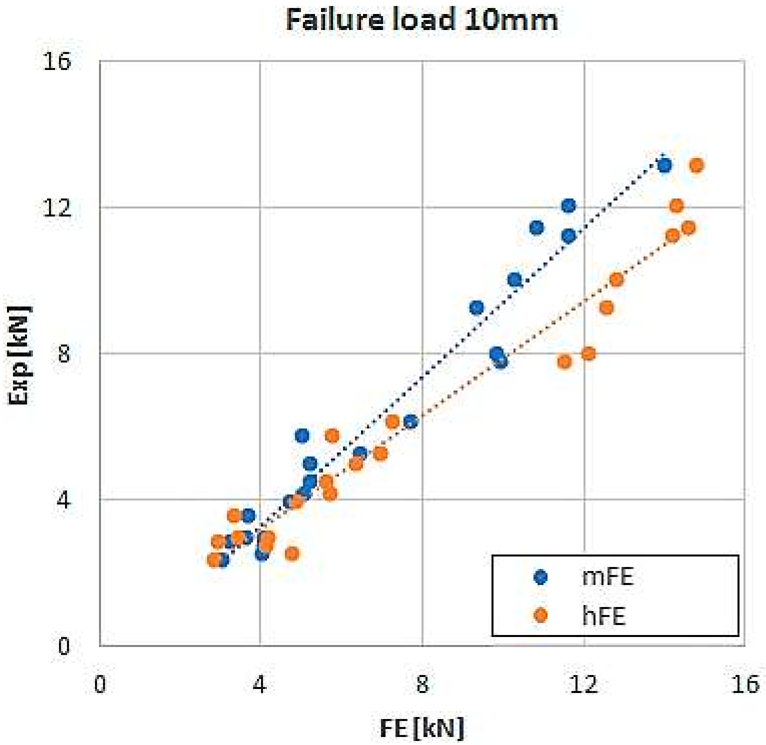

	Parameter	α	β	R^2
mFE	Fult	-770.6[#]	1.021*	0.955
hFE	Fult	102.4[#]	0.780	0.952

[#] Not significantly different from 0, $p<0.05$

* Not significantly different from 1, $p<0.01$

Figure 5. Regression of the FE-calculated failure load based on the 10 mm segments (horizontal axis) and the experimentally measured failure load for the 20 mm segments (vertical axis)

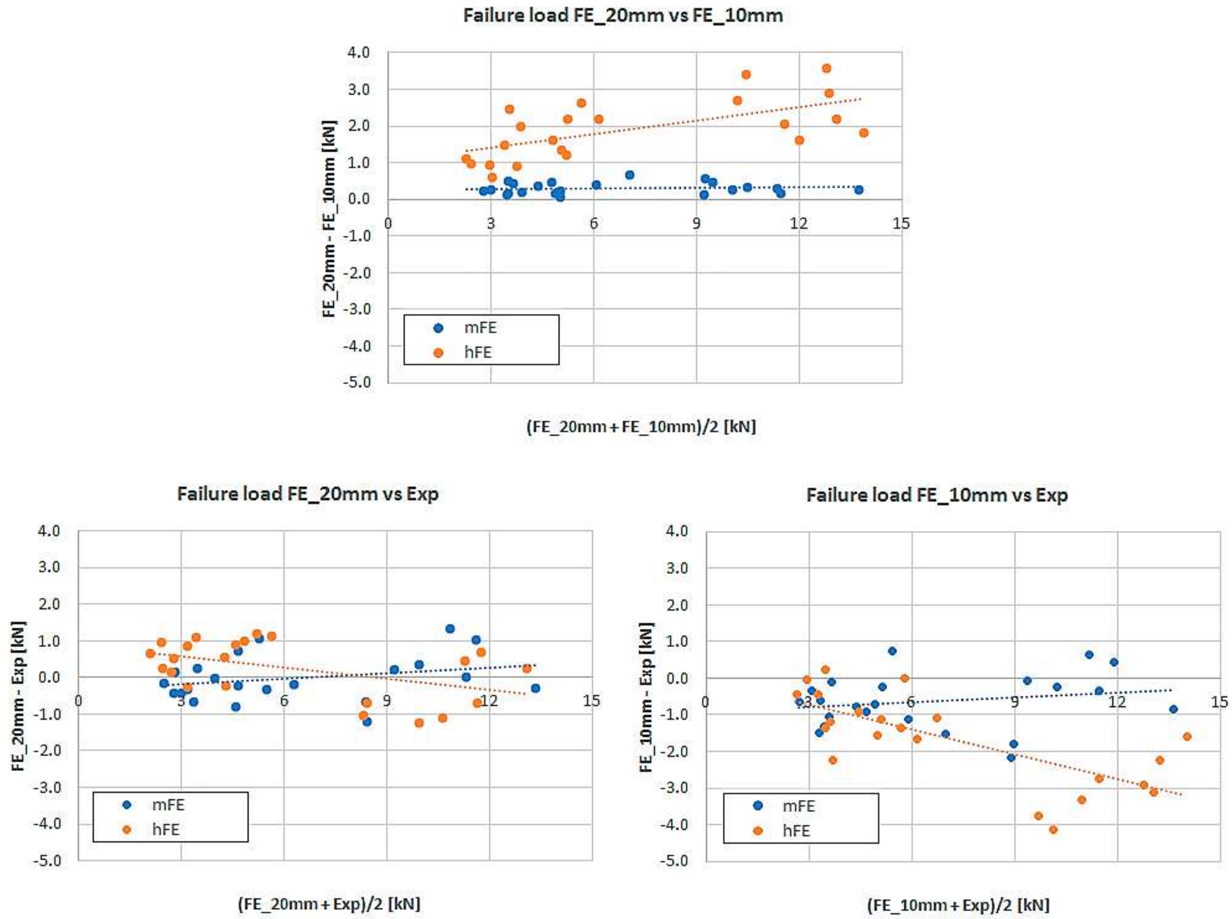

Figure 6. Bland-Altman plots to compare the failure load calculated for 20 mm segments with the failure load calculated for the 10 mm segments (top), the failure load calculated for 20 mm segments with the experimentally measured failure load (bottom left), and the failure load calculated for 10 mm segments with the experimentally measured failure load (bottom right).

Cpu-time results

All analyses were performed using 1 core of an HP Integrity Server rx2800. For the 10 mm segments, the average cpu-time required for solving the mFE models was 3h45m (SD: 1h05m). A full non-linear homogenized analysis with 1.7 mm elements took on average 0h10m (SD: 6m), with roughly 30% of the cpu-time spent on solving of the hFE model and the rest on image pre-processing steps and homogenization. The cpu-time for solving the homogenized models, however, exponentially increased with reduced element size. Compared to the 1.7 mm elements, the cpu-time for solving the homogenized models with 1 mm models roughly increased by a factor 100 (Appendix A).

DISCUSSION

The first goal of this study was to identify the elastic and failure parameters for mFE and hFE analyses when using models based on XCT2 images. For the mFE analyses, the default Young's modulus of 10 GPa provided accurate results. This value is in good agreement with values reported from bending-, tension- and nanoindentation-tests of wet human trabecular bone (Wu *et al*., 2018), but is considerably lower than values typically reported for cortical bone (~19 GPa). It is also less than the value found when comparing the stiffness of elastic specimens obtained from micro-FE models with experimental measurement (Wu *et al*., 2018; Bayraktar *et al*., 2004). Possible explanations for this discrepancy are the limited resolution of the models, the chosen threshold settings that will still result in some overestimation of the BV/TV (Manske *et al*., 2015) and the restrictive boundary condition used that can lead to an overestimation of the model stiffness (and hence underestimation of the tissue Young's modulus) (Panyasantisuk *et al*., 2016). As the Young's modulus used here was the same as that used in the earlier study (Hosseini *et al*., 2017), the results for the stiffness were the same as in that earlier study, although the regression constants are slightly different due to differences in statistical analysis. Our results are also in agreement with those of a recent study by Whittier *et al*. (2018), who reported a tissue Young's modulus of 8,748 MPa for XCT2 models. In their study, this value was obtained by comparing micro-FE results of models based on XCT2 images with those obtained from earlier validated XCT1 models of the same bones. The fact that their reported tissue modulus is still 13% less than the one we report potentially can relate to the fact that they did an *in-silico* validation whereas we performed an experimental validation. It is possible as well though that these differences relate to differences in the experimental set-up used in the original validation experiment (in particular the use of sand-blasted versus polished platens). Whereas no changes were needed for the tissue Young's modulus, the original mFE strength parameters according to Pistoia *et al*. (2002) need to be changed as the original ones would lead to a severe underestimation of the bone failure load, a result that was reported as well by others (Agarwal *et al*., 2016; Whittier *et al*., 2018). When using the new constants as listed in Appendix B, an accurate estimation of the failure load was obtained with excellent coefficient of determination ($R^2 = 0.9686$).

For the hFE analyses, results differ relative to the earlier study because of differences in implementation, homogenization approach and fabric tensor used. As a result, the moduli and strength parameters identified in the present study differ substantially from those in the earlier study. The parameters found here, however, have a clearer interpretation as they directly represent the moduli/strength values of bone tissue. The values found for the tissue Young's modulus is in excellent agreement with values reported for cortical bone (e.g. Mirzaali *et al*. (2016) reported a value of 18.97 GPa) and with values reported for bone tissue in the literature obtained from nanoindentation (e.g. Rho *et al*. (1999) reported a value of 19.4 GPa and Kim *et al*. (2014) a value of 20 GPa for osteoporotic bone).

It should be noted that the failure load values measured in the earlier study and used in this study (average 6.3 kN) are somewhat higher than those reported in other studies (Pistoia *et al*., 2002; Varga *et al*., 2010; Mueller *et al*., 2011). These differences relate to differences in the material used and in the experimental set-up. As a consequence, the failure loads predicted by the mFE and hFE using the parameters proposed here will be higher than those predicted in earlier normative studies (Dalzell *et al*., 2009; Burt *et al*., 2016).

A second goal of this study was to investigate the accuracy of mFE and hFE models that represent the clinical 10 mm region using the new parameters. The results show that both models can predict the failure load of the 20 mm segments with a very similar and high coefficient of determination ($R^2 > 0.95$). The mFE models also provided good accuracy, with a non-significant intercept and a slope that was not significantly different from 1. The hFE models, on the other hand, tended to overpredict the failure load measured for the 20 mm segments when the model was restricted to the clinical section. A likely explanation for this overprediction is that in the experiment the actual failure occurred (partly) outside the clinical region. A plot of the accumulated damage (Appendix C) at the end of the loading curve revealed that, indeed, most of the damage for the 20 mm segments is expected at the distal boundary, while the predicted damage for the clinical segment is more uniform. This explanation agrees with earlier findings that demonstrated that more accurate predictions of distal radius failure load are possible if the clinical region is shifted further distally towards the region where many fractures occur (Mueller *et al*., 2011). The fact that this was not found for the mFE models might have several causes. First, the applied boundary conditions will stiffen the bone near the cut surfaces, which will reduce the deformations in particular in the weaker parts. Second, as these models are linear, the failure load is always based on the initial tissue strain distribution in the intact configuration. Third, the critical volume v_{crit}, in an absolute sense, is reduced in the clinical region models compared to the 20 mm segments, which can slightly increase the predicted failure load (Mueller *et al*., 2011).

The third goal was to compare the mFE and hFE performance in relation to the computational costs. As the performance is very similar, only the cpu-time can be considered, which was around 22 times less for the hFE than for the mFE analyses. As presently only a standard FE solver is implemented, cpu-time for solving will exponentially increase when reducing the element size (Appendix A). Considering the results obtained in this study, however, there is no need to further reduce the element size.

A few limitations of the present study need to be discussed. First, 20 of the 22 tests specimens were obtained from 10 donors, and thus cannot be considered as fully independent samples. For that reason, the earlier study (Hosseini *et al*., 2017) calculated a marginal and a conditional coefficient of determination, which however complicates the comparison between the methods and with earlier studies. In the present study, instead, we checked if systematic differences could be detected between left and right arm parameters, and further treated the samples as independent because we found no significant differences. Although the latter does not formally prove that the samples are independent, at least it provides some support for the assumption that no complications are to be expected by considering the samples as independent. An alternative option would be to make separate relationships for the left and right arm, but this was considered undesirable as there are no reasons to assume a difference between left and right arm bone strength, which is also supported by the results of the t-test. Averaging the left and right values would be statistically correct but obviously has the major disadvantage that it would halve the number of data points. Second, to simplify the workflow, calibration steps as performed in the previous study for BV/TV and the fabric tensor were not explicitly implemented in the present study but were implicitly accounted for by the tuning procedure. It is possible that accounting for the calibration would have changed the value of the constants, but the effects are expected to be very small. Third, the geometric representation of the models is coarse. The use of tetrahedron elements rather than the brick elements used here would have resulted in a much more accurate geometric representation. However, it was found that the results of such models using tetrahedron elements are almost identical to those of the present hexahedron (average difference in failure load was 0.7%, max. difference 4.3%) while the cpu-time for homogenization and solving is increased by approximately 5 times. As such, using such models for this application has no advantages other than that these models provide a better geometric representation. Fourth, in the earlier study (Hosseini et al., 2017) the reproducibility of the hFE was found to be slightly less than that of the mFE approach. Although this was not tested, it is expected that the hFE reproducibility would be improved in the present study because of the reduced number of processing steps and manual input. Finally, as demonstrated in the mesh convergence study, the failure load was not truly converged. Whereas this could be improved by using a non-local implementation, it is expected that this will not change the results much as the element size used here is close to the length scale that would be required for the non-local implementation

As one of the overall aims of this study was to develop a well standardized approach that can be used by others, the scripts and tasks to perform these homogenized- and micro- FE analyses will be made available as additional material (Appendix D) (Requires Scanco IPLFE v2.01 or higher to run).

In conclusion, by using the material parameters determined in this study, it is possible to accurately predict the stiffness and failure load using either a micro-FE or homogenized-FE approach. The latter has the advantage of being at least an order of magnitude faster.

Conflict of Interest

Bert van Rietbergen is a consultant for Scanco Medical AG.

Acknowledgements

This study was supported by the grants program “Programa de Formación Doctoral Francisco José de Caldas Generación del Bicentenario” awarded by the Francisco José de Caldas Institute for the Development of Science and Technology (COLCIENCIAS, Colombia) LASPAU ID 20110290 and by funding (grant no 14311.1 PFLS-LS) obtained from the Swiss Commission for Technology and Innovation CTI.

REFERENCES

Agarwal S., Rosete F., Zhang C., McMahon D.J., Guo X.E., Shane E., Nishiyama K.K., 2016. In vivo assessment of bone structure and estimated bone strength by first- and second-generation HR-pQCT. *Osteoporosis International* 27(10):2955-2966.

Bayraktar H.H., Morgan E.F., Niebur G.L., Morris G.E., Wong E.K., Keaveny T.M., 2004. Comparison of the elastic and yield properties of human femoral trabecular and cortical bone tissue. *Journal of Biomechanics* 37(1):27-35.

Boutroy S., van Rietbergen B., Sornay-Rendu E., Munoz F., Bouxsein M.L., Delmas P.D., 2008. Finite element analysis based on in vivo HR-pQCT images of the distal radius is associated with wrist fracture in postmenopausal women. *Journal of Bone and Mineral Research* 23(3):392-399.

Burghardt A.J., Buie H.R., Laib A., Majumdar S., Boyd S.K., 2010. Reproducibility of direct quantitative measures of cortical bone microarchitecture of the distal radius and tibia by HR-pQCT. *Bone* 47(3):519-528.

Burt L.A., Schipilow J.D., Boyd S.K., 2016. Competitive trampolining influences trabecular bone structure, bone size, and bone strength. *Journal of Sport and Health Science* 5(4):469-475.

Dalzell N., Kaptoge S., Morris N., Berthier A., Koller B., Braak L., van Rietbergen B., Reeve J., 2009. Bone micro-architecture and determinants of strength in the radius and tibia: age-related changes in a population-based study of normal adults measured with high-resolution pQCT. *Osteoporosis International* 20(10):1683-1694.

Hazrati-Marangalou J., Ito K., van Rietbergen B., 2015. A novel approach to estimate trabecular bone anisotropy from stress tensors. *Biomechanics and Modeling in Mechanobiology* 14(1):39-48.

Hosseini H.S., Dünki A., Fabech J., Stauber M., Vilayphiou N., Pahr D., Pretterklieber M., Wandel J., van Rietbergen B., Zysset P.K., 2017. Fast estimation of Colles' fracture load of the distal section of the radius by homogenized finite element analysis based on HR-pQCT. *Bone* 97:65-75.

Kim G., Cole J.H., Boskey A.L., Baker S.P., van der Meulen M.C., 2014. Reduced tissue-level stiffness and mineralization in osteoporotic cancellous bone. *Calcified Tissue International* 95(2):125-131.

Laib A., Rüegsegger P., 1999. Comparison of structure extraction methods for in vivo trabecular bone measurements. *Computerized Medical Imaging and Graphics* 23(2):69-74.

Macneil J.A., Boyd S.K., 2008. Bone strength at the distal radius can be estimated from high-resolution peripheral quantitative computed tomography and the finite element method. *Bone* 42(6):1203-1213.

Manske S.L., Zhu Y., Sandino C., Boyd S.K., 2015. Human trabecular bone microarchitecture can be assessed independently of density with second generation HR-pQCT. *Bone* 79:213-221.

Manske S.L., Davison E.M., Burt L.A., Raymond D.A., Boyd S.K., 2017. The Estimation of Second-Generation HR-pQCT From First-Generation HR-pQCT Using In Vivo Cross-Calibration. *Journal of Bone and Mineral Research* 32(7):1514-1524.

Mirzaali M.J., Schwiedrzik J.J., Thaiwichai S., Best J.P., Michler J., Zysset P.K., Wolfram U., 2016. Mechanical properties of cortical bone and their relationships with age, gender, composition and microindentation properties in the elderly. *Bone* 93:196-211.

Moahker M., 2006. On the averaging of symmetric positive-definite tensors. *Journal of Elasticity* 82:273-296.

Mueller T.L., Christen D., Sandercott S., Boyd S.K., van Rietbergen B., Eckstein F., Lochmüller E.M., Müller R., van Lenthe G.H., 2011. Computational finite element bone mechanics accurately predicts mechanical competence in the human radius of an elderly population. *Bone* 48(6):1232-1238.

Panyasantisuk J., Pahr D.H., Zysset P.K., 2016. Effect of boundary conditions on yield properties of human femoral trabecular bone. *Biomechanics and Modeling in Mechanobiology* 15(5):1043-1053.

Pistoia W., van Rietbergen B., Lochmüller E.M., Lill C.A., Eckstein F., Rüegsegger P., 2002. Estimation of distal radius failure load with micro-finite element analysis models based on three-dimensional peripheral quantitative computed tomography images. *Bone* 30(6):842-848.

Rho J.Y., Roy II M.E., Tsui T.Y., Pharr G.M., 1999. Elastic properties of microstructural components of human bone tissue as measured by nanoindentation. *Journal of Biomedical Materials Research* 45(1):48-54.

Samelson E.J., Broe K.E., Xu H., Yang L., Boyd S., Biver E., Szulc P., Adachi J., Amin S., Atkinson E., Berger C., Burt L., Chapurlat R., Chevalley T., Ferrari S., Goltzman D., Hanley D.A., Hannan M.T., Khosla S., Liu C.T., Lorentzon M., Mellstrom D., Merle B., Nethander M., Rizzoli R., Sornay-Rendu E., Van Rietbergen B., Sundh D., Wong A.K.O., Ohlsson C., Demissie S., Kiel D.P., Bouxsein M.L., 2019. Cortical and trabecular bone microarchitecture as an independent predictor of incident fracture risk in older women and men in the Bone Microarchitecture International Consortium (BoMIC): a prospective study. *The Lancet Diabetes & Endocrinology* 7(1):34-43.

van Rietbergen B., Weinans H., Huiskes R., Odgaard A., 1995. A new method to determine trabecular bone elastic properties and loading using micromechanical finite-element models. *Journal of Biomechanics* 28(1):69-81.

van Rietbergen B., Ito K., 2015. A survey of micro-finite element analysis for clinical assessment of bone strength: the first decade. *Journal of Biomechanics* 48(5):832-841.

Varga P., Pahr D.H., Baumbach S., Zysset P.K., 2010. HR-pQCT based FE analysis of the most distal radius section provides an improved prediction of Colles' fracture load in vitro. *Bone* 47(5):982-988.

Whittier D.E., Manske S.L., Kiel D.P., Bouxsein M., Boyd S.K., 2018. Harmonizing finite element modelling for non-invasive strength estimation by high-resolution peripheral quantitative computed tomography. *Journal of Biomechanics* 80:63-71.

Wu D., Isaksson P., Ferguson S.J., Persson C., 2018. Young's modulus of trabecular bone at the tissue level: A review. *Acta Biomaterialia* (78):1-12.

Chapter 6

General Discussion

Main Findings

The main goal of this thesis was to investigate to what extent micro-FE analysis based on high resolution CT-images can accurately estimate material properties of intact and damaged bone tissue. The first section of the thesis (chapters 2 and 3) focused on mechanical properties of damaged bone. In chapter 2, the ability of micro-FE analysis based on micro-CT images to estimate the compressive stiffness of fractured cancellous bone was investigated first. Subsequently in chapter 3, the stiffness after cementing the fractured samples was measured and estimated from micro-FE. In these studies, trabecular samples were micro-CT scanned and tested in compression before and after fracture and after cement fixation. Different types of fractures were induced, varying from a smooth osteotomy-like fracture to a rough comminuted fracture caused by impact at high speed. The experimentally measured loss in stiffness due to a fracture ranged from 37% to 86% depending on the type of fracture. The stiffness measured after cement fixation was 12% to 53% less than the original intact stiffness. The micro-FE analyses overestimated the stiffness after a fracture for rough fractures, while good agreement between micro-FE and experimental results was found for smooth fractures. For the cemented cases, micro-FE underpredicted the stiffness of smooth cemented fractures while it overpredicted that of rough cemented fractures. In a post-analysis, the results of which are not reported in these chapters, we also investigated if changes in stiffness after the fracture and after the cement application could be predicted from bone morphology parameters. The hypothesis was that morphology parameters, such as trabecular separation (Tb.Sp) may determine the intermingling of trabeculae after putting the fragments together and thus may determine the compressive stiffness. Such parameters potentially also determine the cement interlock. It was found, however, that bone morphology parameters did not provide a better predictor of the stiffness after fracture or cement application. Only some additional cement morphology parameters were found to be correlated with the stiffness after cement stabilization, but only for the roughest fracture and coefficients of determination were modest at best ($R^2 < 0.43$).

As the first goal of diagnosis should be to avoid bone fractures, the second part of the thesis (chapters 4 and 5) focused on the bone strength prediction. In chapter 4, this is done for small animal models. The investigation was focused on an assessment of the accuracy of beam theory to predict yield strength of small animal long bones by comparing results based on beam theory with those based on micro-FE models. Rat Femurs of two age groups were scanned using micro-CT and subjected to a three-point bending test from which the yield force was obtained. The tissue yield stress then was calculated by regressing the experimental results with results obtained from beam theory and micro-FE analysis. It was found that the bone strength calculated from beam theory overpredicted that calculated from micro-FE by 8.0%. When comparing results for the age groups a similar increase in tissue strength was found for beam theory and micro-FE, but significant differences over time were found only for the micro-FE tissue yield stress.

Chapter 5 focused on the mechanical analysis of human bone strength based on HR-pQCT in-vivo scans. Although this method has been validated in several studies for the first generation of this type of scanner, there was no validation yet for the second generation of HR-pQCT devices, even though it was clear that strength and stiffness parameters need changes. The goal of this chapter therefore was to establish optimal parameters when performing micro-FE and also homogenized FE analyses to provide accurate failure load predictions for the standard scan region of the distal radius based on second-generation HR-pQCT images. Compared to micro-FE analyses based on first generation images, the number of elements in the models is increased by a factor of around 2.5 due to the higher resolution. Consequently, the processing time of the micro-FE models was increased by a factor of around 4, which implies solving times in the range of 6 to 24 hours (depending on site and size), which can become an inhibiting factor when analyzing large numbers of patients. For this reason, homogenized-FE was proposed as a faster alternative to estimate failure loads. Performances in terms of computational costs between micro-FE and homogenized-FE were also compared. Scans were made for cadaver radii. After identification of material parameters, micro-FE precisely predicted the measured failure load ($R^2 = 0.955$), but homogenized FE performed almost equally well ($R^2 = 0.952$) while the homogenized FE analyses were around 22 times faster than micro-FE analyses. When analyzing the standard clinical region, the homogenized FE results tended to predict failure loads that were higher than those measured experimental for the 20 mm region, indicating that the failure is expected outside (more distal of) this region. With the micro-FE analyses this effect was not found.

Compressive stiffness of fractured and cemented cancellous bone

Cancellous bone is a tissue that can absorb high levels of energy and can withstand high deformation before complete failure occurs (Keaveny *et al.*, 1993). In this study, different mechanisms to induce fractures on cancellous bone specimens were used, producing fractures with very different morphologies and with different degrees of accumulated microdamage. The different fractures showed different behaviors and responses for each of the analyzed conditions (fractured/cemented).

The smooth fracture, as expected, was the one that, on average, experienced the lowest loss in stiffness when fractured, as no damage to the bone tissue itself exists and as the two fragments typically conform well when reconnected. Also as expected, for this smooth fracture, it had the highest stiffness after cement application. This smooth fracture was the only one that micro-FE well predicted when fractured, but it also was the only one that micro-FE underpredicted when evaluating the final stiffness after cement fixation. As mentioned in chapter 3, it is not entirely clear why we found an underprediction of the cemented stiffness in this case, although not intended as an explanation, a few additional special characteristics for this type of fracture are worth mentioning. First, with this fracture type all the trabecular fractured ends were contained in the same spatial plane. This may facilitate load transfer in the compressive direction after fracture, as dense areas will be opposite to dense areas on the other site. In the case of cement application, however, the cement will be less intermingled with the bone than in the other cases and have a more ‘disc-like’ shape than in the other fracture cases. Also, the final cement orientation is more perpendicular to the loading direction than in the other cases. Without further analyses, however, it is hard to predict to what extent that would affect the experimental and micro-FE results.

For the cemented case, some additional limitations applied when inducing fractures by impact. The compressive impact fracture used in chapter 2 could not be used for cement application due to the high compaction of the bone after the fracture, that does not enable proper cement application. Instead, only the bending impact fracture was used. That case was somewhat limited as well, because due to the very irregular shape of this fracture it was not possible to reliably define the cement penetration depth.

Another characteristic that was observed in the experiments as well as the micro-FE analyses with cancellous bone specimens was the large variability within each fracture group, even though the morphology of the samples was not significantly different. This indicates that there is a stochastic component determining the results that was not captured by the parameters measured or the micro-FE analyses. This stochastic component could relate to large differences in fracture morphology even when using the same method to induce it. Although visually the fractures looked similar, it could be that specific, yet unclear, characteristics have a large effect on the compressive stiffness outcome. The stochastic component could also relate to how the specimens were placed together after the fracture. For the smooth fracture, we were able to test that, and found that small differences in orientation would have only a very modest effect on the results. For the other fracture types, it generally is not possible to reorient the fragments as these would not fit together. It is possible, however, that the reproducibility of the results after placement of the fragments is low. We did not test this here as each compression tests potentially could induce new damage to the fractured ends of the specimen, but we recommend doing so in future work. Another suggestion for future studies would be to quantify/visualize tissue damage induced by the fracture. Potentially this can be estimated from histology, or by using micro-CT techniques with radiopaque dies (Wang *et al*., 2007). This could reveal if the damage to the tissue is uniformly distributed or very local.

Strength estimation of animal long bones

In this study, the accuracy of both micro-FE analysis and beam theory to predict material properties, and particularly bending strength, was assessed (chapter 4). The starting point was the hypothesis that beam theory could well quantify the bone tissue strength from three-point bending tests of small animal long bones, since the highest stresses take place at the central section for which the cross-sectional geometry of the beam is measured. However, this hypothesis has to be rejected as it was found that the use of beam theory to calculate bone tissue strength properties from 3-point bending test results of rat femurs leads to a significant overprediction of bone tissue strength values.

Interestingly, we did not find a significant underestimation of the tissue Young's modulus, as was found in an earlier study using mice femurs (van Lenthe *et al*., 2008). When comparing this study with the one of van Lenthe *et al*. (2008), some differences that can explain the difference in results are apparent. First, femora from different species were analyzed. The study of van Lenthe included two different strains of mice whereas the present study analyzed femora from rats. Although mice and rats belong to the family Muroidea of rodents there are large differences in size (Steppan *et al*., 2004). Also, according to Silva *et al*., (2013), rats and mice have different periods of growth and bone tissue maturation.

Another difference found between van Lenthe's study and this study was the modeling of the roller supports used in the three-point bending experiments in our micro-FE study. Although this is not explicitly mentioned, we assumed that in the study by van Lenthe *et al*. the boundary conditions were applied directly to the bone at a limited number of surface nodes. This difference in boundary conditions can affect the results of the simulations. In a first analysis, we found that when modeling only surface contact between rollers and bone, an unrealistic stress pattern resulted, with very high stresses near the contact, which affected the calculated stiffness and strength. For this reason, a small indentation was modeled. In a pilot test, we first varied the indentation depth, but found no major changes when further increasing this beyond the two voxels used for the final analyses.

Finally, there were differences also in the direction and speed of the applied bending load. Femora in the study of van Lenthe *et al*. were tested at 0.5 mm/s in the anteroposterior direction. The present study tested the rat femora in posteroanterior direction at a much lower

0.1mm/min. It is possible that strain rate influences the response of bone tissue due to its viscoelastic behavior, although at the physiological or less than physiological strain rates applied here this is not expected to play a major role. The difference in orientation of the bones during testing, however, may have resulted in a somewhat different bending response as the orientation of the bone can be slightly different, which potentially could affect the results (Ferreño *et al*. 2017).

Micro-FE and Homogenized-FE strength estimations based on second generation HR-pQCT images

Our study described in chapter 5 is a follow-up study to the work described in Hosseini *et al*. (2017). In their study 20 mm distal radius segments were used to investigate to what extent micro-FE and homogenized FE could predict bone strength as experimentally measured for these segments. Rather than focusing on the 20 mm segments, we here focused on the clinical scan region, which is only 10 mm in size, and aimed at establishing a new set of parameters for the micro-FE and homogenized FE analyses.

Although the material model we used for the homogenized analyses was largely the same as that used by Hosseini *et al*. some of the parameters we found by fitting experimental and FE results are very different from those reported in Hosseini et al. Most notably, the Young's modulus that we found (19.01 GPa) is much higher than that found by Hosseini *et al*. (12.4 GPa). This, however, is largely due to the fact that we did not implement a piecewise power density function, that acts as a multiplication factor in the study by Hosseini *et al*. When compared over the full range, the differences in moduli are only modest (Fig. 1, left). On the other hand, our strength values (e.g. compressive strength of 166 MPa) are much lower than those reported by Hosseini *et al*. (220 MPa). For low density bone, the strength values actually are rather similar (Fig. 1, right). The formulation by Hosseini *et al*., however, would result in unrealistic high strength values when extrapolated to the cortical density (Fig 1, right). But as bone failure starts in low density bone regions this did not affect their results.

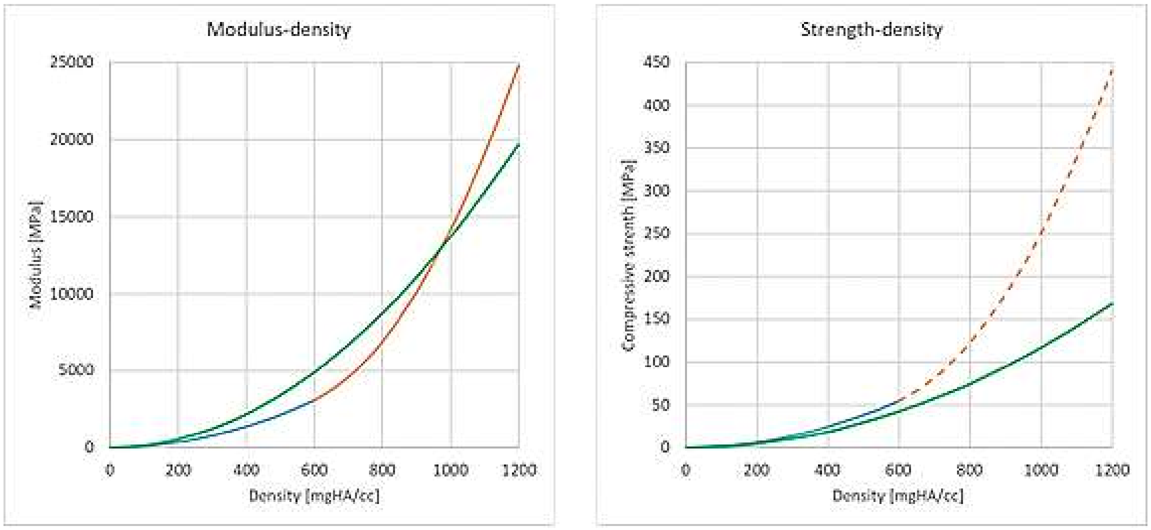

Fig 1: modulus – density relationships (left) and strength – density relationships (right) used in our study (green line) and in the earlier study by Hosseini *et al*. (blue-orange lines).

The clear advantage of the parameters used in our study is that the moduli and strength values have a clearer physical interpretation, and that they are in the ranges commonly reported for bone tissue.

A major advantage of the homogenized FE analyses over the micro-FE analyses is that they can actually simulate the failure process and that the strength criterion is not based on an empirical relationship that needs to be re-validated for every specific new situation. In theory, the same tissue properties found here should hold also when analyzing full bones, or larger regions. In this respect it is interesting that the homogenized FE results tend to predict higher strength values for the 10 mm segments compared to the 20 mm segments, which is explained by the fact that the 20 mm segments have their weakest part outside of the 10 mm clinical scan region. The micro-FE analyses actually fail to reveal this because of the empirical nature of the failure criterion. Although it was not possible to test this, it thus is expected that the micro-FE results will actually underpredict the strength of the 10 mm segments if they were experimentally tested at that height.

A major disadvantage of the homogenized FE approach obviously is the fact that trabeculae are not modeled in detail. In theory, it thus is possible that changes in the bone microstructure related to specific treatments/conditions would not be detected (or much later) by homogenized FE while they would be by micro-FE.

Future perspectives

All the work described in this thesis relies on high-resolution imaging. In order to get clinically relevant results, it should be possible to obtain such images for bone in-vivo. Presently, only HR-pQCT is available for this, but this is limited to the peripheral skeleton. Moreover, with only around 80 devices available worldwide at the time of writing this, its accessibility is limited. A potential alternative is the use of cone beam CT (CBCT) devices. Recent studies demonstrated that such devices can provide images at a voxel size of 75 microns of adequate quality to quantify bone morphology (Mys *et al*., 2018). As such devices have a larger gantry, they may be able to scan other parts of the body as well. Although the feasibility of using such devices for imaging other than peripheral sites should still be investigated, and although these devices do not provide the same physical resolution as HR-pQCT, a major advantage is that they are available at many hospitals, making it much easier to access them.

Even if the resolution would be much higher than what is presently available for in-vivo bone imaging, it seems unlikely that the actual fracture region can be well recognized from a single scan since it cannot be recognized if bone is actually connected or just touching. A potential solution for the first issue would be to overlay the image with other imaging data, such as MRI that may show the hematoma, providing more complete information.

Also deep learning, which has become a widely used artificial intelligence (AI) tool (Minnema *et al*., 2018; Mayo *et al*., 2018; Belal *et al.*, 2019), could potentially be used to distinguish those fractured tissues in HR-pQCT images. With proper training, these techniques could detect fracture patterns in neighboring trabeculae to indicate if seemingly connected trabeculae are connected or just touching, and likely obtaining in this way a better representation of the tissue.

Currently AI techniques are being implemented in diverse fields –medicine among these- and their useful applications are increasing. More studies to extend and validate potential uses of AI in clinics are expected in the coming years.

In this study, FE models based on HR-pQCT images have been demonstrated to be a reliable and accurate tool for the prediction of bone tissue properties, thanks to the ability to visualize and quantify bone microstructure, making this technique able for clinical applications including bone quality assessment, structural and topological changes and assessment of fracture risk. One challenging target for the future is to extend these possibilities to those regions where in-vivo HR-pQCT scans are not possible, such as the hip and lumbar spine, which are regions susceptible to fragility fractures. Although the resolution of whole-body CT scanners has steadily increased over the last decades, it is unlikely that they will reach a similar resolution as HR-pQCT due to dose limitation. However, in particular for the hip, it might be feasible to get morphology measurements and micro-FE results at somewhat lower resolutions (Mulder *et al.*, 2012).

Whether using HR-pQCT, CBCT or other imaging techniques, with a potential contribution from AI or multimodal imaging techniques, we expect that the computational methods used in this thesis based on high-resolution imaging will find an increased application for diagnosis, prevention, treatment and tracking of bone diseases (e.g. osteoporosis, arthrosis), for the assessment of the efficacy of orthopaedic interventions (e.g. stabilization using biomaterials) and for assessment of pharmacological interventions (e.g. drug studies).

REFERENCES

Belal S.L., Sadik M., Kaboteh R., Enqvist O., Ulén J., Poulsen M.H., Simonsen J., Høilund-Carlsen P.F., Edenbrandt L., Trägårdh E., 2019. Deep learning for segmentation of 49 selected bones in CT scans: First step in automated PET/CT-based 3D quantification of skeletal metastases. *European Journal of Radiology* 113, 89-95.

Ferreño D., Sainz-Aja j., Carrascal I.A., Diego S., Ruiz E., Casado J.A., Riancho J.A., Sañudo C., Gutierrez-Solana F., 2017. Orientation of whole bone samples of small rodents matters during bending tests. *Journal of the Mechanical Behavior of Biomedical Materials* 65, 200-212.

Hosseini H.S., Dünki A., Fabech J., Stauber M., Vilayphiou N., Pahr D., Pretterklieber M., Wandel J., van Rietbergen B., Zysset P.K., 2017. Fast estimation of Colles' fracture load of the distal section of the radius by homogenized finite element analysis based on HR-pQCT. *Bone* 97, 65–75.

Keaveny T.M., Hayes W.C., 1993. Mechanical properties of cortical and trabecular bone. *Bone* 7, 285-344.

Mayo R.C., Leung J., 2018. Artificial intelligence and deep learning – Radiology's next frontier? *Clinical Imaging* 49, 87-88.

Minnema J., van Eijnatten M., Kouw W., Diblen F., Mendrik A., Wolff J., 2018. CT image segmentation of bone for medical additive manufacturing using a convolutional neural network. *Computers in Biology and Medicine* 103, 130-139.

Mulder L., van Rietbergen B., Noordhoek N.J., Ito K., 2012. Determination of vertebral and femoral trabecular morphology and stiffness using a flat-panel C-arm-based CT approach. *Bone* 50, 200-208.

Mys K., Stockmans F., Vereecke E., van Lenthe G.H., 2018. Quantification of bone microstructure in the wrist using cone-beam computed tomography. *Bone* 114, 206-214.

Silva M.J. (Ed.), 2013. Skeletal aging and osteoporosis, biomechanics and mechanobiology. 1st ed., Springer-Verlag Berlin Heidelberg, Berlin, Germany.

Steppan S., Adkins R., Anderson J., 2004. Phylogeny and divergence-date estimates of rapid radiations in Muroid Rodents based on Multiple Nuclear Genes. *Systematic Biology* 53, 533-553.

van Lenthe G.H., Voide R., Boyd S.K., Muller R., 2008. Tissue modulus calculated from beam theory is biased by bone size and geometry: implications for the use of three-point bending tests to determine bone tissue modulus. *Bone* 43, 717-723.

Wang X., Masse D.B., Leng H., Hess K.P., Ross R.D., Roeder R.K., Niebur G.L., 2007. Detection of trabecular bone microdamage by micro-computed tomography. *Journal of Biomechanics* 40, 3397-3403.

Appendices

Appendix A

Convergence study

(Supplementary information for chapter 5)

A convergence study was executed for the 22 20-mm segments in which the element size was varied from 1.0 to 0.29 elements/mm (corresponding to an element size of 1.0mm to 3.4mm). It was found that at 0.6 elements/mm (1.7 mm element size) both the stiffness and the failure load were within 5% of the value obtained when using 1 element/mm (Fig. 1). At 0.6 elements/mm stiffness values were largely converged, but failure loads were not. The latter likely relates to the fact that no non-local formulation of the failure criterion was used. However, as the localization scale for trabecular bone would be in the range of the intertrabecular distance (1-2 mm), setting the element size to a similar value would render similar results as a non-local implementation. As the cpu-time exponentially increased with reduced element size, such that solving models with 0.6 elements/mm would solve roughly 100 times faster than those with 1 element/mm and as cpu-time was an important factor for the present study, it was concluded that 0.6 elements/mm (1.7 mm element size) would be preferable.

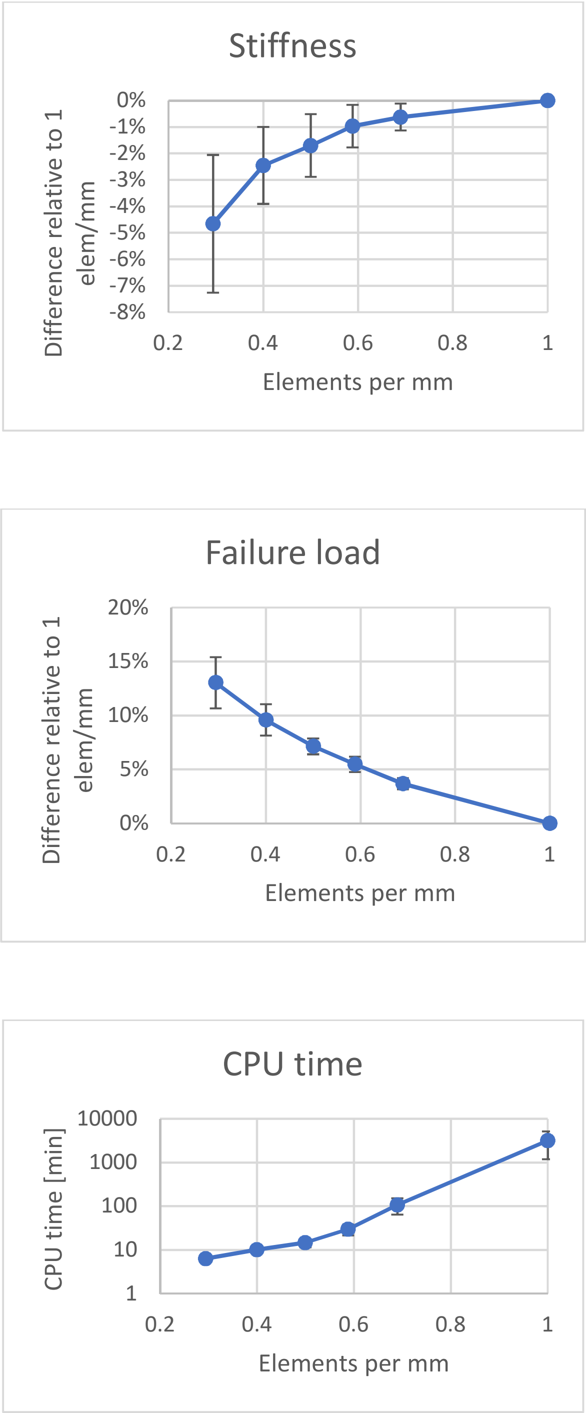

Figure 1. Effect of element size on the calculated stiffness (top-left) and failure load (top-right) and on the cpu-time needed for the full analysis (bottom). Error bars indicate the 95% confidence intervals.

Appendix B

Elastic and strength parameters used for the micro-FE and the homogenized-FE (Supplementary information for chapter 5)

Table 1: Elastic and strength parameters used for the micro-FE

Bone tissue Young's modulus	E_t [GPa]	10.0
Bone tissue Poisson's ratio	v [-]	0.3
Critical volume for failure load calculation	v_{crit} [-]	4%
Critical value for failure load estimation	ε_{crit} [-]	1%

Table 2: Elastic and strength parameters used for the homogenized FE. Bold values were determined in this study; other values were taken from (Hosseini et al., 2017)

Bone tissue Young's modulus	ε_0 [GPa]	**19.01**
Bone tissue shear modulus	μ_0 [GPa]	**7.851**
Bone tissuePoisson's ratio	v_0 [-]	0.223
Power for modulus-density relationship	k [-]	2
Power for modulus-fabric relationship	l [-]	0.96
Bone tissue compressive strength	σ_0^- [MPa]	**166**
Bone tissue tensile strength	σ_0^+ [MPa]	**131**
Bone tissue shear strength	τ_0 [MPa]	**67.3**
Interaction parameter for surface	ξ_0	$0.26BV/TV+0.23$
Power for strength-density relationship	P	1.82
Power for strength-fabric relationship	q	0.79
Prescribed cumulated plastic strain at ultimate load	$\kappa_{\max}$	0.02
Plastic hardening rate	S	100
Critical damage value	D_c	0.75
Damage rate	a	7.0

Appendix C

Damage plot (hFE) and Von Mises Strain distributions (mFE and hFE) for modelled sections (Supplementary information for chapter 5)

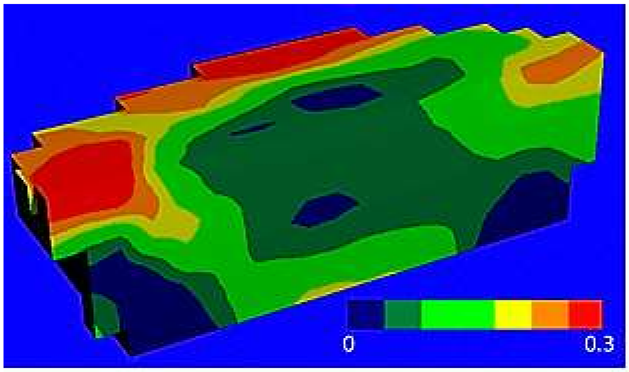

Figure 1. Damage distribution at the failure load for the hFE model of one of the samples just after reaching the failure load. The model is cut in half to reveal the inside strain distribution.

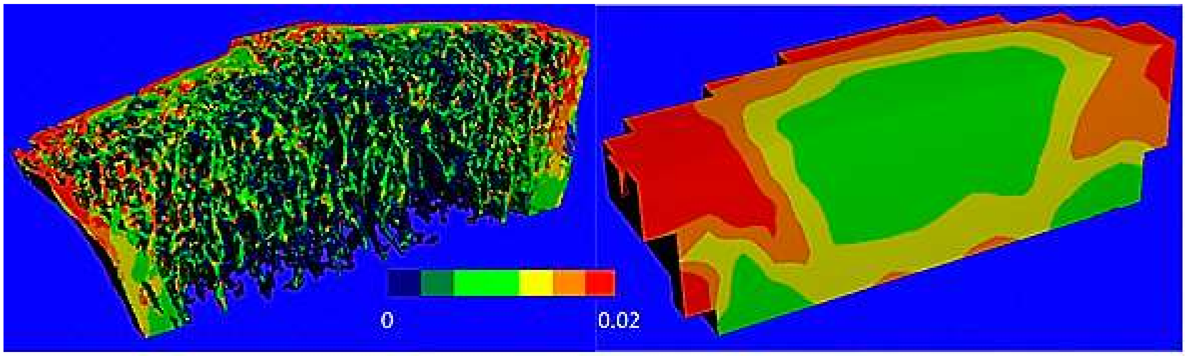

Figure 2. Von Mises strain calculated for the mFE model (left) and the hFE model (right) for one of the samples compressed to a 1% strain. The models are cut in half to reveal the inside strain distribution.

Appendix D

Scripts and tasks to perform the homogenized- and micro- FE analyses

(Supplementary information for chapter 5)

mFE analysis

```
$!
$!         _/_/_/  _/_/_/    _/
$!          _/    _/    _/  _/           Image Processing Language
$!         _/    _/_/_/    _/
$!        _/    _/        _/             (c) Eindhoven Univ. of Technology
$!     _/_/_/  _/        _/_/_/_/            Bert v. Rietbergen
$!
$!
$! Script for XtremeCT2 micro-FE analysis.
$! Requires SCANCO IPLFE v1.16 or higher to run
$!
$! Call as: @mFE.com disk2:[microct.data.00001234.00005678]c0001234.aim
$!
$! with the numbers 00001234 and 00005678 replaced by the correct sample
$! number and  measurement number respectively, and the filename c0001234
$! replaced by the correct file name. In case the data is stored at another
$! disk also the disk specification should be replaced.
$!
$! This script uses the E5E6 cortical/cancellous compartment definitions
$! Required input files: _SEG.AIM and .GOBJ
$!
$! ---------------------------------------------------------------------------
$! Definition of base filename and jobname:
$  FILENAME     = F$PARSE("''P1'",,,"NAME") - "_SEG"
$  DEV          = F$PARSE("''P1'",,,"DEVICE")
$  DIR          = F$PARSE("''P1'",,,"DIRECTORY")
$  FILEBASE     = DEV + DIR + FILENAME
$  JOB_NAME     = FILEBASE + "_MFE"
$! ---------------------------------------------------------------------------
$! Definition of symbols used in the script:
$  IPL_SEGAIM   = FILEBASE + "_SEG.AIM"         ! input: segmented aim file
$  IPL_FNAME0   = JOB_NAME + ".AIM"             ! output: FE aim file
$  IPL_FNAME1   = JOB_NAME + "_RESULT.AIM"      ! output: FE result aim file
$  IPL_GOBJ0    = FILEBASE + ".GOBJ"            ! input: periosteal contour
$  IPL_PROBLEM  = 33                            ! problem_nr
$  IPL_FEPAR_NO = 43                            ! variable_nr for post-proc.
$  IPL_FEA0     = 10000                         ! Young's modulus trab tissue
$  IPL_FEA1     = 10000                         ! Young's modulus cort tissue
$  IPL_FEA2     = "-0.05"                       ! Critical_volume for
$                                               ! strength
$  IPL_FEA3     = "0.01"                        ! Critical_value   ,,     ,,
$!
$! ---- Check if the required input files exist
$!
$  IF (F$SEARCH(IPL_SEGAIM) .EQS. "")
$  THEN
$     WRITE SYS$OUTPUT " ---------------------------------------------------"
```

```
$     WRITE SYS$OUTPUT " ERROR: cannot find file: ",IPL_SEGAIM
$     WRITE SYS$OUTPUT " This task can only run after the standard patient
$                        evaluation is completed
$     WRITE SYS$OUTPUT " ---------------------------------------------------"
$     STOP
$  ENDIF
$  IF (F$SEARCH(IPL_GOBJ0) .EQS. "")
$  THEN
$     WRITE SYS$OUTPUT " ---------------------------------------------------"
$     WRITE SYS$OUTPUT " ERROR: cannot find file: ",IPL_GOBJ0
$     WRITE SYS$OUTPUT " This task can only run after the standard patient
$                        evaluation is completed
$     WRITE SYS$OUTPUT " ---------------------------------------------------"
$     STOP
$  ENDIF
$  ON ERROR THEN EXIT
$! ---------------------------------------------------------------------------
$! First part of the IPL script: pre-processing
$! ---------------------------------------------------------------------------
$  IPLFE_BATCH

! ---- Read segmented aim generated by the default image processing. For XT2
!      this file already has different values for the cort/trab compartments

/read
  -name                       comb
  -filename                   "IPL_SEGAIM

! ---- only include the regions indicated by the gobj

/gobj_maskaimpeel_ow
  -input_output               comb
  -gobj_filename              "IPL_GOBJ0
  -peel_iter                  0

! ---- Delete unconnected parts

/cl_rank_extract
  -input                      comb
  -output                     cl
  -first_rank                 1
  -last_rank                  1
  -connect_boundary           false
  -value_in_range             1

/multiply_volumes
  -input1                     comb
  -input2                     cl
  -output                     out
  -common_region_only         false
  -multiply_zero_pixels       true

/del comb
/del cl

! ---- Remove empty space around the bone, if any
/bounding_box_cut
```

```
  -input                    out
  -output                   fem
  -z_only                   false
  -border                   0 0 0

/del out

/write
  -name                     fem
  -filename                 "IPL_FNAME0          ! (_MFE.AIM)
  -compress_type            bin
..
$! ---------------------------------------------------------------------------
$! Second part of the IPL script: the actual FE-analysis
$! ---------------------------------------------------------------------------
$  IPLFE_BATCH

/read
  -name                     fem
  -filename                 "IPL_FNAME0          ! (_MFE.AIM)

/fe_solve3
  -in                       fem
  -fea_file_name            "JOB_NAME            ! (_MFE)
  -problem_nr               "IPL_PROBLEM
  -scale_factor             -0.01
  -list_option              1
  -tolerance_force          1.000000E-03
  -tolerance_displ          1.000000E+00
  -max_nr_iter              50000
  -restart_option           0
  -comp_val_mat_001         126
  -Ymodulus_mat_001         "IPL_FEA0
  -Poissonr_mat_001         3.000000E-01
  -comp_val_mat_002         127
  -Ymodulus_mat_002         "IPL_FEA1
  -Poissonr_mat_002         3.000000E-01
  -comp_val_mat_003         0
  -Ymodulus_mat_003         1.000000E+04
  -Poissonr_mat_003         3.000000E-01
..
$! ---------------------------------------------------------------------------
$! Third part of the IPL script: post-processing
$! ---------------------------------------------------------------------------
$  IPLFE_BATCH

/db_scanco_activate
  -write                    true

! ---- use the voxgobj to get the correct threshold in the database

/read
  -name                     fem
  -filename                 "IPL_FNAME0          ! (_MFE.AIM)

/voxgobj_scanco_param
  -input                    fem
```

```
  -gobj_filename             "IPL_GOBJ0
  -peel_iter                 -1
  -region_number             0

/del fem

! ---- do the postprocessing and store results in the database

/fe_post
  -post_file_name            "JOB_NAME           ! (_MFE)
  -output                    res
  -variable_nr               "IPL_FEPAR_NO
  -loadcase_nr               1
  -list_option               1
  -interpol_option           1
  -averaging_option          0
  -test_dir                  0
  -critical_variable_nr      "IPL_FEPAR_NO       ! Not available in FE v01.*
  -critical_volume           "IPL_FEA2
  -critical_value            "IPL_FEA3

/write
  -name                      res
  -filename                  "IPL_FNAME1         ! (_MFE_RESULT.AIM)
..
$!
```

hFE analysis

```
$!
$!         _/_/_/  _/_/_/    _/
$!          _/     _/   _/  _/           Image Processing Language
$!         _/    _/_/_/    _/
$!        _/    _/        _/             (c) Eindhoven Univ. of Technology
$!     _/_/_/  _/        _/_/_/_/            Bert v. Rietbergen
$!
$!
$! Script for XtremeCT2 homogenized-FE analysis
$! Requires SCANCO IPLFE v2.01 or higher to run
$!
$! Call as: @hFE.com disk2:[microct.data.00001234.00005678]c0001234.aim
$!
$! with the numbers 00001234 and 00005678 replaced by the correct sample
$! number and measurement number respectively, and the filename c0001234
$! replaced by the correct file name. In case the data is stored at another
$! disk also the disk specification should be replaced.
$!
$! This script uses the E5E6 cortical/cancellous compartment definitions
$! Required input files: .AIM, _SEG.AIM, .GOBJ and _TRAB_MASK.GOBJ
$!
$! --------------------------------------------------------------------------
$! Definition of base filename and jobname:
$  FILENAME     = F$PARSE("''P1'",,,"NAME") - "_SEG"
$  DEV          = F$PARSE("''P1'",,,"DEVICE")
$  DIR          = F$PARSE("''P1'",,,"DIRECTORY")
```

```
$  FILEBASE     = DEV + DIR + FILENAME
$  JOB_NAME     = FILEBASE + "_HFE"
$!
$! Definition of symbols used in the script:
$  IPL_AIM      = FILEBASE + ".AIM"                ! input: aim file
$  IPL_SEGAIM   = FILEBASE + "_SEG.AIM"            ! input: segmented aim
$  IPL_FNAME0   = JOB_NAME + ".INP"                ! output: FE input inp
$  IPL_FNAME1   = JOB_NAME + "_FST_INC_RESULT.AIM"! output: first inc res.
$  IPL_FNAME2   = JOB_NAME + "_LST_INC_RESULT.AIM"! output: last inc res.
$  IPL_FNAME3   = JOB_NAME + "_BASE.INP"           ! temp: model input
$  IPL_FNAME4   = JOB_NAME + "_TRAB.INP"           ! temp: model input
$  IPL_GOBJ0    = FILEBASE + ".GOBJ"               ! input: perios. contour
$  IPL_GOBJ1    = FILEBASE + "_TRAB_MASK.GOBJ"     ! input: endost. contour
$  IPL_MISC1_0  = 28                               ! downscale factor
$  IPL_MISC1_1  = 1                                ! meshing_option
$  IPL_MISC1_2  = 1                                ! fabric_option
$  IPL_PROBLEM  = 33                               ! problem_nr
$  IPL_FEPAR_NO = 42                               ! var. for first inc.
$  IPL_FEA0     = 120                              ! var. for last inc.
$!
$! ---- Check if the required input files exist
$!
$  IF (F$SEARCH(IPL_AIM) .EQS. "")
$  THEN
$     WRITE SYS$OUTPUT " ---------------------------------------------------"
$     WRITE SYS$OUTPUT " ERROR: cannot find file: ",IPL_AIM
$     WRITE SYS$OUTPUT " This task can only run after the standard patient
evaluation is completed
$     WRITE SYS$OUTPUT " ---------------------------------------------------"
$     STOP
$  ENDIF
$  IF (F$SEARCH(IPL_SEGAIM) .EQS. "")
$  THEN
$     WRITE SYS$OUTPUT " ---------------------------------------------------"
$     WRITE SYS$OUTPUT " ERROR: cannot find file: ",IPL_SEGAIM
$     WRITE SYS$OUTPUT " This task can only run after the standard patient
                        evaluation is completed
$     WRITE SYS$OUTPUT " ---------------------------------------------------"
$     STOP
$  ENDIF
$  IF (F$SEARCH(IPL_GOBJ0) .EQS. "")
$  THEN
$     WRITE SYS$OUTPUT " ---------------------------------------------------"
$     WRITE SYS$OUTPUT " ERROR: cannot find file: ",IPL_GOBJ0
$     WRITE SYS$OUTPUT " This task can only run after the standard patient
$                       evaluation is completed
$     WRITE SYS$OUTPUT " ---------------------------------------------------"
$     STOP
$  ENDIF
$  IF (F$SEARCH(IPL_GOBJ1) .EQS. "")
$  THEN
$     WRITE SYS$OUTPUT " ---------------------------------------------------"
$     WRITE SYS$OUTPUT " ERROR: cannot find file: ",IPL_GOBJ1
$     WRITE SYS$OUTPUT " This task can only run after the standard patient
$                       evaluation is completed
$     WRITE SYS$OUTPUT " ---------------------------------------------------"
$     STOP
```

```
$  ENDIF
$!
$! ---- When using hex elements, use a low mask threshold such that any
$!      element touching the mask is included. When using tet elements,
$!      threshold at 50% to get the proper contours
$!
$  IF (IPL_MISC1_1 .EQ. 1)
$  THEN
$     SCALE_THRESHOLD == 10
$  ELSE
$     IF (IPL_MISC1_1 .EQ. 2)
$     THEN
$        SCALE_THRESHOLD == 500
$     ELSE
$        WRITE SYS$OUTPUT " -------------------------------------------------"
$        WRITE SYS$OUTPUT " Invalid meshing option: ", IPL_MISC1_1
$        WRITE SYS$OUTPUT " Valid options are 1 and 2 only
$        WRITE SYS$OUTPUT " -------------------------------------------------"
$        EXIT 2
$     ENDIF
$  ENDIF
$  ON ERROR THEN EXIT
$! ----------------------------------------------------------------------------
$! First part of the IPL script: pre-processing and homogenization
$! ----------------------------------------------------------------------------
$  IPLFE_BATCH

! ---- Read the original input files

/read
  -name                      org_in
  -filename                  "IPL_AIM

/read
  -name                      seg_in
  -filename                  "IPL_SEGAIM

/gobj_to_aim
  -gobj_filename             "IPL_GOBJ0
  -output                    full_mask_in
  -peel_iter                 0

/gobj_to_aim
  -gobj_filename             "IPL_GOBJ1
  -output                    trab_mask_in
  -peel_iter                 0

! ---- Make a common 'canvas' to which all images will be pasted to ensure
!      they are positioned in the proper way relative to each other when
!      removing the pos later

/threshold
  -input                     org_in
  -output                    tmp
  -lower_in_perm_aut_al      999999
  -upper_in_perm_aut_al      0
  -value_in_range            0
```

```
  -unit                     0

! ---- Set a border of downscale_factor voxels around the canvas in x/y-dir
!      This is needed later for better density interpolation when using tet
!      elements

/border_change
  -input                    tmp
  -output                   canvas
  -border                   "IPL_MISC1_0 "IPL_MISC1_0 0

/del tmp

! ---- Now place all images in the canvas

/concat
  -input1                   canvas
  -input2                   org_in
  -output                   org_canv
  -common_region_only       false
  -add_not_overlay          false

/del org_in

/concat
  -input1                   canvas
  -input2                   seg_in
  -output                   seg_canv
  -common_region_only       false
  -add_not_overlay          false

/del seg_in

/concat
  -input1                   canvas
  -input2                   full_mask_in
  -output                   full_mask_canv
  -common_region_only       false
  -add_not_overlay          false

/del full_mask_in

/concat
  -input1                   canvas
  -input2                   trab_mask_in
  -output                   trab_mask_canv
  -common_region_only       false
  -add_not_overlay          false

/del trab_mask_in

! ---- Now all images are pasted in the same canvas, crop all images to the
!      volume of interest (voi) which is defined as the volume of seg with a
!      border in x/y-dir of downscale_factor voxels.
!      This will remove any slices potentially lost due to slice matching
!      from all images.
```

```
! ---- first get the voi

/gobj_maskaimpeel_ow
  -input_output              seg_canv
  -gobj_filename             "IPL_GOBJ0
  -peel_iter                 0

/bounding_box_cut
  -input                     seg_canv
  -output                    voi
  -z_only                    false
  -border                    "IPL_MISC1_0 "IPL_MISC1_0 0

! Create the voi border in x/y-dir only

/set_value
  -input                     voi
  -value_object              0
  -value_background          0

! ---- then crop all images to the voi dim and pos

/concat
  -input1                    voi
  -input2                    org_canv
  -output                    org
  -common_region_only        true
  -add_not_overlay           false

/del org_canv

/concat
  -input1                    voi
  -input2                    seg_canv
  -output                    seg
  -common_region_only        true
  -add_not_overlay           false

/del seg_canv

/concat
  -input1                    voi
  -input2                    full_mask_canv
  -output                    full_mask
  -common_region_only        true
  -add_not_overlay           false

/del full_mask_canv

/concat
  -input1                    voi
  -input2                    trab_mask_canv
  -output                    trab_mask
  -common_region_only        true
  -add_not_overlay           false

/del trab_mask_canv
```

```
/del voi

/exa org geo
/exa seg geo
/exa trab_mask geo
/exa full_mask geo

! ---- Set the pos of all files to zero such that alignment of downscaled and
!      high-resolution images is exact for any down_scale_factor.
!      For example, if this is not done and the pos was 49 and the downscale
!      factor 10, the downscaled image would have a pos of 4. The error in
!      the pos thus would be 9 voxels in size. This would affect the
!      calculation of the element density/fabric later. By setting the pos to
!      zero, no such errors occur

/header_geo_set
  -input                    org
  -off_new                  -1   -1   -1
  -pos_new                   0    0    0
  -el_size_mm_new           -1.0 -1.0 -1.0

/header_geo_set
  -input                    seg
  -off_new                  -1   -1   -1
  -pos_new                   0    0    0
  -el_size_mm_new           -1.0 -1.0 -1.0

/header_geo_set
  -input                    full_mask
  -off_new                  -1   -1   -1
  -pos_new                   0    0    0
  -el_size_mm_new           -1.0 -1.0 -1.0

/header_geo_set
  -input                    trab_mask
  -off_new                  -1   -1   -1
  -pos_new                   0    0    0
  -el_size_mm_new           -1.0 -1.0 -1.0

/exa trab_mask geo

! ------ create the cortical and trabecular compartment masks

/subtract_aims
  -input1                   full_mask
  -input2                   trab_mask
  -output                   cort_mask

/set_value
  -input                    trab_mask
  -value_object             1
  -value_background         0

/set_value
  -input                    cort_mask
  -value_object             2
  -value_background         0
```

```
! ---- Generate the mesh

/fe_mesh
  -in                       full_mask
  -out_filename             "IPL_FNAME3          ! (_HFE_BASE.INP)
  -output_format            abaqus
  -down_scale_factor        "IPL_MISC1_0
  -threshold_value          "SCALE_THRESHOLD
  -threshold_unit           6
  -max_nr_groups            0
  -meshing_option           "IPL_MISC1_1
  -element_order            1
  -use_hex_as_tet           false
  -oddcase_start            true
  -optimize_bw              fasle
  -max_aspect_ratio         1.000000
  -min_side_length          0.100000
  -global_pos_flag          true
  -problem_nr               0
  -max_nr_mat               0
  -density_option           0
  -ref_density              1.000000
  -Emod_const_a             10000.000000
  -Emod_const_b             0.000000
  -Emod_const_p             1.000000
  -Poissons_ratio           0.300000

/del full_mask

! ---- calculate element density and fabric for the trabecular elements

/hfe_homogenize
  -org                      org
  -seg                      seg
  -mask                     trab_mask
  -mesh_infile_name         "IPL_FNAME3          ! (_HFE_BASE.INP)
  -mesh_outfile_name        "IPL_FNAME4          ! (_HFE_TRAB.INP)
  -VOI_radius               2.000000
  -volfrac_option           2
  -volfrac_ref_density      1200.000000
  -volfrac_min              0.001
  -fabric_option            "IPL_MISC1_2
  -fabric_min_volume        8.000000
  -fabric_min_volfrac       0.050000
  -fabric_power_transform   1.0
  -MIL_peel_iter            0
  -MIL_ip_sigma             0.000000
  -MIL_ip_support           0
  -MIL_ip_threshold         50
  -MIL_nr_ave_iter          2
  -MIL_t_dir_radius         2
  -MIL_epsilon              1.200000
  -list_option              2

/del trab_mask
```

```
! ---- calculate element density but no fabric for the cortical elements
!      Set a very small radius: will be set to element size by
!      /hfe_homogenize

/hfe_homogenize
  -org                      org
  -seg                      seg
  -mask                     cort_mask
  -mesh_infile_name         "IPL_FNAME4         ! (_HFE_TRAB.INP)
  -mesh_outfile_name        "IPL_FNAME0         ! (_HFE.INP)
  -VOI_radius               0.010000
  -volfrac_option           2
  -volfrac_ref_density      1200.000000
  -volfrac_min              0.001
  -fabric_option            0
  -fabric_min_volume        8.000000
  -fabric_min_volfrac       0.050000
  -fabric_power_transform   1.0
  -MIL_peel_iter            0
  -MIL_ip_sigma             0.000000
  -MIL_ip_support           0
  -MIL_ip_threshold         50
  -MIL_nr_ave_iter          2
  -MIL_t_dir_radius         2
  -MIL_epsilon              1.200000
  -list_option              2

/del org
/del seg
/del cort_mask
..
$  DEL 'IPL_FNAME3';*
$  DEL 'IPL_FNAME4';*
$!
$! --------------------------------------------------------------------------
$! Second part of the IPL script: the actual FE-analysis
$! --------------------------------------------------------------------------
$!
$  IPLFE_BATCH

/hfe_solve
  -in_file_name             "IPL_FNAME0         ! (_HFE.INP)
  -job_file_name            "JOB_NAME           ! (_HFE_XT2_STD)
  -Eparams                  19010. 7851 0.223
  -Epowers                  2.00 0.96 1.00
  -Sparams                  131. 166. 67.3
  -Spowers                  1.82 0.79 1.00
  -CHI                      0.23 0.26
  -Dparams                  0.750 7.000
  -Hparams                  100.000 0.020
  -problem_nr               "IPL_PROBLEM
  -scale_factor             -0.05000000
  -nod_select_tol           0.010
  -nr_steps                 100
  -tolerance                0.001
```

```
  -max_nr_iter                20
  -assembly_every_iters       3
  -max_force_drop             0.020000
  -list_option                1
..
$!
$! ---------------------------------------------------------------------------
$! Third part of the IPL script: additional post-processing
$! ---------------------------------------------------------------------------
$!
$  POST1:
$  IF (IPL_FEPAR_NO.EQ.0) THEN GOTO POST2
$  IPLFE_BATCH

/db_scanco_activate
  -write                      true

! ---- use the voxgobj to get the correct threshold in the database

/read
  -name                       in
  -filename                   "IPL_SEGAIM

/voxgobj_scanco_param
  -input                      in
  -gobj_filename              "IPL_GOBJ0
  -peel_iter                  -1
  -region_number              0

! ---- create first plot

/hfe_post
  -job_file_name              "JOB_NAME            ! (_HFE_XT2_STD)
  -out                        res
  -dim_out                    -1 -1 -1
  -pos_out                    -1 -1 -1
  -el_size_mm_out             -1 -1 -1
  -variable_nr                "IPL_FEPAR_NO
  -loadstep_nr                1
  -interpol_option            2
  -defplot_scaling            0.000000
  -list_option                1

/write
  -name                       res
  -filename                   "IPL_FNAME1          ! (_HFE_FST_INC_RESULTS.AIM)
  -compress_type              bin
..
$!
$  POST2:
$  IF (IPL_FEA0.EQ.0) THEN EXIT
$  IPLFE_BATCH

/db_scanco_activate
  -write                      true

! ---- create 2nd plot
```

```
/hfe_post
  -job_file_name            "JOB_NAME           ! (_HFE_XT2_STD)
  -out                      res
  -dim_out                  -1 -1 -1
  -pos_out                  -1 -1 -1
  -el_size_mm_out           -1 -1 -1
  -variable_nr              "IPL_FEA0
  -loadstep_nr              99999
  -interpol_option          2
  -defplot_scaling          0.000000
  -list_option              1

/write
  -name                     res
  -filename                 "IPL_FNAME2         ! (_HFE_LST_INC_RESULTS.AIM)
  -compress_type            bin
..
$!
```

Summary

Osteoporosis leads to deterioration of the bone microarchitecture, enhanced bone fragility and increased bone fracture risk due to a fall. This disease affects mainly trabecular bone, but also contributes to the thinning and increased porosity of the cortical walls, conditions that are directly associated with a reduction in bone strength. As a result, patients have a higher risk of fragility fractures. It thus is important to avoid fractures. This, however, requires an accurate diagnosis of bone fracture risk. Several studies have proposed DEXA and quantitative CT (QCT) imaging as tools for the diagnosis of bone fracture risk by measuring the bone density, although their resolution is not good enough to recognize the trabecular architecture. With the introduction of High Resolution peripheral Quantitative CT (HR-pQCT) imaging, it has become possible to image both trabecular structure and morphological changes. Several studies have investigated if morphological parameters measured by HR-pQCT are better predictors of bone fracture risk than DEXA. Although such studies have found clear differences between fracture patients and controls, it was found that the fracture risk prediction is not much improved.

Finite element (FE) modeling has been proposed to better estimate bone fracture risk, providing a direct mathematical relationship between the bone internal and external morphology and bone strength. Finite element models can be derived directly from CT scans where the geometry of the model is manually or automatically derived from the periosteal contour of the bone and subdivided in elements by using a voxel conversion technique, where bone voxels are directly converted to brick elements in the FE model. While most studies only accounted for bone density to represent the element material properties, later studies also included bone fabric to quantify bone anisotropic properties. Whereas FE models can much better predict bone strength than density or morphological analyses, their ability to predict bone fracture risk is less clear. With the introduction of the HR-pQCT, it became possible as well to perform micro-FE analyses that model that actual bone microstructure. Several studies have validated the strength prediction of micro-FE analyses based on HR-pQCT images of the distal radius and found considerable improvements over strength predictions based on DEXA aBMD or other density measures. Micro-FE has also

been used in many clinical studies to predict bone fractures. In a recent study that included results from many prospective studies, it was found that the association between fractures and micro-FE results indeed was much stronger than that of any other parameter investigated. Micro-FE analyses have also been used to measure the stiffness of fractured bone. In such studies the fractured region is scanned and micro-FE analyses involving compression/bending tests are simulated. It was found that the calculated stiffness first drops, and only after some 3 weeks the micro-FE calculated stiffness showed a clear increase in stiffness over time. Two years later, the fractured site actually had a higher stiffness than the contralateral site. Presently, however, it is still unclear what the accuracy of such micro-FE analyses of fractured bone are as unlike with intact bone, an experimental validation is not feasible. It seems likely that several systematic errors will occur, such as the fact that trabeculae that touch will be considered to be bonded and the fact that bone tissue itself may be damaged, but that this cannot be derived from the images. It was proposed that such artefacts could explain, for example, the initial drop in stiffness seen in the fracture healing studies. Similar problems may occur for bone that is treated by cement after a fracture. The cement can be visualized with HR-pQCT as these cements are radiopaque, but it presently is unclear to what extent the stiffness of bone treated with cement can be predicted by micro-FE or other analyses.

Therefore, the main goal of this thesis was to investigate to what extent micro-FE analysis based on high resolution CT-images can accurately estimate material properties of intact and damaged bone tissue. For this, chapter 1 presents the general introduction, the goals and the outline of this thesis. To reach the main goal of the thesis, chapter 2 presents the ability of micro-FE analysis to estimate the compressive stiffness of cancellous bone samples after a fracture was tested. Following, the stiffness after cementing a fractured sample was measured and compared to the fractured and unfractured situation (chapter 3). In this study also, micro-FE was used in order to test if it can predict the stiffness of cemented bone. In these studies, trabecular samples were micro-CT scanned and tested in compression before and after fracture and after cement fixation. Different types of fractures were induced, varying from a smooth osteotomy-like fracture to a rough comminuted fracture caused by impact at high speed. The experimentally measured loss in stiffness due to a fracture ranged from 37% to 86% depending on the type of fracture. The stiffness measured after cement fixation was 12% to 53% less than the original intact stiffness. The micro-FE analyses overestimated the stiffness after a fracture for rough fractures, while good agreement between micro-FE and experimental results was found for smooth fractures. For the cemented cases, micro-FE underpredicted the stiffness of smooth cemented fractures while it overpredicted that of rough cemented fractures. It was also found that bone morphology parameters did not provide a better predictor of the stiffness after fracture or cement application.

As the first goal of diagnosis should be to avoid bone fractures, the second part of the thesis focused on the bone strength prediction. In chapter 4, this is done for small animal models where the investigation was focused on an assessment of the accuracy of beam theory to predict yield strength of small animal long bones by comparing results based on beam theory with those based on micro-FE models. Rat Femurs of two age groups were scanned using micro-CT and subjected to a three-point bending test from which the yield force was obtained. The tissue yield stress then was calculated by regressing the experimental results with results obtained from beam theory and micro-FE analysis. It was found that the bone strength calculated from beam theory overpredicted that calculated from micro-FE by 8.0%. When comparing results for the age groups a similar increase in tissue strength was found for beam theory and micro-FE, but significant differences over time were found only for the micro-FE tissue yield stress.

Chapter 5 focused on the mechanical analysis of human bone strength based on HR-pQCT in-vivo scans. Although this method has been validated in several studies for the first generation of this type of scanner, there was no validation yet for the second generation of HR-pQCT devices, even though it was clear that strength and stiffness parameters need changes. The goal of this chapter therefore was to establish optimal parameters when performing micro-FE and also homogenized FE analyses to provide accurate failure load predictions for the standard scan region of the distal radius based on second-generation HR-pQCT images. Compared to micro-FE analyses based on first generation images, the number of elements in the models is increased by a factor of around 2.5 due to the higher resolution. Consequently, the processing time of the micro-FE models was increased by a factor of around 4, which implies solving times in the range of 6 to 24 hours (depending on site and size), which can become an inhibiting factor when analyzing large numbers of patients. For this reason, homogenized-FE was proposed as a faster alternative to estimate failure loads. Performances in terms of computational costs between micro-FE and homogenized-FE were also compared. Scans were made for cadaver radii. After identification of material parameters, micro-FE precisely predicted the measured failure load ($R^2 = 0.955$), but homogenized FE performed almost equally well ($R^2 = 0.952$) while the homogenized FE analyses were around 22 times faster than micro-FE analyses. When analyzing the standard clinical region, the homogenized FE results tended to predict failure loads that were higher than those measured experimental for the 20 mm region, indicating that the failure is expected outside (more distal of) this region. With the micro-FE analyses this effect was not found.

Finally, Chapter 6 summarizes the main findings and implications of the studies described in previous chapters of this dissertation as well as the future perspectives.

In summary, this PhD thesis introduces novel FE applications that can be used to diagnose, analyze and predict bone mechanical properties at the bone organ-level as well as on the bone tissue-level for a wide range of (pre-)clinical applications.

Curriculum Vitae

Andrés Julián Arias-Moreno was born in Bogotá, Colombia. He obtained a bachelor degree in Mechanical Engineering at the National University of Colombia in 2006. He studied a specialization in Bioengineering obtaining his degree in 2007 at the District University of Bogotá, Colombia. Then he received a scholarship to study a master in Biomedical Engineering at the National University of Colombia where he developed a computational model to simulate osteogenesis and bone fracture healing, obtaining his Master´s Degree in 2011. In this same year, he was awarded in Colombia with a scholarship to study doctoral studies abroad. In October 2011 he started his Doctoral studies in the group of Orthopaedic Biomechanics in the Department of Biomedical Engineering at Eindhoven University of Technology. The results of his research about the estimations of mechanical properties of intact and damaged bone tissue based on High Resolution CT-images are presented in this dissertation.

List of Publications

Related with this thesis

Arias-Moreno A.J., Hosseini H.S., Bevers M., Ito K., Zysset P.K., van Rietbergen B., 2019. Validation of distal radius failure load predictions by homogenized- and micro-Finite Element analyses based on second generation high resolution peripheral quantitative CT images". *Osteoporosis International*, DOI: 10.1007/s00198-019-04935-6.

Arias-Moreno A.J., Ito K., van Rietbergen B., 2016. Micro-Finite Element Analysis will overestimate the Compressive Stiffness of Fractured Cancellous Bone. *Journal of Biomechanics* 49, 2613-2618.

Arias-Moreno A.J., Ito K., van Rietbergen B., 2019. Accuracy of Beam Theory for Estimating Bone Tissue Modulus and Yield Stress From 3-point Bending Tests on Rat Femora. Submitted to *Journal of Biomechanics*.

Arias-Moreno A.J., Ito K., van Rietbergen B., 2019. The compressive stiffness of cemented cancellous bone. In preparation.

Other publications

5. Yeoh S.Y., **Arias-Moreno A.J.**, van Rietbergen B., Hoeve N.D. ter, van Diest P.J., Grull H., 2015. Effects of magnetic resonance-guided high-intensity focused ultrasound ablation on bone mechanical properties and modeling. *Journal of Therapeutic Ultrasound* 3, 1-10.

Acknowledgements

… And this doctoral experience that began a few years ago has come to an end. It is an infinite joy for me to culminate this step and to continue with the new challenges that await me in the future. As a dear professor and friend told me once, “this is only the beginning”. And each step in life is a process of personal and professional growth that I experience day by day in this step through life. Thanks be to God, María Auxiliadora, San Juan Bosco and Santo Domingo Savio, protectors, guides and sources of strength, stability and blessing, because everything that happens has a reason to be and life is a continuous learning process.

This experience would not have been possible without the important support of COLCIENCIAS and the Autonomous University of Manizales, who granted me a doctoral scholarship to learn and promote science. I hope to return this support with my future contributions.

I would like to thank Professor Keita Ito, who opened the doors of his research group to me and permanently provided a light and guide in my research when things seemed not to reach a clear point.

Always an instructor and guide in the process, Dr. Bert van Rietbergen maintained his kind willingness and patience to work alongside me in obtaining the good results presented in this thesis. Thank you very much Bert, with you I learned even more the meaning of the word Research.

I would like to thank the members of my doctoral committee for kindly agreeing to be part of this evaluation group. Thank you very much for your diligent work.

The experimental work of this study could be carried out thanks to the permanent good assistance and support given by the human technical component of the department. I want to express my gratitude to the staff in charge of the Biolab and the workshop: Rob Petterson,

Mascha Maenhout-van Haag, Jurgen Bulsink, and Rob van de Berg. All of them always with the best disposition to support me in my research processes.

An important contribution made to one of the relevant components of my study came from the experts in Biostatistics, who always responded and guided me when I asked for their help. I would like to offer my special thanks to Professor Koo Rijpkema, of the Department of Mathematics and Computer Science, and to Adam and Mark Lund, biostatisticians by passion.

An important aspect to carry out a research study is the group of people that surround us during this work, because they generate the necessary work environment to advance, learn and obtain good results. In this role, the people from the Orthopaedic Biomechanics research group have accompanied me and supported me to reach the end of the trip. Thanks a lot to all of them, the old ones and the new ones, especially to Reza, Juan, Patrik, Javad, Michele, Irene, Marc, Johanna, Feihu, Nicole, Alireza and Maria.

My sincere thanks to the executives and diligent workers who always gave me a hand when I needed administrative formalities and clarification about life in Eindhoven. To Janneke Cuijpers, Wendy Brouwers-Weber, Evelien Arts-Arts, Yvon Biemans, Mariken Coppens, and Liesbeth van den Akker, thank you very much.

My colleagues and friends in the room Gem-Z 4.09 and in the fourth floor: Francesco, Fabio, Arianna, Renee, Marleen (and Meilof), Inge, Germaine, Joke, Gitta, Tilaï, Tommaso, Valentina, Tamara, Amin, Héctor, Carlos, Umit, Priscilla, Awital and Carlitos Chavarri. Thank you for the working atmosphere and for the good moments shared inside and outside the University.

As Jhonny and el Orejon put it, "To bless oneself and to cross a border makes the warrior, who learns to fight outside, stronger." To all those Colombian and Latin American warriors who, along with me, crossed the border, thank you very much. This time would not have been the same without you: Maria Elena and Benny (by adoption), Lilito with Juand Di and Miguel, Juan and Sol, David "el Chuchinga", JC and Mabe, Camilín and Carla, Andresito and Carito, Cesar and Nina (by adoption), Francisco "el Hombre", Héctor, Pablito and Yuyu, Johanna Pepita and Robinson, Oscar and Viviana, Claudia and Antonio.

To my Zumba fellowship: you made my days. Always! Thanks goes to Lara, Greta, Jaya, Ronnie, Katarina, Aromal, Norent, Aida and Cansu.

To my dear teachers "de la Nacho", Andrés, Diego, Karim, Mafe, Lucy, Amalia. Thank you! With your knowledge and talent, you paved my way to get where I am today. To my colleagues in Manizales, who were always looking out for me. My sincere thanks to Albita, "El profe" Jose Germán, Fabiecito, Tino, Cesar, Sebastián, Diana (x2), Olga (x2), Sandra, Yesid and Mauricio.

My memories, prayers and gratitude of life for those who transcended in my absence: Leopoldo, Teresita, Adelita, Sole, Delio, Eva, Juanito, Nancy. This thesis is also dedicated to you.

Great achievements are made with great tools. Thanks to Pupi, Carmelo, Teo and Monserrat for their invaluable support in taking this thesis to the end.

Those who accompanied me day by day, have made me laugh, and didn't let me fall. Heartfelt thanks go to Les Luthiers and J.S. Mastropiero, as well as to Chespirito and his group.

I would like to express my very great appreciation to Olga Salinas, because with our talks you have taught me to believe in myself and to reach a strong and solid level of thought and life.

Now I'm going to thank my family in my native Spanish language. A mi Famila y amigos en Colombia, que siempre han estado allí. ¡¡¡Gracias!!!. A la señora Mae, por toda tu atención y esfuerzo, por consentirnos y cuidarnos. A Tato, por todo el apoyo brindado y los abrazos cada vez que he vuelto a casa (¡que gran trabajo tu portada, que gran diseñador eres!). A Adriana y Valentina, por su cariño y buenos momentos en mis visitas. A Totto y Daniel, por recibirme en su

casa cuando ando por allá, por su cariño y su zoológico. A Jairo y Melba, Diego, Flor y Paula, por su constante atención a mis pasos y su compañía permanente en la distancia. A Teresa y Andy, Sonia Y Shawn, por su cariño y apoyo. Shawn, ¡sos grande! Gracias por esa mano que nos has dado al final. Fue muy importante. A Jannette, Jandota y Tifa, por su cariño y acogida cuando nos hemos encontrado. Felicitaciones por las nuevas adquisiciones. Que estos primitos sean bendiciones para sus vidas. A Neftalí y Anatilde, que siempre preguntan por mí. A Emmy y Melqui, "los Sabios de Caldas", una vez más y como siempre, me han dado una mano, un hogar, un ejemplo de amor y de valentía. Los quiero y los admiro. A Marcelo, apoyo y amigo en Manizales. A Eu, una mano amiga siempre. A Omar, mi hermano Tigre, mi biólogo marino más admirado, ¡Tigre, lo logramos! A Ángela Edith, amiga, gracias por ese cariño desde que eramos chiquitos en la U. A Diomar, mi viejito pechilanudo, gracias por abrigarme cada vez que vamos a ascender nevados y a alcanzar nuestras cimas.

To my paranymph, Johanna. I can't have better company by my side on one of the most important days of my life. Thank you for the steady and beautiful disposition for every moment. Thank you for placing your sympathy and intelligence at the service of others.

And to the person I most admire and love in my life, Lorenza. Thank you. Thank you. Thank you. You and I are God's will and through him we are together, here and now, and from the moment it corresponded to us. My light, my blessing, my motivation and my inspiration. This achievement is ours, and also those who are on the way too. Blessed photocopy! ¡Dios bendiga a la Muñeca!